WELD METAL SOLIDIFICATION AND SOLIDIFICATION MODELING IN ELECTROSLAG SURFACING

Youping Gao

B.S., Beijing Polytechnic University, 1987

A dissertation submitted to the faculty of the
Oregon Graduate Institute of Science & Technology
in partial fulfillment of the requirements for the degree
Doctor of Philosophy
in
Materials Science and Engineering

January, 1996

The dissertation ***"Weld Metal Solidification and Solidification Modeling in Electroslag Surfacing"*** by Youping Gao has been examined and approved by the following Examination Committee:

Jack H. Devletian, Thesis Advisor
Professor

William E. Wood
Professor, Department Chairman

Lemmy L. Meekisho
Assistant Professor

James T. Stanley
Assistant Professor

ACKNOWLEDGMENT

I would like to express my sincerest appreciation to my thesis advisor, Dr. J.H. Devletian, for his guidance, support, and patience through this work. I also wish to thank Dr. W.E. Wood, Dr. L.L. Meekisho, and Dr. J.T. Stanley for examining my dissertation and sharing their professional opinions. I am grateful to Dr. D.G. Atteridge for many invaluable discussions regarding this research work. I would also like to acknowledge R. Turpin, N. Shannon, Q. Zhao, R. Parthasarathy, J.Y. Zhang, and K. Terry for their cooperation on this project. I also thank my fellow students W. Y. Shen, M. Li, D. Singh, V. Dikshit, F. Lu, J. Ding, H. Su, W. Su, and X. Chen for their friendship.

I wish to acknowledge the National Center for Excellence in Metalworking Technology (NCEMT) for sponsoring this project. NCEMT is operated by Concurrent Technologies Corporation (CTC) under contract to the U.S. Navy as a part of U.S. Navy Manufacturing Technology Program.

I wish to give special thanks to Mr. Stephen Yih and Dr. Erwin Rudy for their generosity and foresight in the establishment of my professional career. Words are inadequate to express my deep appreciation to my wife, Dan Li, and my parents for their support spiritually and emotionally.

TABLE OF CONTENTS

TITLE PAGE i
APPROVAL PAGE ii
ACKNOWLEDGMENT iii
TABLE OF CONTENTS iv
LIST OF TABLES vii
LIST OF FIGURES ix
ABSTRACT xiii
CHAPTER I. INTRODUCTION 1
CHAPTER II. BACKGROUND 7
SURFACING TECHNOLOGY 7
Weld Surfacing Processes 7
Electroslag Surfacing 8
NICKEL ALLOY 625 11
Metallurgy of Nickel Alloy 625 11
Welding of Nickel Alloy 625 12
STRUCTURE of WELDMENT 14
WELD METAL SOLIDIFICATION 16
Microstructure Evolution 16
Epitaxial and Non-epitaxial Growth in Welding 16
Microsegregation 20
MODELING of WELD METAL SOLIDIFICATION 22
WELD METAL SOLIDIFICATION CRACKING 27
Mechanisms of Solidification Cracking 27
Factors Affecting Solidification Cracking 28
Features of Solidification Cracking 30

Solidification Cracking Test 31
CHAPTER III. EXPERIMENTAL PROCEDURES 33
MATERIALS 33
Surfacing Strips 33
Base Materials 34
Surfacing Fluxes 35
WELDING EQUIPMENT 36
ELECTROSLAG SURFACING PROCESS 38
Surfacing Process Variables 38
Light Image Analysis 39
Chemical Composition of Cladding 41
WELD METAL SOLIDIFICATION 41
Quenched Interface Studies 42
Solidification Cooling Rate 42
Differential Thermal Analysis 44
Weld Metal Solute Segregation 45
Metallography 46
Scanning Electron Microscopy 47
EXPERIMENTAL VERIFICATION of the MODEL 47
Solid/Liquid Fraction Measurement 48
Solute Concentration Measurement 48
WELD METAL SOLIDIFICATION CRACKING TEST 49
Cracking Susceptibility of Cladding Materials 51
Effect of Cladding Variables 51
CHAPTER IV. RESULTS and ANALYSIS 53
ESS PROCESS OPTIMIZATION 53
Surfacing Variables 53
Composition Profiles 61
WELD METAL SOLIDIFICATION 65
Weld Pool & Weld Metal Solid/Liquid Interface 65

Solidification Parameters 66
Freezing range of nickel alloy 625 cladding 66
Solidification cooling rate 67
Solidification & Segregation 72
Solid/liquid interface in cladding 72
Interdendritic precipitates 77
Variable partition coefficient 80
Weld Metal Microstructure 81
The unmixed zone 82
The composite zone 87
WELD METAL SOLUTE REDISTRIBUTION MODEL 89
Model and Its Assumptions 89
Model Predictions and Validation 93
SOLIDIFICATION CRACKING SUSCEPTIBILITY 101
CHAPTER V. DISCUSSION 106
WELD METAL MICROSTRUCTURE EVOLUTION 106
Formation of the Unmixed Zone 106
The Composite Zone 109
Weld Metal Microstructure Evolution 110
SOLIDIFICATION MODELING 113
Solidification Parameters Estimation 117
WELD METAL SOLIDIFICATION CRACKING 117
CHAPTER VI. CONCLUSIONS 119
REFERENCES 122
APPENDIX 137
BIOGRAPHICAL NOTE 140

LIST OF TABLES

2.1	Comparison of Welding Processes Used for Surfacing	8
2.2	Summary of the Phases Found in Nickel Alloy 625 Weld Metal	14
3.1	Compositions (wt%) of Strip Electrode Filler Metals	34
3.2	Compositions (wt%) of Base Metals	35
3.3	The Major Chemical Ingredients of the Surfacing Fluxes	36
3.4	Combination of Filler Metal and Base Metal Used in Weld Metal Solidification Study	42
3.5	Welding Variables of ESS and GTAW Used in Weld Metal Solidification Study	44
3.6	DTA Analysis Parameter for Measuring Clad Metal Solidus and Liquidus	45
4.1	Optimized ESS Variables for 30 x 0.5 mm Nickel Alloy 625 Strip Electrode Deposit on MIL-S-23284, Class 1 Shafting Steel	60
4.2	Typical Characteristics of ESS and SAS Deposits using 30 x 0.5 mm Nickel Alloy 625 Strip Electrode on MIL-S-23284, Class 1 Shafting Steel under the Condition Listed in Table 4.1	60
4.3	Chemical Compositions of Four Layer Cladding of Nickel Alloy 625 Deposited on MIL-S-23284 Class 1 Steel by ESS	63
4.4	Chemical Compositions of Four Layer Claddings of Nickel Alloy 625 by SAS	64
4.5	Alloying Vectors for ESS and SAS Process	64
4.6	Solidus and Liquidus of Nickel Alloy 625 Cladding Deposit	67
4.7	SEM/EDS Analysis of Water-Quenched Cladding of Nickel Alloy 625 Deposited on MIL-S-23284 Class 1 Steel by ESS	73

4.8 EDS Analysis of Laves Phase and Carbide in Nickel Alloy 625 Cladding by ESS 79

4.9 Niobium Redistribution in Nickel Alloy 625 Deposited on Class 1 Shafting Steel by ESS 80

4.10 Effect of Filler Metal and Base Metal Compositions on the Formation of the Unmixed Zone 83

4.11 EDS Analysis of the Unmixed Zone and Composite Zone in Nickel Alloy 625 Deposited on 304 Stainless Steel by ESS 85

4.12 EDS Analysis of the Unmixed Zone and Composite Zone in Nickel Alloy 625 Deposited on 316 Stainless Steel by ESS 85

4.13 The Initial Values for the Model for the Solute Redistribution of Niobium during Solidification of Nickel Alloy 625 Cladding 93

4.14 Comparison of Experimental Data with the Model, Nb Concentration in the Interdendritic Liquid of Nickel Alloy 625 Cladding 96

4.15 Cracking Index (CI) of 30 mm Strip Deposit on 25 mm Thick MIL-S-23284, Class 1 Steel 101

4.16 Effect of Cladding Variables on Solidification Cracking Susceptibility (CI) 102

LIST OF FIGURES

1.1	Electroslag Surfacing Processes	2
1.2	Deposition Rates and Welding Current Operating Ranges Comparison among the Popular Surfacing Processes	3
2.1	Schematic Illustration of the Electroslag Surfacing Process	9
2.2	Metallurgical Zones in a Typical Weld	15
2.3	Classification of Hot Cracking in Welding	31
3.1	The Surfacing Equipment Setup	37
3.2	The Output Volt-Ampere Characteristics of the Power Source	38
3.3	Showing the Image Analysis Procedures	40
3.4	Illustration of the Transverse Cross Section of Surfacing Deposit	40
3.5	Schematic Showing of the DTA Specimen Orientation in Cladding	45
3.6	Schematic Illustration of the position of SEM/EDS Compositional Analysis in Interface Quenched Cladding Specimen	46
3.7	OGI Solidification Cracking Test for Strip Cladding	50
3.8	Solidification Cracking Test for Strip Cladding	51
4.1	The Typical Cross Section of Nickel Alloy 625 Cladding Deposited on MIL-S-23284 Class 1 Steel by ESS	55
4.2	The Typical Cross Section of Nickel Alloy 625 Cladding Deposited on MIL-S-23284 Class 1 Steel by SAS	55
4.3	Image Analysis of the Nickel Alloy 625 Cladding Deposited on MIL-S-23284 Class 1 Steel by ESS	56
4.4	The Effect of Current on the Deposition Rate, Dilution, and Penetration of Nickel Alloy 625 Surfacing Deposited on MIL-S-23284 Class 1 Steel	57

4.5 The Effect of Travel Speed on the Deposition Rate, Dilution, and Penetration of Nickel Alloy 625 Surfacing Deposited on MIL-S-23284 Class 1 Steel 58

4.6 The Effect of Voltage on the Deposition Rate of Nickel Alloy 625 Surfacing Deposited on MIL-S-23284 Class 1 Steel 59

4.6a Water Quenched Weld Metal Solid/Liquid Interface of Nickel Alloy 625 Electroslag Surfacing 65

4.7 Illustration of the Weld Metal Solid/Liquid Interface of Nickel Alloy 625 Electroslag Surfacing 66

4.8 Dendritic Structure of GTA Remelted Nickel Alloy 625 ESS Deposit 68

4.9 Dendritic Structure of Nickel Alloy 625 Cladding Deposited on MIL-S-23284 Class 1 Steel by ESS 69

4.10 Cooling Rate in Nickel Alloy 625 Composite Zone of ESS and GTAW Calculated from Heubner's Correlation 70

4.11 Cooling Rate Determination of the Unmixed Zone in Nickel Alloy 625 Deposited on 316 Stainless Steel Based on Grant's Correlation 71

4.12 Optical Micrograph of the Water-Quenched Cladding Sample of Nickel Alloy 625 Deposited on MIL-S-2384 Class 1 Steel 73

4.13 Optical Micrograph of Nickel Alloy 625 Cladding Deposited on Class 1 Steel 74

4.14 Scanning Electron Backscattered Image of Nickel Alloy 625 Cladding Deposited on Class 1 Steel 75

4.15 SEM Micrograph of Niobium-rich Liquid Network in the Water-Quenched Nickel Alloy 625 Cladding Deposited on MIL-S-23284 Class 1 Steel by ESS 76

4.16 SEM Backscattered Image Shows g Matrix (dark area) and Interdendritic Precipitates (bright area) for Nickel Alloy 625 Cladding Deposited on Class 1 Steel by ESS 77

4.17 Scanning Electron Microscopy Showing Laves Phase in Nickel Alloy 625 Cladding Deposited on Class 1 Steel by ESS 78

4.18 Scanning Electron Microscopy Showing Carbides in Nickel Alloy 625 Cladding Deposited by ESS 79

4.19 The Locations (a, b, c, d) of the Composition Measurement in the Dendritic Structure of the Water Quenched Nickel Alloy 625 Cladding Deposited on Class 1 Steel 81

4.20 Interface of Nickel Alloy 625 Deposit on Class 1 Shafting Steel by ESS process 82

4.21 Microstructure of the Unmixed Zone in Electroslag Surfacing on 316 Stainless Steel Base Metal using Nickel Alloy 625 Strip Electrodes 84

4.22 Epitaxial Growth in the Unmixed Zone of Nickel Alloy 625 Deposited on 316 Stainless Steel by ESS 86

4.23 The Grain Structure of Five Layer Nickel Alloy 625 Deposited on Class 1 Shafting Steel by ESS 88

4.24 The Cylindrical Coordinate Used in this Model 89

4.25 The Model Predicted an Interdendritic Liquid Fraction of 12.5% when the Nb Concentration in the Liquid is Equal to 12.6 (wt%) 94

4.26 SEM Backscatter Image of the Interdendritic Liquid from the Quenched Interface Cladding, at the Stage where CLNb is Reached to 12.6 wt% in the Liquid (Liquid Fraction = 12.5%) 95

4.27 Comparison between Predicted and Experimental Data for Interdendritic Liquid Fraction at Different Nb Concentration Level 96

4.28 SEM Backscatter Image of the Interdendritic Liquid from the Quenched Interface Cladding, at the Stage where CLNb is Reached to 9.99 wt% in the Liquid (Liquid Fraction = 17.4%) 97

4.29 SEM Backscatter Image of the Interdendritic Liquid from the Quenched Interface Cladding, at the Stage where CLNb is Reached to 12.5 wt% in the Liquid (Liquid Fraction = 12.7%) 98

4.30 SEM Backscatter Image of the Interdendritic Liquid from the Quenched Interface Cladding, at the Stage where CLNb is Reached to 13.2 wt% in the Liquid (Liquid Fraction = 11.8%) 99

4.31 Predicted Interdendritic Liquid Fraction for Different Heat Input Cladding by ESS at CLNb = 12.6 (wt%) 100

4.32 Illustration of Solidification Fracture Surface of the Solidification Cracking Test 103

4.33 Solidification Cracking Morphology of Dendritic Fracture in Nickel Alloy 625 Cladding 103

4.34 Solidification Cracking Surface of Nickel Alloy 625 Cladding Showed a Groove Morphology 104

4.35 Ductile Fracture of the Non-cracking Cladding Bead Portion in Nickel Alloy 625 Cladding by ESS 105

5.1 Interface Regions of 410 Stainless Steel Deposited on A36 Steel by ESS 107

5.2 Optical Micrograph of the Interface Region of 304 Stainless Steel Deposited on 304 Stainless Steel (Matched Filler Metal) by ESS 108

5.3 Optical Micrograph of the Interface Region of Nickel Alloy 625 ESS Deposit Remelted by GTA Autogenous Welding 109

5.4 Grain structures of the Composite Zone in Nickel Alloy 625 Deposited on Class 1 Steel 110

5.5 Microstructure of the Interface Region of Nickel Alloy 625 Deposited on 304 Stainless Steel Base Metal by ESS 112

5.6 Comparison of the Current Model with Scheil, Sawai, and Cieslak Model for Interdendritic Liquid Fraction at Nb =12.5 wt% for solidification of nickel alloy 625 115

ABSTRACT

WELD METAL SOLIDIFICATION AND SOLIDIFICATION MODELING IN ELECTROSLAG SURFACING

Youping Gao, Ph.D.

Supervising Professor: Jack H. Devletian

Electroslag surfacing (ESS) with strip electrodes is a cost-effective and efficient method to combine the structural properties of the substrate material with the surface properties of the cladding. For example, ESS of high strength steel propulsion shafting with a thin layer of highly corrosion-resistant (but expensive) nickel alloy 625 provides a cost-effective means to manufacture ship shafting with both high strength and high corrosion resistance. Despite the economic benefits, the solidification mechanism and microstructural characteristics involving dissimilar metal cladding combinations have not been adequately addressed for ESS.

The solidification mechanism and microstructural characteristics of ESS deposits involving several common strip and base metal compositions were investigated and compared to traditional techniques such as gas-metal arc (wire) and submerged arc strip surfacing methods. Strip compositions for ESS included: (a) nickel alloys 625, 59, 200, and 70/30 NiCu; (b) stainless steels 304, 308L, and 410; and (c) 70/30 CuNi alloy. Base metals included: MIL-S-23284, Class 1 steel as well as 304 and 316 stainless steels.

The solidification mechanism of strip cladding by ESS is modeled and verified by experiments. In this study, the distribution of alloying elements such as niobium is determined experimentally and modeled using the modified Scheil equation with solid state diffusion and the new concept of a variable equilibrium partition coefficient for enhanced accuracy. This model has successfully predicted the distribution of alloying elements in dissimilar metals cladding such as nickel alloy 625 deposited on steel.

The unique microstructure of cladding deposited by ESS is characterized by virtually 100% vertically oriented dendrites. The mechanism of epitaxial growth and renucleation is used to model this phenomena. The weld metal solidification initiates epitaxially from the unmixed zone and grows competitively into the composite zone. Nucleation may occur near the interface between the unmixed zone and the composite zone when the new grains in the unmixed zone have an unfavorable growth direction. In addition, because the weld pool size is large and the solid/liquid interface moves vertical-up, the resulting microstructure is characterized by the unique microstructure where grains and dendrites are virtually all parallel to the vertical axis. Precipitation of second phases such as MC carbides and Laves phases in nickel alloy 625 cladding has be modeled and verified by interface-quenching experiments. A new solidification cracking test has been developed and successfully applied as means of ranking cracking resistance of strip cladding.

In summary, this work characterizes and models the solidification mechanism for electroslag surfacing of dissimilar strip/base metal combinations. In addition, a new weld metal solidification cracking test is developed for strip surfacing process.

CHAPTER I

INTRODUCTION

Surfacing of a material with a desired property onto a component to attain a combined property is an effective way to best utilize materials in engineering practice. The economic value of the composites is clearly seen in the cases where the surfacing provides inexpensive low-alloy steel with a high degree of resistance to a wide range of working environments. In those applications, welding has been the primary process in manufacturing such composite structures.

Electroslag surfacing (ESS, shown in Figure 1.1) with its unique features is a proven ideal welding process for thick section component surfacing.[1-22] Since the introduction of ESS in 1971,[1] it has gained tremendous popularity in industry especially in Europe and Japan. Many fluxes have been developed for different applications.[15,20,22,23] The state of the art ESS uses strip electrodes up to 300 mm wide which gives ESS such a high deposition rate far beyond any other weld surfacing processes can possibly reach.[20,21] A comparison of the relative deposition rates and welding current operating ranges among the popular surfacing processes is shown in Figure 1.2. At optimum working conditions, ESS provides many advantages over other surfacing processes. The most important characteristic of ESS is that it offers low dilution (compare to other high deposition rate processes) and high deposition rate simultaneously which is often a contradictory factor in most other welding processes. This is especially suitable for

Figure 1.1 Electroslag Surfacing Processes.

surfacing purposes where retention of the proper surfacing material composition is important and high efficiency is achieved at the same time.

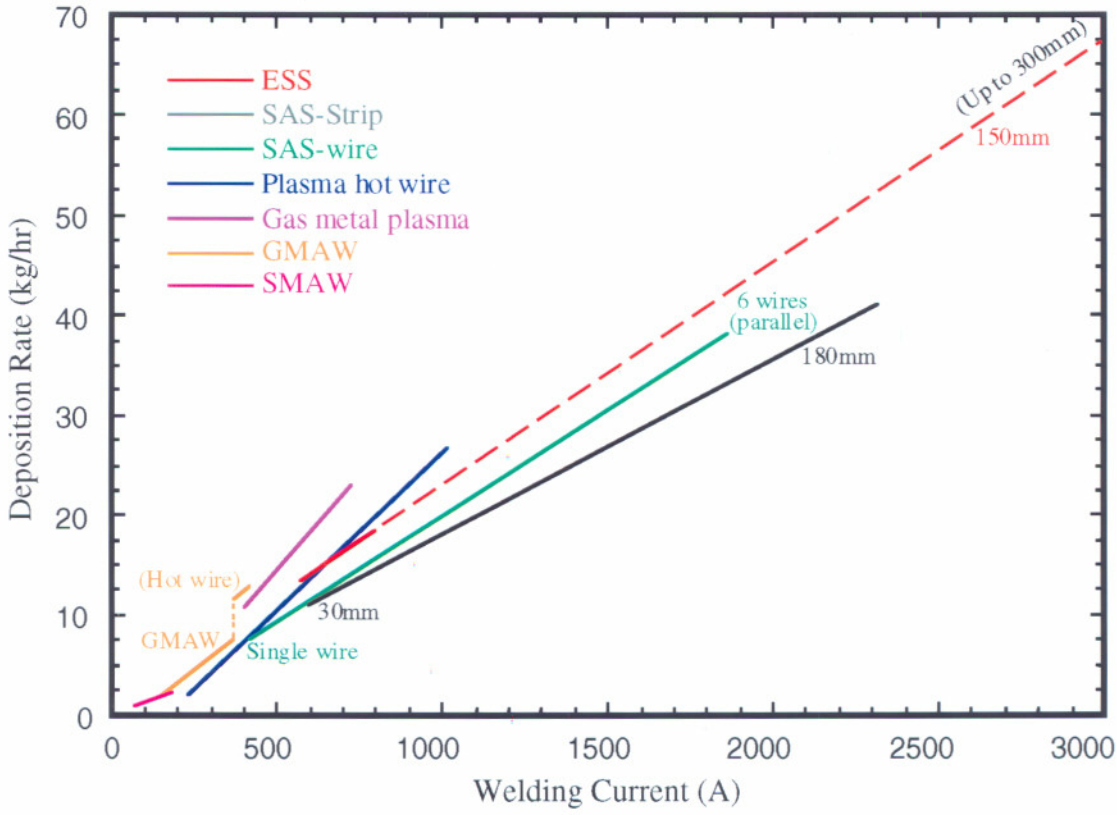

Figure 1.2 Deposition Rates and Welding Current Operating Ranges Comparison among the Popular Surfacing Processes.

Nickel alloy 625 has high strength, excellent fabricability, outstanding corrosion resistance in air and sea water, and good weldability.[24,25] It has been widely used in the industries where the service conditions are particularly severe. As a solution strengthened superalloy, it upholds its excellent properties in wrought, cast, and weld product forms. In marine conditions, its virtual immunity to general corrosion and chloride-induced stress-corrosion cracking[26-28] makes it ideal for surfacing low alloy

steel components exposed to seawater and subjected to high mechanical stresses. Although weld metal solidification cracking problems have been encountered in welding and surfacing,[29,30] many successful applications of nickel alloy 625 surfacing have been demonstrated.[18,19,31-35] In the present study, nickel alloy 625, as the surfacing material, is used to surface low alloy steel propulsion shafting by the ESS process for the long term corrosion protection.

Despite the promising future of ESS and the industrial prospective of ESS, the studies on the ESS process have been so far limited to the performance characteristics. In previous studies on dissimilar metal welding, a unique microstructure morphology[5,18,19,36] had been observed. It appeared to defy conventional studies developed for weld metal. However, the mechanism for forming such structures remains unknown. In fact, the basic aspects regarding the microstructure evolution in surfacing deposited by ESS have not yet been studied. In autogenous or matching filler metal welding, the grain growth in the weld metal initiates epitaxially and grows competitively. The nucleation event is insignificant in weld metal solidification.[37-44] However, in dissimilar metal welding, due to the presence of an unmixed zone, the weld metal solidification starts with essentially unmixed molten base metal solidifying on solid base metal then growing into a chemically different composite zone. Those differences along with the new observations of the unique microstructures[5,18,19,36] have demonstrated the need for further study of weld metal solidification in ESS surfacing.

In order to better understand and control the solidification process, many models have been developed to analyze microsegregation during solidification in casting and other welding processes.[45-55] Models derived from binary alloy systems have been used for the complex multi-component alloys based on the assumption that the individual

alloy components do not influence each other with respect to segregation behavior, and often it is under the assumption that the partition coefficient applied at the interface is a constant throughout solidification. Those assumptions are not valid for the solidification of complex alloy such as nickel alloy 625 in the current study. A new model that accommodates multi-component alloy system with a variable partition coefficient throughout solidification and takes into account of back diffusion in the solid is developed and effectively predicted solute redistribution in the weld metal solidification of nickel alloy 625. Furthermore, a correlation of solute segregation and welding condition has been established for nickel alloy 625 surfacing. Since solidification cracking susceptibility is to a degree dependent upon the extent of segregation and the components which are segregating, the correlation between solidification cracking susceptibility and welding condition has also been established based on the solidification model.

A variety of weldability tests have been developed to study the performance characteristics of materials and processes during the welding.[56,57] However, none of them can be easily adopted in the strip surfacing process.[58,59] It was found in present study that those weldability tests produce an altered weld metal microstructure different from that of ESS. Therefore, such test results could not represent strip surfacing conditions. A new testing method has been developed in this study to evaluate the solidification cracking tendency in order to make an assessment on welding materials and process parameters.

In this study, the ESS process has been compared with the popular submerged arc surfacing (SAS) process using 30x0.5 mm nickel alloy 625 strip electrode deposited on MIL-S-23284 class 1 steel. Different combinations of filler metal and base metal have also been studied. The essential aspects of ESS strip surfacing such as weld pool

formation, solidification mechanism, and microstructure evolution have been investigated in both dissimilar metal and matched filler metal cladding. An optimum welding condition has been attained. An analytical model with variable partition coefficient for solute redistribution during weld metal solidification has been developed. Also, a correlation has been established between weld metal microstructures and the solidification cracking susceptibility. A new testing device to assess solidification cracking susceptibility particularly designed for strip surfacing is also being employed.

The objectives of this study are:

- To study the fundamental aspects of the electroslag surfacing process regarding weld pool formation and weld metal solidification mechanism.
- To establish a model to predict solute redistribution during weld metal solidification in surfacing and to compare the model with experimental data, and
- To investigate the weld metal solidification cracking susceptibility, mechanism, and the influencing factors in strip surfacing process using a newly developed solidification cracking test.

CHAPTER II

BACKGROUND

Materials are frequently called upon to perform multiple functions, and often no single alloy is the best for each of the required functions. Composite material is one of the solutions to this problem and often this has become both a structural and an economic necessity. One of the most common techniques applied to construct such composites for improving a material's resistance to corrosion and wear is weld surfacing.

SURFACING TECHNOLOGY

Manufacturing processes to build composite structures include weld surfacing, roll bonding, explosion bonding and other mechanical methods. Among those methods, weld surfacing has been the most versatile and popular way to produce clad structures.

Weld Surfacing Processes

Surfacing has been a common industrial practice for many years. Although many different welding processes, or derivatives of those processes, as listed in Table 2.1, could be used for the surfacing purpose, labor intensity, low deposition rate and inefficiency had always been the major drawbacks during the early years of weld surfacing. In order to increase deposition rate and cover a larger surface area, a strip

cladding technique was applied[60-63] in the early 60's using strip electrodes with the submerged arc welding process - submerged arc surfacing (SAS). This automatic strip cladding process, which was considered the most cost-effective method to surface large components, dramatically increased the deposition rate and reduced intensive labor requirement. It has been exclusively used in the industries since then.[64,65] Another important factor in surfacing is that the penetration must be limited to a minimum so that the desired surfacing material properties can be properly retained. However, excessive dilution from base metal is intrinsic in this arc welding process and deteriorates the overlay properties. Often, more than one layer of overlay is required to ensure the proper surface composition and properties.

Table 2.1 Comparison of Welding Processes Used for Surfacing

Welding process	Typical deposit thickness, mm	Deposition rate	Dilution level	Feature
Oxyfuel	1-2	low	low	labor intensive
SMAW	3	low	moderate	labor intensive
GTAW	1.5-2	low	low	labor intensive
GTAW hot wire	3-4	moderate	low	labor intensive
GMAW	3-4	moderate	moderate	labor intensive
GMAW pulsed	2-3	low	low	labor intensive
Plasma	3-4	moderate	low	labor intensive
SAW wire	3-5	moderate	high	automatic
SAS strip	4-5	high	moderate	automatic
ESS strip	4-6	high	low	automatic

Electroslag Surfacing

In 1971, Seidel and Hess[1] invented an improved cladding process which had a similar appearance to SAS but used an electroslag technique called electroslag surfacing

(ESS) or electroslag strip cladding. It utilized the same principle as electroslag welding developed by Hopkins[66] in the United States in the 1930's, except that electroslag cladding operated in the flat position with a rather shallow layer of molten slag pool and used a strip electrode. In electroslag strip cladding, there is no arc except during the initiation. The heat of fusion is generated by the ohmic heating of a molten slag pool with the passage of electric current through it. This ohmic heating melts not only the filler metal and the surface of the base metal, but also the flux to maintain a dynamically steady slag pool as such to protect the weld metal from atmospheric contaminants as the process proceeds Figure 2.1. The filler electrode is continuously fed into the slag pool, where it melts and deposits on the surface of the substrate. The equipment setup for ESS is similar to that of SAS.

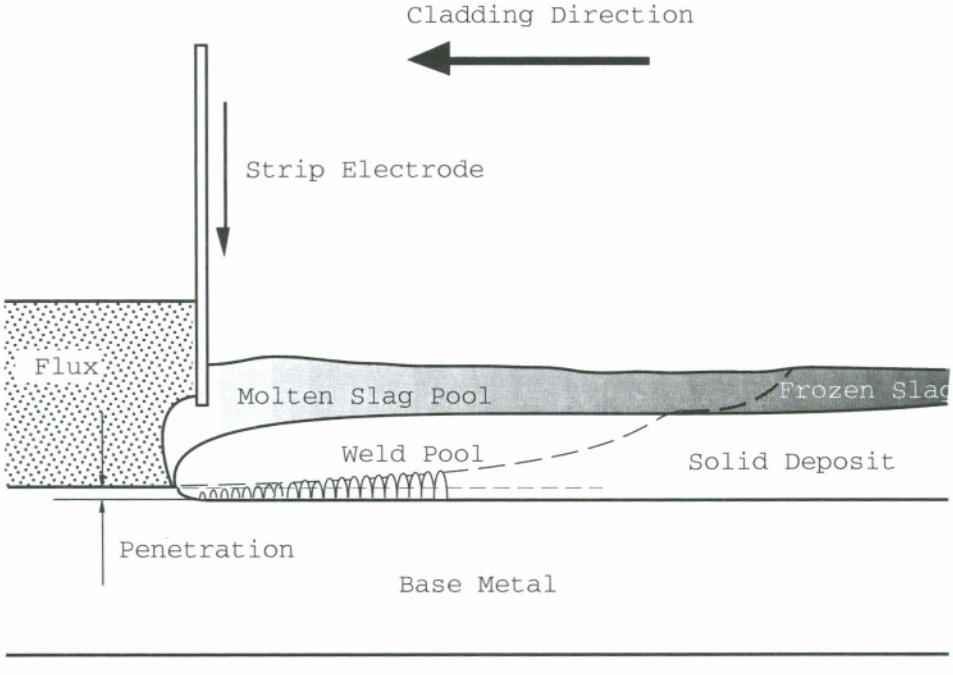

Figure 2.1 Schematic Illustration of the Electroslag Surfacing Process.

The electroslag strip surfacing process has many advanced features over other cladding processes.[1-16,18-22,67-69] One important feature is that it combines two usually contradictory factors in welding: high deposition rate and low dilution. Moreover, it offers more uniform shallow penetration, easier and more effective alloying adjustment through flux,[70] cleaner deposits, lower oxygen content,[71] better slag detachment, superior surface finish, wider strip capability, and lower workmanship requirement as compared with conventional surfacing processes. In comparison to its nearest competitor SAS, ESS allows higher welding current density than SAS does especially when wider strip is applied. ESS deposit is metallurgically cleaner than that of SAS. Due to its superior performance characteristics and cost-effectiveness, the ESS process has virtually eliminated other competitive processes used for thick section surfacing in Japan. It has been widely used from the internal surface cladding of pressure reactor vessels to the external surface cladding of marine structural components, to improve heat resistance, corrosion resistance, and wear resistance as in hardfacing.[72,73]

Despite the wide application of ESS in industry, the studies on the ESS process have been so far limited to the performance characteristics with emphases on the surfacing composition, operating parameters, mechanical and corrosion properties. They have provided an important guideline to industry in applying the ESS process. Some have studied the microstructures produced by the ESS process. A unique microstructure morphology[5,18,19,36] has been found. It appears different from conventional welding microstructures. However, questions still remain to be answered regarding how such microstructure is produced in the ESS process.

NICKEL ALLOY 625

Metallurgy of Nickel Alloy 625

Nickel alloy 625 (UNS N06625, NiCr22Mo9Nb, ENiCrMo-3) was developed in the early 60's by H. L. Eiselstein of Inco Alloys International, Inc. Originally, it was designed for applications in high-strength main steam-line piping and gas turbine materials for super critical steam power plants.[25] Due to its specific combination of excellent fabricability, mechanical properties and corrosion resistance in both wrought and cast product forms, it has gained its popularity as the second mostly used nickel base superalloy.[74,75] Beyond the original applications, it is now widely used as a generic alloy throughout industries where the corrosion problems are particularly severe. This alloy contains many elements, and most of them are strategic materials. For economic and conservative considerations, nickel alloy 625 has often been used as a surfacing material. Surfacing can be achieved by weld surfacing, roll bonding,[76] explosion bonding and other mechanical methods. (thermohydraulically and P/M coextruded)[77,78] Among those methods, weld surfacing has been the most popular method to produce a clad structure.

Under marine conditions, nickel alloy 625 is immune to crevice corrosion and chloride-induced stress-corrosion cracking. It has been exploited as the weld surfacing material for corrosion resistance in the marine applications.[18,19,31,32,34] Additional applications as weld surfacing material can be found in nuclear reactors for high temperature corrosion resistance,[29,79] and rollers for wear resistance.[80]

Nickel alloy 625, based on nickel-chromium-molybdenum ternary system, is a solid-solution strengthened alloy. Molybdenum, in addition to niobium, is added to

stiffen the nickel-chromium matrix, and thereby provides high strength without a strengthening heat treatment. In the wrought condition, MC and M_6C (rich in nickel, niobium, molybdenum, and carbon) are the primary carbides which distribute uniformly in the γ matrix and add additional strength through dispersion hardening to the alloy. In addition, $M_{23}C_6$, a chromium-rich carbide, which appears in solution treated material, distributes along grain boundaries and stabilizes grain boundaries against excessive shear. Although nickel alloy 625 contains small amounts of aluminum and titanium, it is not usually considered as an age hardenable superalloy. However, as a consequence of its content in Nb, precipitation of the metastable ordered γ'' phase (a $Ni_3(Nb,Al,Ti)$ coherent body-centered tetragonal) and stable δ phase (a $Ni_3(Nb,Mo)$ incoherent orthorhombic) does occur during long term aging of solution treated alloy. This alloy can also be further strengthened by aging treatment.[25,26,74,81-84]

Welding of Nickel Alloy 625

Nickel alloy 625 is generally considered having good weldability as compared with other nickel based superalloys because it is free from strain age cracking.[24,25,85] However, it is still quite susceptible to solidification cracking during welding.[86,87] Solidification cracking has been found in dissimilar metal welding[30] and cladding[29] with nickel alloy 625.

The as-welded microstructures of nickel alloy 625 are quite different from that of the wrought material. Strong segregation of the alloying elements forms a composite-like structure with interdendritic area which is richer in niobium than corresponding dendritic area. Eutectic-like constituents are formed in the interdendritic area during casting and welding.[18,87-96] Laves phase and Nb-rich carbides, as examples of the

constituents, are produced as the result of strong segregation caused by non-equilibrium weld metal solidification and always distributed in the interdendritic region. The general formula of Laves phase is $(Fe,Cr,Mn,Si)_2(Nb,Mo,Ti)$. Excessive amounts of Laves phases will impair room temperature tensile ductility. The solidification characteristics of nickel alloy 625 have been studied and the phases found in the as-welded alloy are listed in Table 2.2.[87,91,97]

A comprehensive comparison of weldability of nickel alloy 625 with other heat resistant superalloys and stainless steels has been carried out by Arata *et al.*[86] Hot ductility characteristics and weld cracking susceptibility of those alloys have been investigated using weld thermal cycle simulator, Varestraint, and Trans-Varestraint test. The brittle temperature ranges had been determined. The ductility of nickel alloy 625 showed a drastic decrease to zero near nil ductility temperature. Although some of the ductility characteristics of nickel alloy 625 are comparable to that of 316 stainless steel, the cracking susceptibility is substantially higher than that of the stainless steel. Among heat resistant superalloys, such as Inconel 617, Hastelloy X, and Incoloy 800, nickel alloy 625 has a moderate cracking tendency.

Cieslak[87,91] has further studied the alloying element effect on weldability. A statistically designed matrix varying in C, Si, and Nb content has been employed to determine the individual effects of those elements. The Varestraint test was used as the evaluation tool. The correlation between the alloy chemistry, solidification microstructure and weldability (solidification cracking susceptibility) was established. It was concluded that the formation of Nb-rich eutectic constituents was primarily responsible for the increased susceptibility to solidification cracking. However, the influences of welding

condition on the formation of Nb-rich eutectic constituents and further on the weldability were not studied.

Table 2.2 Summary of the Phases Found in Nickel Alloy 625 Weld Metal

Phase	Structure	Morphology	Composition	Melting range
Matrix	FCC	Dendritic	Ni, Cr	1360-1285 °C
Laves	Hexagonal	Lamellar	Ni, Fe, Cr, Nb, Mo, Si	1148 °C
MC	Cubic	Blocky	C, Ni, Cr, Nb, Mo	1246 °C
M_6C	Diamond Cubic	Irregular	C, Ni, Cr, Nb, Mo, Si	1206 °C

Heubner *et al.*[98] investigated the solidification behavior in directionally solidified nickel alloys. The equilibrium solidification ranges and melt equilibria of nickel alloy 625 had been determined. Partition coefficients of the alloy components as a function of temperature had been measured by isothermal holding and quenching during solidification. Segregation behavior of each component corresponded with the equilibrium model under such solidification condition.

STRUCTURE of WELDMENT

In dissimilar metal welding, the weldment is a chemically heterogeneous composite consisting of six metallurgically distinct regions defined as (1) the composite zone, (2) the unmixed zone, (3) the weld interface, (4) the partially melted zone, (5) the heat-affected zone, and (6) the unaffected base metal, as illustrated in Figure 2.2.[42,99-101] The composite zone in a weld is the part where filler metal and melted base metal are completely mixed. The unmixed zone in a weld is the part where base metal has been melted due to the heat of the weld, but not mechanically mixed as in the composite

region, and it has an identical chemical composition to the base metal. However, its microstructure differs from both composite zone and base metal. The weld metal (fusion zone) is a combination of those two zones. Separated by the weld interface, is the partially melted zone where some localized melting in base metal such as second phase particle dissolving may occur. The heat-affected zone (HAZ) and unaffected base metal will not be discussed in this study. However, in autogenous welds or weld made with matching filler metal, the unmixed zone does not exist as a distinguishable zone. It is virtually identical to the composite zone in terms of solidification structures and chemical composition, and no interface can be drawn in between (except some heavily segregated base metals may also produce a distinguishable unmixed zone[102]).

The factors affecting the unmixed zone such as welding method and heat input, have been studied.[99-101] It is concluded that the unmixed zone exists in heterogeneous welds regardless of the welding method, and a higher heat input and greater penetration produce a wider unmixed zone generally. It is also suggested by Matthews and Savage that a larger unmixed zone is expected when the melting range of the filler metal is equal to or greater than that of base metal. A more recent study has focused on its adverse effect on the weld metal corrosion resistance.[103] However, the presence of the unmixed zone effect on the microstructure development has not yet been studied.

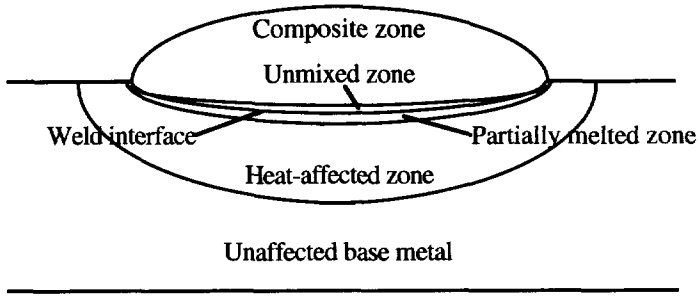

Figure 2.2 Metallurgical Zones in a Typical Weld.

WELD METAL SOLIDIFICATION

Microstructure Evolution

The solidification of metallic alloys is generally considered as a nucleation and growth process. Although it is true that in the case of ingots and castings, it has been concluded by many researchers in welding (autogenous weld or weld made with matching filler metal) that the nucleation event is insignificant and the control mechanics of weld metal solidification is an epitaxial growth.[37-44] That is, the molten weld metal solidifies on the pre-existing lattice sites in the partially molted grain of the heat-affected zone. As a result, the heterogeneous nucleation event in welds is eliminated during the initial stage of weld metal solidification.

Epitaxial and Non-epitaxial Growth in Welding

The understanding of the fundamental aspects of the solidification mechanism and grain structure development in the fusion zone of conventional welding has increased substantially during the past 30 years. Essentially, there are two distinguishable solidification modes in fusion welding, epitaxial growth mode and independent nucleation (non-epitaxial) mode. They are followed by competitive growth (although the independent nucleation does not necessarily occur as the first step as the weld pool solidifies). The fundamental concepts of epitaxial growth and competitive growth during weld metal solidification were established in the 1960's by Savage and his colleagues.[37–40] They proposed that no nucleation event was necessary to initiate weld pool solidification. Solidification mechanism in fusion welds is a process of epitaxial

growth from the partially melted base metal at the fusion boundary where a perfect or near perfect wetting of the base metal by the molten weld metal and favorable substrate characteristics precludes the distinct nucleation. However, in the bulk weld metal, grain growth is a process of competitive growth where grains with their easy growth direction parallel to the direction of the maximum temperature gradient will grow more easily and crowd out other less favorably oriented neighboring grains. The easy growth direction for f.c.c. and b.c.c. metals is <100>.[38,104-106] This preferential growth in the <100> direction is thought to be because the <100> is the least close packed, as crystallization occurs from the random atomic arrangement in the liquid, the looser packing of atoms in this direction effectively allows a faster growth than in other closer parked directions. Further investigation focused on the epitaxial growth was conducted by Loper and coworkers[41,105] who expounded the microstructural development in conventional autogenous GTA welding. They concluded that no mechanism of solidification at the fusion boundary other than epitaxial growth mechanism occurred. They summarized the relationships of epitaxy, nucleation, and grain growth.

The microstructure in the weld fusion zone was profoundly influenced by the partially melted base metal grains.[41,105] Favorably oriented partially melted base metal grains resulted in nucleation-free growth in the fusion zone, whereas unfavorably oriented partially melted base metal grains induced a nucleation event in the bulk weld metal. Statistically, the percentages of nucleation free growth and nucleation growth in the entire weld metal were 30% and 70%, respectively, in their study. The closer the partially melted base metal grains oriented to the unfavorable <111> direction, the greater the possibility for nucleation to occur near the fusion boundary. Nucleation in the fusion zone requires a favorable crystallographic growth orientation, favorable thermal conditions and impurities in the weld metal.[105] More studies on nucleation in the fusion

zone have been conducted by Kou *et al.*[107-110] They described some favored conditions for other types of nucleation taking place in the weld fusion zone,[107,108,110,111] and these new grain were internal epitaxial columnar grains when the weld was oscillated, and equiaxial grains caused by dendrite fragmentation.

In 1979, Loper and Gregory[112] published the most extensive study on non-epitaxial growth in fusion welding where significant high welding travel speed (from 210 to 850 mm per second) was used in autogenous welds on aluminum alloys. Epitaxial growth was eliminated and non-epitaxial growth became a dominant factor in such welds. Non-epitaxial growth created a metallurgical grain boundary (referred as type B grain boundary by Matsuda[113]) near the fusion boundary which separated the partially melted base metal grains from the fusion zone grains. Also epitaxial grain growth still existed to some extent but it was quickly eliminated by surrounding non-epitaxial grains which were more favorable in growth direction. In the case of the non-epitaxial growth, microstructure developed in weld fusion zone became independent from base metal microstructures. In the absence of epitaxial growth, the microstructure in the fusion zone was essentially a single crystal structure, only low angle grain boundary maybe presented.[112] This study has also found that high welding travel speed, small base metal grain size and narrow weld bead all tend to favor non-epitaxial growth.

The non-epitaxial phenomena were also observed by Baikie and Yapp[114] in 316 stainless steel multipass welds where nucleation was found in partially melted grains which had a less favored orientation (for example, 30°). More cases were found in laser irradiation situations where the cooling rate was about 10^6 to 10^8 °C per second.[115,116] Based on these works, it was predicted by Brook and Mahin[117] that more cases of non-epitaxial growth were expected with the increasing research in the area of rapid

solidification. However, whether the non-epitaxial growth is truly dependent on rapid solidification or not is still a question. Devletian and Wood[43] have studied the capacitor discharge welding where the solidification rate is about 10^6 °C per second yet the grains still form epitaxially in the fusion zone.[44] Noticeably, all of those studies were carried out on autogenous or matching filler metal welds. In the case of dissimilar welding, although it has been observed that epitaxial growth seldom occurs between clad metal and base metal,[5] no further study has been conducted.

It is important to study the solidification of electroslag strip cladding because it directly affects the cladding properties and the formation of defects in cladding. Both the technical importance and theoretical importance are obvious. Weldability and the mechanical properties of fusion welds are affected by the microstructures developed during weld pool solidification in the weld fusion zone (if the base metal's response to the welding is to be neglected). In welding, the molten weld pool shape can profoundly influence grain orientation produced during weld metal solidification and affect weldability.[38] It was observed by Savage *et al.* that welds made with a tear drop shape weld pool were more susceptible to solidification cracking than welds made with an elliptical shaped pool.[118] Davies and Garland[119] pointed out that this is because in a tear drop shaped weld pool, low melting point segregates tend to be trapped at the grain boundaries along the weld centerline when the essentially straight columnar grains[120] growing from opposite sides of the weld pool impinge against each other. In an elliptical shaped weld pool, on the other hand, curved columnar grains growing perpendicular to the trailing edge of the pool do not impinge against each other. Therefore, they do not trap low melting point segregates along the weld centerline. It is also true that fine-grained welds are less susceptible to solidification cracking than coarse-grained welds. This is due to the fact that in fine-grained welds low melting point segregates tend to be

distributed over a larger grain boundary area and, therefore become less harmful.[121,122] The microstructures produced in fusion welds have always resulted in anisotropic mechanical properties of the weld deposit.[38,123,124]

Microsegregation

Microsegregation, that is, segregation of solute elements over distances on the order of dendrite arm spacings.[125] The origin of the microsegregation in cladding is the result of the uneven redistribution of solute accompanying the solidification of an alloy. It affects mechanical properties, corrosion properties, and workability of ingot. In welding, it is such segregation that produces a microstructure susceptible to solidification cracking to a degree dependent upon the extent of segregation and the components which are segregating.[126] The extent of microsegregation in the alloy structures can be determined experimentally by measuring one of the following: (a) amount of non-equilibrium eutectic constituent, (b) amount of non-equilibrium second phase, (c) ratio of minimum to maximum element concentration.

The equilibrium partition coefficient (distribution coefficient) k is defined as the ratio of solute concentration in solid to solute concentration in liquid at a particular temperature. It can be obtained by the liquidus and solidus lines over the solidification interval of a phase diagram. It is influenced by the diffusion of solute in the liquid, diffusion of solute in the solid, convection, turbulence, and solute trapping. The equilibrium partition coefficient k equal to one, means an even distribution of solute in solid and liquid. The further the k of an element deviates from the unity, the greater that element segregates. Although, under equilibrium solidification conditions, the solute distribution across the solidification path is equilibrated, the value of the partition

coefficient k does not reflect the segregation behavior in solidified alloy. However, in non-equilibrium solidification, it has been a primary indictor to the segregation.

In the complex alloy system, such as nickel alloy 625, the partition coefficient can only be determined experimentally. A significant change of partition coefficient over the solidification range has been reported,[98] and it also has been described as a function of temperature. For solutes which exhibit distribution coefficients less than 1.0, the molten weld metal becomes enriched in that solute ahead of the solid-liquid interface. As solidification proceeds, this enriched liquid freezes in the dendritic boundaries.[126]

In nickel alloy 625, niobium has been the strongest element that segregates,[98,127] As the result of such segregation, elements like niobium, molybdenum *etc.* are substantially concentrated in the interdendritic region. As the interdendritic liquid solidifies, Laves phase, a non-equilibrium product forms in the interdendritic region.

The cooling rate at a given location in the weld is the product of the temperature gradient and the solidification growth rate (G x R = cooling rate, G is the thermal gradient at dendrite tips, R is the solidification rate in the direction of dendrite advance). For many alloys, there is an empirical correlation between the dendrite arm spacings and the cooling rate.[128,129] The correlation exists for both primary and secondary dendrites. Caution must be taken to accurately measure the primary dendrite arm spacings. Because the primary dendrite usually doesn't line-up well for direct measurement, while secondary dendrite arms line-up on the stems of primary dendrites. It should be noted that dendrite coarsening can also lead to a false result. The dendrite arm spacings are determined experimentally from the microstructures. Therefore, the local solidification time can be calculated using a correlation with experimental data. For nickel alloy 625,

the correlation between primary dendrite arm spacings and cooling rate has been determined[98] to be:

$$\lambda = 758.3\ (Cooling\ rate)^{-0.4} \qquad [2.1]$$

MODELING of WELD METAL SOLIDIFICATION

Solidification modeling has shown an increased importance in modern industry. The potential to influence the microstructure through extensive hot forming and high temperature annealing has been limited. Many parts are used in the as-solidified (as-cast or as-welded) condition, as in net shape casting and surfacing. Controlling the solidification process has been the only method to obtain better microstructures.

Solute redistribution during solidification in complex alloy systems is important, since it profoundly influences the weldability or castability and mechanical properties of the solidified alloy. Many models developed for binary alloys have been used for the complex multi-component alloys based on an assumption that the individual alloy component does not influence each other with respect to segregation behavior, and often it is under the assumption that the partition coefficient applied at the interface is a constant throughout solidification. Although Brody and Flemings[130] showed that the assumption of constant partition coefficient may not always be valid, this assumption has been continuously used in many models. In the binary alloy system, the partition coefficient can be obtained from the equilibrium phase diagram of the alloy system. In the complex alloy system, such as nickel alloy 625, the partition coefficient can only be determined experimentally. It has been found in the literature that for the same alloy

system (*e.g.* nickel alloy 625) different models often use a different partition coefficient value. Some uses the value directly from binary system, some uses experimental value. To overcome the discrepancy between model and experiment, many have adjusted the partition coefficient k to a effective partition coefficient k_e or k_{ef} which has no physical meaning regarding to the alloy system at all. A significant change of partition coefficient over the solidification range has been reported,[98] and described as a function of temperature. This should be taken into account when models the complex alloy systems, such as nickel alloy 625, and this would significantly improve the modeling of the solute redistribution behavior in those alloy systems.

In a binary alloy, under equilibrium conditions (complete solute diffusion in both solid and liquid), by applying the lever rule, the following equation is derived:

$$\frac{C_L}{C_0} = [1 - (1-k)f_S]^{-1} \qquad [2.2]$$

where C_L is the solute concentration in the liquid;

C_0 is the initial element concentration;

k is the equilibrium partition ratio; and

f_S is the weight fraction of the solid.

This equation could be used in calculating the solute concentration during the equilibrium solidification. However, in the real world, liquid metal rarely solidifies under equilibrium conditions. It is virtually always under non-equilibrium conditions such as in casting and welding.

The first theoretical treatment of microsegregation in the non-equilibrium solidification condition was given by "Scheil" equation [2.3]. It assumed that complete solute diffusion in liquid and no diffusion in solid. Other assumptions such as no mass flow into or out of the volume element, constant physical properties, and fixed volume element size were also applied.

$$C_s^* = k\, C_0\, (1 - f_s)^{(k-1)} \qquad [2.3]$$

where C_s^* is the solute concentration in the solid at the solid/liquid interface.

The Scheil equation predicts generally greater microsegregation than that found experimentally. The discrepancy between predicted and actual microsegregation measured experimentally arises mainly from back diffusion in the solid.

Brody and Flemings[130,131] were the first to account for diffusion in the solid during dendritic solidification. They approximated the solute concentration gradient at the solid/liquid interface during solidification and derived the solutions as the following: Eq. [2.4, 2.5].

$$C_s^* = k\, C_0 \left[1 - \frac{f_s}{1+\alpha k}\right]^{k-1} \qquad [2.4]$$

for the linear rate of the interface advancement and

$$C_s^* = k\, C_0\, [1 - (1 - 2\alpha k)f_s]^{(k-1)/(1-2\alpha k)} \qquad [2.5]$$

for the parabolic rate of the advancement, respectively, and the α is the diffusion Fourier number, which represents the extent of diffusion of solute in the solid; it is defined as $\alpha = D_s \frac{t_f}{\lambda^2}$

where D_S is the solute diffusivity in the solid;

t_f is the local solidification time; and

λ is the one-half of the dendrite arm spacing.

This model predicted a reasonable solution only when $\alpha k < 0.1$. When the solid diffusion became significant factor, mass balance can not be preserved with this model. Considering this model must reduce to the Scheil equation [2.3] for no solid diffusion and to equation [2.2] for complete diffusion, Clyne and Kurz[132] have modified this model and added a spline fit to match the Scheil equation and equilibrium equation for infinitesimal and infinite diffusion coefficients, respectively, so that these extreme conditions can be fully satisfied. They defined an α' to substituted α in Brody and Flemings' model. Their definition of α' for parabolic growth is shown in Eq. [2.6]. It has been pointed out by Kobayashi[51] this approach overestimated the extent of diffusion in the solid and, therefore, underestimated microsegregation. And the α' is not constant during solidification, it is a function of α, k, and f_S.

$$\alpha' = \alpha\left(1-e^{-1/\alpha}\right) - \frac{1}{2}e^{-1/\alpha} \qquad [2.6]$$

Kobayashi[51,133] derived an analytical solution for solidification with parabolic growth. The solution was given by an infinite series expansion, and offered the most accurate results. However, the number of terms required to generate an accurate solution were excessively large (more than 10,000 terms) for small values of α and k. Thus, it is very difficult to use his model for practical purposes. Furthermore, his model was derived with the assumptions of constant equilibrium partition ratio and constant diffusivity. These assumption are not valid for most complex alloys, for example, the

equilibrium partition ratio of certain element in nickel alloy 625 can vary over 30% of its value over the solidification range,[98] so that this model cannot be properly applied.

The diffusion of solute in liquid can generally be ignored especially in case of dendritic solidification because of the relatively high diffusivity (D_L is approximately equal to 10^{-9} m^2s^{-1}) and the small diffusion distances within the interdendritic liquid (approximately 10 to 100 μm). The extent of diffusion in the solid varies widely depending on the nature of the solute atoms.

To reduce segregation and eliminate Laves phase in nickel alloy 625 casting, Sawai *et al.*[127] have studied the microsegregation behavior in directionally solidified casting. Matsumiya's 1-D finite difference model[134] was used in predicting the formation of Laves phase. A lower liquid concentration was predicted at a given temperature especially for small partition coefficient elements. It was suggested that increasing cooling rate during solidification produced a finer dendrite structure which could reduce the amount of the Laves phase. Meanwhile a stronger segregation behavior of Nb and Mo which led to the formation of Laves phase was also observed with the increased cooling rate. A substantially low threshold was used in the model to predict more Laves phase in the interdendritic region.

Sarreal and Abbaschian[135] have studied the effect of solidification rate on microsegregation. A broad range of solidification rate from slow to rapid ($6x10^{-2}$ to $1x10^5$ K/s) was examined and compared with the classical non-equilibrium models. The difference between the models and experimental results was found in the prediction of the eutectic fraction, and the error in the prediction was assumed mainly due to lack of consideration in dendrite tip undercooling, related to the solute built-up at the dendrite tip, and eutectic temperature depression. Progress was based on the Brody and Flemings'

work. A newer model including the effects of dendrite tip undercooling and eutectic temperature depression was proposed by Sarreal and Abbaschian.[135] Still a constant partition coefficient k was applied for all solidification rates in this model. Giovanola and Kurz[136,137] have also studied the microsegregation under rapid solidification conditions. The assumption of complete mixing in the liquid used in many other models has been found invalid in the rapid solidification conditions. In their semi-empirical approach, both solute distribution in the interdendritic liquid and solute diffusion in solid was accounted. The model predicted a realistic microsegregation under rapid solidification condition. However, in both the above mentioned models, a constant partition coefficient k was used. The concept of the Péclet number used for high rate solidification has been ignored. It would have helped to predict a less segregation behavior if the significantly increased partition coefficient were used under high solidification rates.

WELD METAL SOLIDIFICATION CRACKING

Weld metal solidification cracking has been a major and persistent problem in a variety of engineering alloys. It has been the subject of many extensive studies for several decades.

Mechanisms of Solidification Cracking

Borland's Generalized Theory[138] of solidification cracking has been the most widely accepted one in explaining the mechanism of solidification cracking. In the Generalized Theory, cracking is explained by considering four stages during the solidification of weld metal: In the first stage - dendrite formation, free growth of

dendrites into a continuous liquid takes place and no cracking can occur. In the second stage - dendrite interlocking, impingement of growing dendrites causes interlocking. The liquid remains continuous in the interdendritic regions and healing occurs if any cracking may form. The third stage - critical solidification range, grain boundaries start to form when very little liquid remains. Cracking can not be healed if the strains exceed the strain tolerance of the material. The fourth stage - completion of solidification, the solidification completes, no liquid remains and no solidification cracking occurs. According to this theory, the weld metal solidification cracking is a result of the competition between the material resistance to cracking and the mechanical driving force for cracking. Like many other cracking phenomena, cracking occurs when the mechanical driving force exceeds the (endurable limit of) materials resistance. The mechanical driving force (strain) is raised by not only the internal contraction of the weld metals, but also the external deformation caused by parent metal movement due to the rapid local heating and cooling cycle. Stress is often tension stress in the cladding bead when nickel alloy 625 or other soft materials deposit on low alloy steel.[139] In the case of cladding, reducing cladding speed or preheating the base metal will decrease tensile stress level in the cladding.

Factors Affecting Solidification Cracking

Factors affecting weld metal solidification cracking can be considered either metallurgical or mechanical origin.[138,140-148] The metallurgical factors relate to the conditions of solidification of the metal, the grain size and morphology, the presence of low melting eutectic films, etc. and those affecting the extent of the critical solidification range. The mechanical factors relate to conditions of stress/strain build-up in weld metal during solidification resulting from transient, non-uniform heating and cooling at various weld and near-weld positions.[58,95,124,126,139,149-171]

Trace elements: The early work performed by Pease,[172] Owczarski,[45,173,174] and others regarding tramp elements such as sulfur, phosphorus, lead, etc. was excellent and is still a good guideline to follow with respect to alloy trace element limits. Although almost all of the detrimental trace elements have been eliminated to a substantially low level by today's processing technology, the possibility of contamination during welding has become significant.

Factors affecting solidification cracking formation in welding from a materials composition standpoint have been summarized by Cieslak[87,91] as listed below.

I. From a materials composition standpoint, there are three reasons for hot cracking to occur in an alloy.

The nominal alloy matrix, excluding impurities, has a wide solidification range.

An intentional alloy addition may cause the formation of a low melting point constituent, such as a eutectic, which could wet solidification grain boundaries at temperatures well below the equilibrium solidus.

Impurity elements strongly segregate to interdendritic regions and grain boundaries where they either form low melting point constituents or lower the surface tension of the final solidifying liquid. Most of the low melting point constituents formed by impurities have a very brittle property even when they are solidified.

II. From a welding process point of view, the following factors are all process related.

Magnitude of the thermal strain induced during the welding is determined by the welding process, welding variables, weldment configuration and materials' thermal properties.

The morphology of solidification structure has a great effect on the formation of hot cracking.[146,175]

Solidification mode, which has been a primary factor affecting hot cracking in stainless steels, is both compositional and process dependent.[176-178]

Welding alloying vector indicates which elements are introduced into the weldment and which elements are lost or diluted during welding process. This should also be an additional consideration for compositional factors.

III. Status of base materials:

Base metal microstructures prior to welding may affect cracking susceptibility.[41,179]

Features of Solidification Cracking

Hot cracking in welding can be categorized in the chart shown in Figure 2.3. In many cases, more than one type of cracking occurs in the same weld. However, the solidification cracking has its own features.[180-183] It is usually observed as grain boundary fracture. The fractured surface of the cracking shows a deep dendritic feature when cracking occurs in the temperature between near the liquidus and the bulk solidus, and it shows a shallow dendritic or flat surface when cracking occurs in the temperature range between the bulk solidus and the true solidus. Solidification cracking can often induce subsequent ductility dip cracking as temperature drops. So proper analysis of the fracture surface is important to solve welding cracking problem.

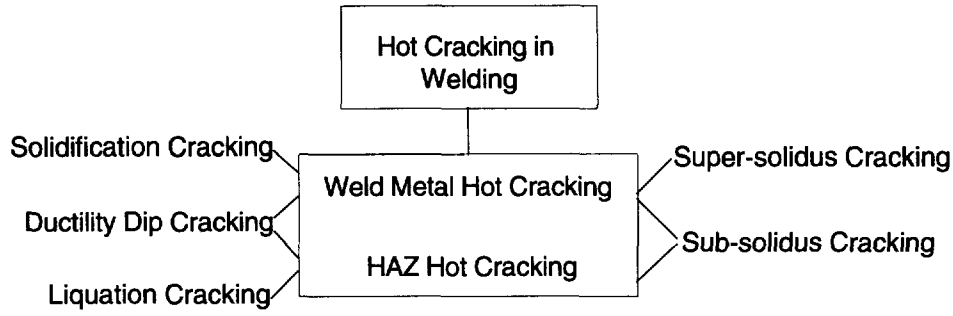

Figure 2.3 Classification of Hot Cracking in Welding.

Solidification Cracking Test

In order to investigate the tendency of weld metal solidification cracking in welding, many tests have been developed to assess the solidification cracking susceptibility of both welding material and welding process. Those testing methods can be classified into two categories: self-restraint tests and external restraint tests. The self-restraint test relies on the rigidity of specimens whereas the external restraint test requires an external load to impose an augmented restraint during testing. The imposed restraint in general is large enough so that the thermally induced restraint can be neglected. This allows the metallurgical and compositional factors associated with cracking to be isolated from the mechanical factors associated with welding process. However, the test conditions, especially the combination of thermal and mechanical history, are inherently different from actual welding conditions. This difference may result in disparate cracking behavior in the external restraint test relative to actual welding. The primary advantage of a self-restraint type test is that it requires no additional equipment or apparatus. And human operating error could be limited in this test as compared with modified varestraint-transvarestraint test (MVT) where inconsistent results were found for clad metal[56,95]

Although, there are numbers weldability tests available to assess the weld metal solidification cracking susceptibility during the welding,[56,57,184] none of them can be easily adopted in the strip surfacing process. The Canadian standard GBOP (Gap Bead-on-Plate) test was found insensitive to cracking in strip surfacing process.[18] Other attempt using the existing test (Varestraint test and MVT) for strip surfacing process can be found in references (58,59). It was found that those tests produced an altered weld metal microstructure different from that of ESS in the present study. Therefore, such test results could not represent strip surfacing condition. Since solidification cracking in the weld metal is a material, structure, and process dependent factor, consequently any test method which produce an altered microstructure could not represent strip surfacing condition.[58,59] A new testing method has been developed to meet the need to evaluate the solidification cracking tendency in order to make assessment on welding materials and process parameters.

CHAPTER III

EXPERIMENTAL PROCEDURES

MATERIALS

The materials used in this study can be categorized into three groups. They are filler strip electrodes, base metals (substrate), and surfacing fluxes. In the process optimization study, nickel alloy 625 strip electrode, MIL-S-23284 class 1 steel base metal, and electroslag surfacing (ESS) flux (submerged arc surfacing flux for comparison only) were used. In the study of clad metal solidification, class 1 steel and several types of stainless steels were used as base metals, while nickel alloy 625, 70/30 copper-nickel, stainless steels, and mild steel were used as filler strip. In the weld metal solidification cracking assessment, the nickel alloy 625 was compared with other filler metals including nickel alloy 59, 70/30 copper-nickel, 70/30 nickel-copper, 308L stainless steel, and nickel 200. MIL-S-23284 class 1 steel was used as base metal.

Surfacing Strips

Composition and melting temperatures of the strip electrode filler metal used in the present study are shown in Table 3.1 Among those filler metals, nickel alloy 625 was the primary filler metal used in all studies. The 30 x 0.5 mm nickel alloy 625 strip electrode was produced by vacuum induction melting (VIM) then electroslag remelting (ESR) and supplied in cold rolled condition. Other strip filler metals were used for either

the cladding interface study or the solidification cracking study. These filler strips include: nickel alloy 59, 70/30 Cu-Ni, 70/30 Ni-Cu, Ni 200, 308 stainless steel, and mild steel.

Table 3.1 Compositions (wt%) of Strip Electrode Filler Metals

Element (wt%)	Nickel Alloy625	Nickel Alloy 59	70/30 Cu-Ni	70/30 Ni-Cu	Nickel 200	308L Stainless	410 Stainless	Mild Steel
C	0.03	0.01	0.02	0.02	0.02	0.03	0.14	0.25
Mn	0.03	0.15	0.73	3.54	0.30	1.96	1.15	0.97
Fe	0.95	0.34	0.55	0.52	0.07	BAL.	BAL.	BAL.
S	<.001	0.003	0.001	0.001	<.001	0.001	0.02	0.019
Si	0.04	0.04	0.04	0.17	0.12	0.45	1.11	0.31
Cu	0.03		66.99	28.64	0.02	0.07		
Ni	63.45	60.90	31.25	65.10	96.41	10.2		
Cr	22.50	22.50				20.5	12.3	
Al	0.26	0.31		0.03	0.04	0.26		0.001
Ti	0.19		0.42	1.98	3.02	0.19		0.04
Mo	9.32	15.50				0.42		
Nb	3.47	0.23				0.03		
P	0.005		0.001	0.001	0.001	0.01	0.03	0.03
Melting Temp. °C	1285	1310	1170	1308	1435	1400	1483	1505

Base Materials

MIL-S-23284, Class 1 steel was used as the primary base metal in this study (A36 steel was also used occasionally) except in the interface study where the stainless steel 304 and 316 were used. The composition and melting temperature of the base

metals are listed in Table 3.2. The surface condition of base metal to be clad was machined or ground to bare metal. Surface roughness was always maintained approximately RMS = 3.25×10^{-3}mm (RMS = 130μin, about 63P) or better.

Table 3.2 Compositions (wt%) of Base Metals

	MIL-S-23284 Class 1 Steel	A36 Steel	304 Stainless Steel	316 Stainless Steel
C	0.25	0.27	0.04	0.04
Mn	0.34	1.20	2.01	1.75
Fe	94.86	98.02	68.73	64.26
S	0.013	0.05	0.01	0.01
Si	0.22	0.25	0.86	0.33
Ni	3.21		8.81	12.21
Cr	0.42		19.3	18.52
Al	0.005		0.001	0.001
Ti	0.001		0.02	0.01
Mo	0.44		0.19	2.85
V	0.06		0.001	0.001
P	0.006	0.04	0.03	0.02
Melting Temp. °C	1505	1510	1400	1378

Surfacing Fluxes

Agglomerated fluxes were used for both ESS and SAS processes. The major chemical ingredients of the fluxes are listed in Table 3.3

Table 3.3 The Major Chemical Ingredients of the Surfacing Fluxes

ESS flux			
$MgO+CaO+CaF_2$	Al_2O_3	SiO_2	$Li_2O+Na_2O+K_2O$
70	20	8	2

SAS flux				
$MgO+CaO+CaF_2$	SiO_2	Al_2O_3	FeO + MnO	Na_2O+K_2O
45	20	10	5	5

WELDING EQUIPMENT

The Union Carbide, Linde series VI-1200 CV/DV, a direct current, constant voltage power supply was used for both ESS and SAS process. Electrode positive was set for both ESS and SAS processes. The equipment setup is illustrated in Figure 3.1 The welding current, being an indirect parameter, was controlled by the adjustment of the strip electrode feeding rate. A high capacity shunt was linked to the welding head and the potential over the shunt was monitored then converted to the welding current. Welding voltage was directly adjusted in the power supply control box, and it was also monitored and recorded between contact shoes and work pieces. The travel speed was controlled by Linde UEC-7 control unit. The characteristic volt-ampere output of the power source is shown in Figure 3.2. In this experiment, current and voltage were not totally unrelated. Changing each of the process variables also altered the physical state of cladding pool and this change also had inevitable effects on the other process variables. For instance, increasing travel speed would naturally decrease cladding current, due to decreasing depth of cladding pool and reducing heat input in the cladding. In order to keep the same current level, proper adjustment was needed (strip feed rate was increased).

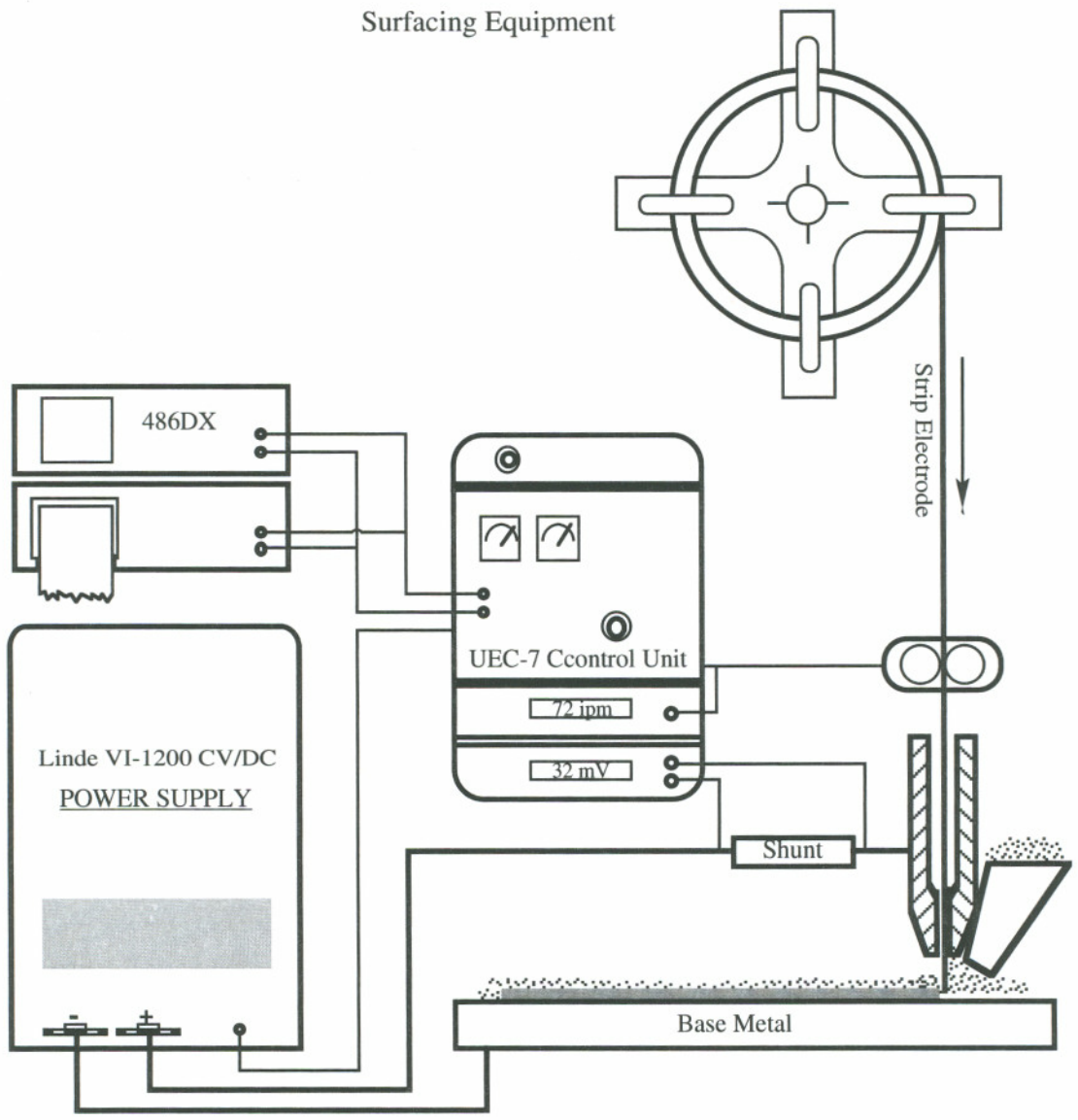

Figure 3.1 The Surfacing Equipment Setup

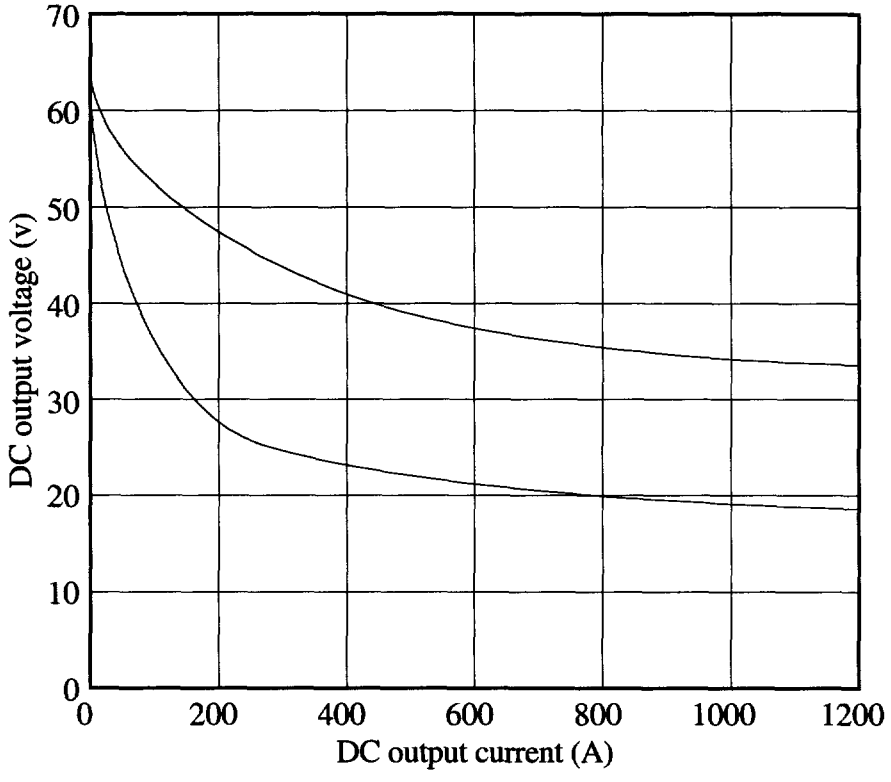

Figure 3.2 The Output Volt-Ampere Characteristics of the Power Source: Curve A and B are the power source's upper limit and lower limit, respectively. The output A/V curve can be adjusted between A and B by the voltage control.

ELECTROSLAG SURFACING PROCESS

Surfacing Process Variables

A comprehensive parametric study was conducted in a systematic series of tests on the ESS process to statistically evaluate the effect of each independent process variable upon dependent process responses consisting of deposition rate, penetration, dilution, and bead shape. Duplicated surfacing conditions were used on SAS for comparison purpose (to establish a common ground, compare with popular industry process). The

independent experimental variables mainly consist of cladding current, voltage, and travel speed. The final optimum condition was evaluated in the order of acceptable dilution, highest possible deposition rate, and a sound bead shape (wetting angle < 70°) with a stable ESS mode.

Bead-on-plate claddings were deposited on 25 mm (1") thick MIL-S-23284, Class 1 steel. Selected claddings were longitudinally sectioned to inspect for a uniform penetration pattern along the entire cladding bead. All claddings were transversely sectioned for image analysis evaluation. The cross-sectioned samples were grounded to 600 grit, then diamond polished to one micron finishing. The base steel was etched with 2% nital to make the cladding deposit and base metal distinguishable.

Light Image Analysis

LECO L2001 image analyzer was used to measure features of cladding cross section. A special method was developed for this analysis by using a predefined line coupled with live image. This technique enables the system to determine the dilution and penetration of the cladding. Due to the no attack on cladding bead (composite zone) by the 2% nital, the composite zone remained as mirror polished condition and acted like a black whole (total reflection, zero light intensity) when CCD camera took the image of specimen into the image analyzer. The heat-affected zone and unaffected base metal reacted differently to the etchant and gave a different lighting contrast (diffuse reflection). Figure 3.3 shows the image analysis procedures. The predefined line separated the composite zone (same lighting intensity in image analyzer) into two areas, a reinforcement area and penetrated area. The penetration could then be determined, so as the dilution level. The bead shape factor (wetting angle, bead height, Bead width) and HAZ size were also measured from image analyzer. The deposition rate was calculated

based on the cross section area. The program for the image analysis is listed in Appendix A.

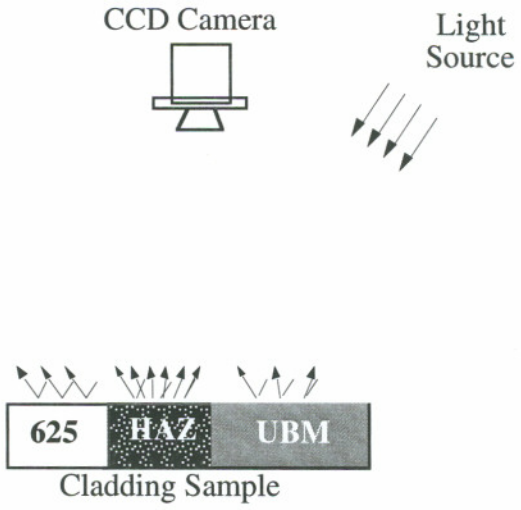

Figure 3.3 Showing the Image Analysis Procedures.

The dilution is defined as:

$$\% \, Dilution = \frac{B}{(A + B)} \% \qquad [3.1]$$

where A is the transverse cross sectional area of the surfacing reinforcement above the base metal surface and B is the cross sectional area of the melted base metal below the base metal surface as shown in Figure 3.4.

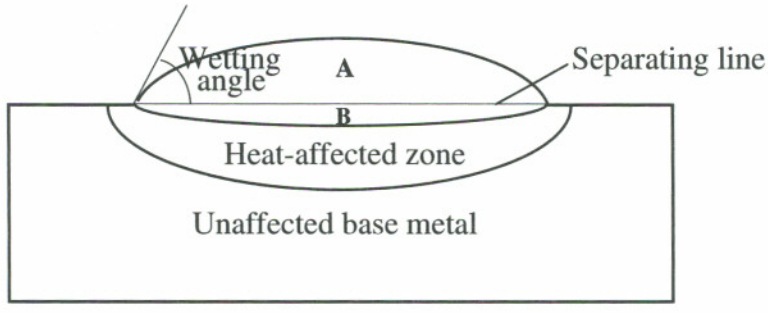

Figure 3.4 Illustration of the Transverse Cross Section of Surfacing Deposit.

Chemical Composition of Cladding

Multiple layers of nickel alloy 625 were deposited. Samples measured 1" cubic were taken from each layer with top surface grounded to 400 grit. The samples were then analyzed by spark emission spectroscopy. Alloying vectors for both ESS and SAS processes were calculated based on the fourth layer composition to minimize the dilution effect from base metal.

WELD METAL SOLIDIFICATION

The studies on the weld metal solidification included: weld metal interface characterization, weld metal microstructure initiation and growth, weld metal solidification structure, and weld metal solute segregation. In the studies of weld metal interface characterization and weld metal microstructure initiation and growth, different combinations of filler metal strips and base metals were used. Both dissimilar and matched filler metal cladding were produced by ESS process. Such combination of several materials covered a wider range of melting temperature difference between the filler metals and base metals and this gave us the advantage of investigating the temperature effect on the unmixed zone in the weld metal. Table 3.4 is the list of different filler and base metals used in this study. Nickel alloy 625 and low alloy steel were mainly used in the studies of weld metal solidification structure and weld metal solute segregation in the ESS process.

Table 3.4 Combination of Filler Metal and Base Metal Used in Weld Metal Solidification Study

Filler Metal	Base Metal	Welding Process
Nickel Alloy 625	Class 1 Steel	ESS
Nickel Alloy 625	Stainless Steel 304	ESS
Nickel Alloy 625	Stainless Steel 316	ESS
–	625 Deposit	GTA Remelting
–	70/30 Cu-Ni Deposit	GTA Remelting
70/30 Cu-Ni	Stainless Steel 304	ESS
Stainless Steel 304	Stainless Steel 304	ESS
Class 1 Steel	Stainless Steel 304	ESS

Quenched Interface Studies

Pressurized water was applied to the cladding pool to partially remove molten weld metal and slag pool to reveal the cladding metal solid/liquid interface and to obtain quenched weld metal. Due to the large slag pool size, pressurized water jet could only effectively remove portions of the molten pool (about 1/3), therefore, multiple runs were conducted such that each aimed at different portions of the molten pool. Intermediate solidification structures were obtained with the water quenched samples. The partition coefficients were also measured from the water quenched samples.

Solidification Cooling Rate

Solidification cooling rate is an important parameter in assessing weld metal solidification. Therefore, it has been a primary target in studying ESS process. Unfortunately, direct measurement of the cooling rate in the ESS cladding has been

impossible due to the severe corrosive media of the molten slag which rapidly attacks the thermocouple. Both well protected R type (Pt-13%Rh:Pt) and D type (W-3%Re:W-25%Re) thermocouples were used in the ESS process and failed to record any meaningful data. Therefore, the cooling rate for the ESS process had to be determined by other means. Indirect measurement of the ESS solidification cooling rate is based on the dendrite arm spacings and cooling rate relationship since the dendrite morphology and dendrite arm spacing are controlled by crystallographic system and solidification conditions.[104,185] Although, the relationship has been established by Heubner *et al.*[98] in directional solidification casting, it is still needed to be proven in the welding condition. Since the solidification conditions (local solidification time) in the GTA weld can be measured, the GTA remelting of nickel alloy 625 deposit has been used in this study to confirm the Heubner's relationship in welding condition.

Experiments for this weld solidification study were conducted with both ESS and GTAW processes. The welding conditions for both ESS and GTAW are listed in Table 3.5. In ESS process, nickel alloy 625 was deposited on the MIL-S-84323 steel. In GTAW process, a ESS cladding bead was remelted by the arc process. A fine wire of R type (Pt-13%Rh:Pt) thermocouple was plunged into the molten weld pool directly behind the arc along the centerline for measuring the local solidification time in the GTAW weld metal. The output of the thermocouple was recorded on strip chart recorder. The local solidification time for ESS was estimated based on dendrite arm spacing - cooling rate relationship.[98] Metallographic specimens were carefully sectioned near the thermocouple insert point and were polished through 0.05 μm alumina, they were then etched with HCl-5%H_2O_2 to reveal the general dendritic structure or electrolytic etched (2-3 V) with 10% oxalic acid to identify the eutectic constituents.

Table 3.5 Welding Variables of ESS and GTAW Used in Weld Metal Solidification Study		
	ESS (30 x 0.5)	GTAW
Current (A)	650	290
Voltage (V)	27	29
Travel Speed (mm/min.)	175	125
Heat Input (kJ/mm)	6	4

Primary and secondary dendrite arm spacings (DAS) were measured by an intercept method around the point of interest. An average value was used to determine the cooling rate.

Differential Thermal Analysis

Solidus and liquidus of the weld deposits were determined by differential thermal analysis (DTA) method. The DuPont 9900 DTA analyzer with the high temperature 1600 cell was used. The cell was calibrated using pure nickel (>99.999) and pure gold (>99.999). Pure platinum was used as reference material. The precision of this system, using R type (Pt-13%Rh:Pt) thermocouples, was determined to be better than ±2.5°C. A high capacity gas purifier was used with ultra high purity argon (research grade) to purge the furnace assembly and protect oxygen contamination during heating and cooling. DTA samples were taken from center of cladding deposit as shown in Figure 3.5, and then machined into a 3.3 mm diameter by 3 mm long cylinder with a 1.65 mm radius on one end to fit into the alumina crucible. Three specimens of each alloy were tested under identical conditions as shown in Table 3.6.

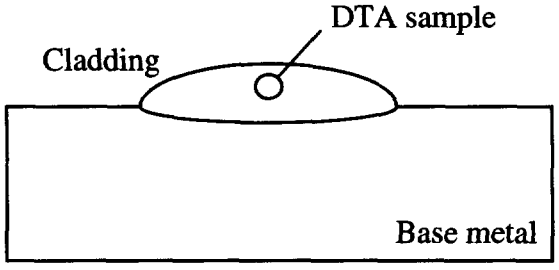

Figure 3.5 Schematic Showing of the DTA Specimen Orientation in Cladding.

Table 3.6 DTA Analysis Parameter for Measuring Clad Metal Solidus and Liquidus	
Heating rate (°C/min.)	30
Holding time (min.)	10
Cooling rate (°C/min.)	30

Weld Metal Solute Segregation

Weld metal solute redistribution (mainly Nb) behavior was studied. The interface quenched cladding samples were used in measuring the partition coefficient (k). The samples were longitudinal sectioned along center line of the bead. To preserve the very thin layer of the water quenched molten metal at edge of the specimen during polishing, a powder hardener was added to the sample mounting material (bakelite). The sample was very lightly etched. The EDS analyses were performed on the interface quenched samples and included (1) bulk composition of the frozen liquid above the dendrites (quenched molten metal), (2) compositions at the solid/liquid interface around the dendrite at the following locations: (a) at the dendrite top adjacent to the quenched frozen liquid, (b) and (c) in between the dendrite top and the dendrite valley, and (d) at the valley of dendrites where the frozen liquid still existed (before secondary phase is

clearly formed) as shown in Figure 3.6, (3) normally solidified clad metal. Microsegregation behavior was measured by SEM/EDS with a windowless detector. The composition of Laves phase and the distribution of the interdendritic eutectic constituents were determined on the as-welded samples.

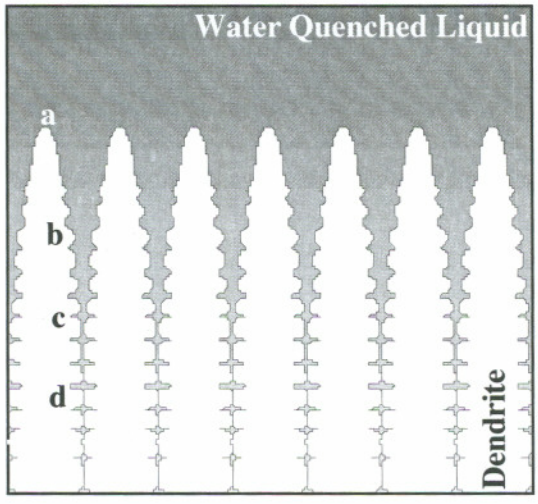

Figure 3.6 Schematic Illustration of the position of SEM/EDS Compositional Analysis in Interface Quenched Cladding Specimen.

Metallography

Metallographic specimens were polished through 0.05 μm alumina, and then etched with HCl-5%H_2O_2 to reveal the general dendritic structure or electrolytic etched (2-3 V) with 10% oxalic acid to identify the eutectic constituents. A special etchant was used for interface study. Due to the difference in chemical composition between cladding material and base metal, two-step etch was used. Polished sample was first etched with 10% oxalic acid then etched with Amy's reagent.

Scanning Electron Microscopy

SEM image analysis was performed for quantitative of percentage of Laves phase. Backscattered mode was used to provide an accurate measurement of the interdendritic constituents. The electron image was captured in a Macintosh Quadra 950 computer linked to the SEM. The quantitative analyses of the interdendritic constituents were performed on the computer using the public domain NIH Image program.

Chemical microanalyses of weld metal segregation and secondary phases chemistry were performed using a Zeiss digital scanning electron microscope (DSM960) equipped with an energy dispersive X-ray spectroscopy (EDS). The accelerating voltage was 25 kV for all EDS analysis. Measurement was made on untilted specimens with an X-ray takeoff angle of 35 degree. K α X-ray lines were used for the analysis of all elements except for Mo and Nb, where L α lines were used.

EXPERIMENTAL VERIFICATION of the MODEL

Verification of the solidification model usually is based on examining individual dendrites where the solute concentration profile is taken and compared with model's prediction. In directionally solidified alloys (or castings), it is easier to obtain such dendrites since they are large in size and uniform in shape. They can be easily sectioned for proper solute concentration measurement. However, in the current work, it is improper to use the above method due to the small dendrite size and large variation in shape and size in the cladding, and more important is that those dendrites at the specimen surface may not be center sectioned. So the experimental verification of the model was conducted by measuring the solute concentration in the liquid (C_L) and the liquid fraction (f_L) at different solidification stages (it is much easier to measure C_L and f_L). Samples

from the interface quenched cladding were used. Composition profile of the solid and fraction of the liquid were measured using SEM. Claddings under different cladding conditions were examined.

Solid/Liquid Fraction Measurement

Samples of the quenched interface cladding were grounded and diamond polished. Very light etch was applied to make the boundary of the frozen interdendritic liquid and solidified solid be clearly identified. Solute concentrations in the interdendritic frozen liquid were measured using SEM/EDS. The fraction of the interdendritic frozen liquid was determined using SEM in the backscatter mode. The frame size and shape of the measured area were controlled based on the niobium concentration level. Within each frame, the niobium concentration variation is smaller than 0.02 wt%. Surfacing deposits under different cladding conditions were examined. The experimental data were compared with the model predictions.

Solute Concentration Measurement

Niobium concentration profile was measured across the sectioned dendrites. Due to the difficulty in getting a perfect center sectioned dendrite, the validation of the model was performed by comparing the fraction of interdendritic liquid at certain niobium concentration with model result. Experimentally, this is much more reliable than measuring solute concentration at different solid fraction level. The solute concentration in the liquid is uniform. The fraction of interdendritic liquid was measured in a small area.

WELD METAL SOLIDIFICATION CRACKING TEST

A new testing method "OGI solidification cracking test" was invented and employed in assessing the solidification cracking susceptibility in strip cladding. The self-restraint weld metal solidification cracking test is shown in Figure 3.7. It used a 25 mm thick base metal plate with a non-symmetric 1.75 mm (0.07") wide gap through the thickness of the substrate over which the cladding was deposited. In this figure, "L" is the total crack length measured across the width of the cladding bead, and "W" is the bead width. A single pass strip cladding was deposited along the center line of 25 mm thick base metal plate. The solidification cracking susceptibility was evaluated by a cracking index CI = L/W. CI = 0 means no cracking and CI =1 means cracking propagated through the whole cladding bead.

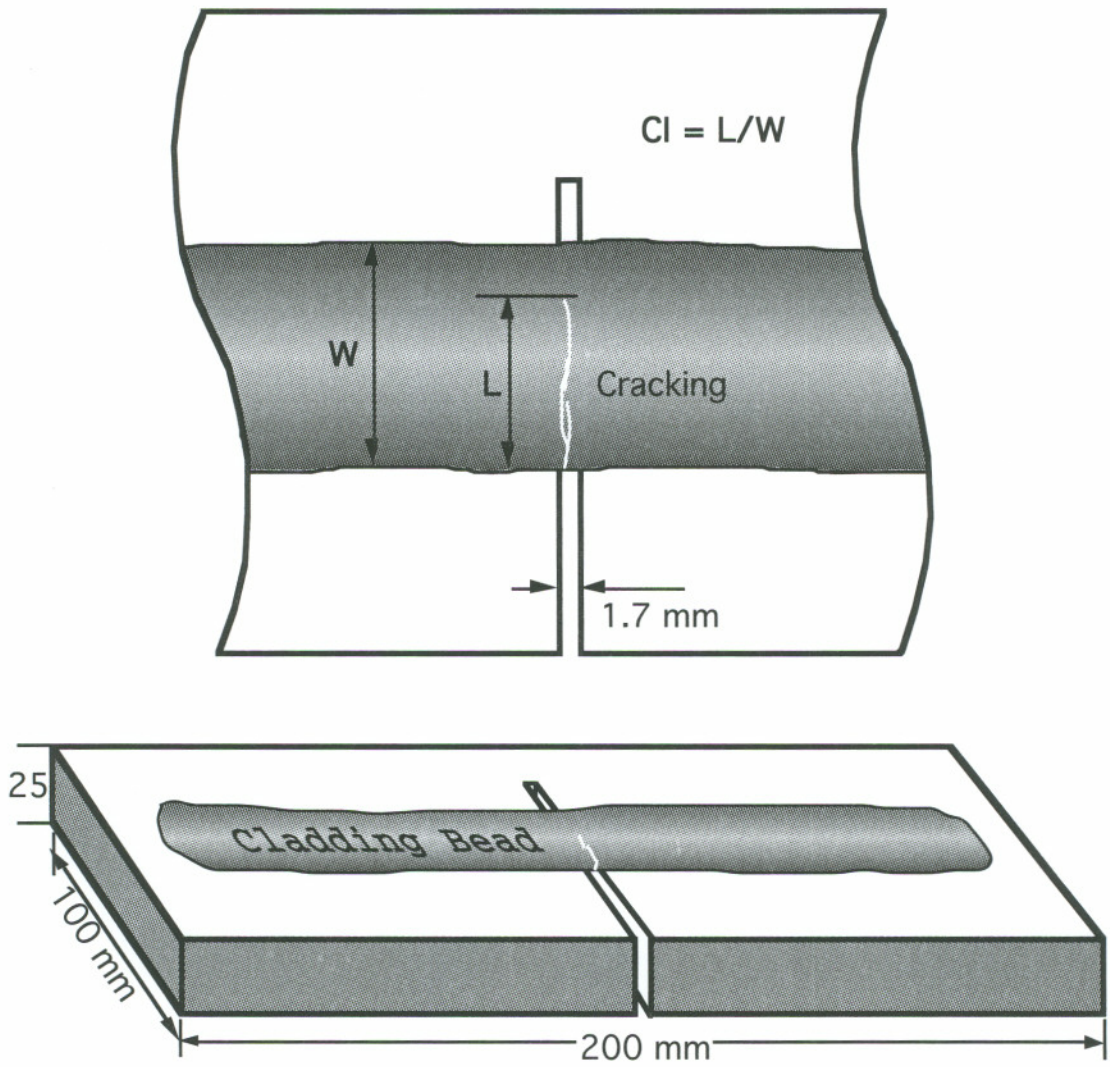

Figure 3.7 OGI Solidification Cracking Test for Strip Cladding.

Cracking Susceptibility of Cladding Materials

In order to establish the trend of material resistant to solidification cracking, the solidification cracking susceptibility of popular used cladding materials was compared. They were nickel alloy 625, nickel alloy 59, 70/30copper-nickel, 70/30nickel-copper, nickel 200, and stainless steel 308L. The test was conducted using the OGI solidification cracking test under identical cladding conditions (600A, 25v, and 152mm/min.) for each cladding strips. Different cladding processes (ESS, SAS) were also investigated for the same cladding material (nickel ally 625).

Effect of Cladding Variables

Effect of cladding variables: The effect of travel speed on solidification cracking susceptibility was investigated. The travel speed was adjusted from 100 to 175 mm/min. (4 to 7 ipm) while maintaining the heat input at 6 kJ/mm (150kJ/in),

The effect of heat input on solidification cracking susceptibility was also investigated. Heat input was adjusted from 6 to 9 kJ/mm (150 to 225 kJ/in)

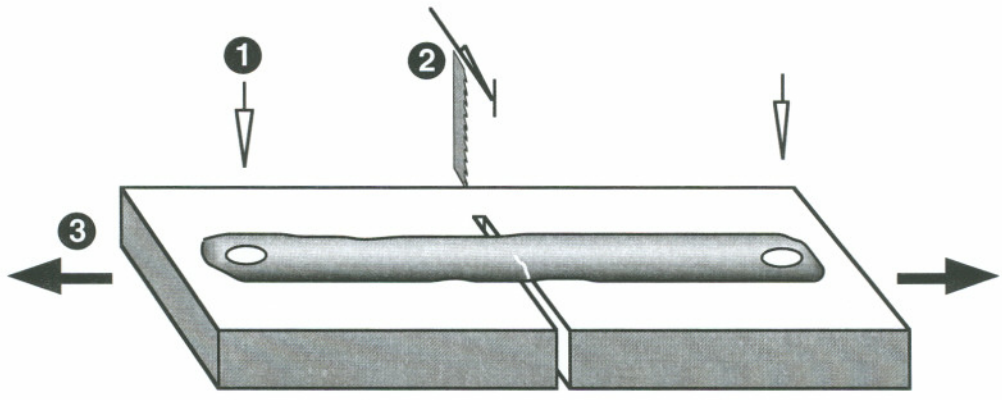

Figure 3.8 Solidification Cracking Test for Strip Cladding. Following the step 1, drilling; 2, cutting; and 3, pulling.

Solidification fracture samples were taken from the cracking test follow by the procedures illustrated in Figure 3.8. Two holes were drilled and the fix end of test piece was saw cut open, then the remaining unfractured cladding deposit was pulled apart. The fractured surfaces were protected while being further section into smaller piece for fractographic analysis. The fractographic analysis of cladding solidification cracking surface was conducted using the Zeiss digital scanning electron microscope (DSM960).

CHAPTER IV

RESULTS and ANALYSIS

ESS PROCESS OPTIMIZATION

Surfacing Variables

To optimize the electroslag surfacing (ESS) process, each independent operating variable had been utilized to its limit and yet kept the process in a stable mode. For example, the cladding voltage was varied from 20 volts, the lowest possible limit of the power source, to 29 volts, beyond which arcing took place and the ESS mode was lost. The cladding current was varied from 500 amps, to maintain the minimum heat input for proper operation, to 900 amps to avoid possible short circuiting. The cladding travel speed was from 102 to 254 mm/min. (4 to 10 ipm). Below 102 mm/min. (4 ipm), a crown shaped cladding bead (wetting angle > 90°) was produced and this could cause slag inclusions between two adjacent cladding beads. Beyond 254 mm/min. (10 ipm) in travel speed, arcing took place.

Cladding sections were metallographically examined and found to be free from defects. The longitudinal section of cladding deposited by ESS showed a uniform penetration pattern along the entire cladding bead except at the starting point where the arc had struck the base metal. The characteristic features of the cladding such as bead dimensions, wetting angle, dilution level, maximum and average penetration, and

deposition rate were evaluated on the cross-section sample by an image analyzer and compared to similar submerged arc surfacing (SAS). Figure 4.1 and Figure 4.2 show the cross section of typical cladding deposited by ESS and by SAS, respectively. This clearly shows that cladding deposited by ESS has uniform penetration and low dilution compared to the cladding deposited by SAS. A typical image analysis of cladding is shown in Figure 4.3, where the surfacing reinforcement portion is identified in red, the penetrated area in white, and the HAZ in green.

The effect of each independent process variable (current, voltage, travel speed) on the dependent process responses (deposition rate, dilution, and penetration) is shown in Figure 4.4 to 4.6. Increasing cladding current (Figure 4.4) increases deposition rate significantly due to the higher strip feeding speed. However, increasing current has little effect on the penetration, as a result, the dilution decreases. The same trend is also observed in SAS. Increasing travel speed while maintaining a constant cladding current and voltage (Figure 4.5) increases deposition rate slightly due to the higher strip feed rate required to maintain the current level. In addition, increasing travel speed increases penetration and therefore the dilution is increased significantly. The cladding voltage has little effect on deposition rate and on penetration, (Figure 4.6) although increasing voltage increases bead width.

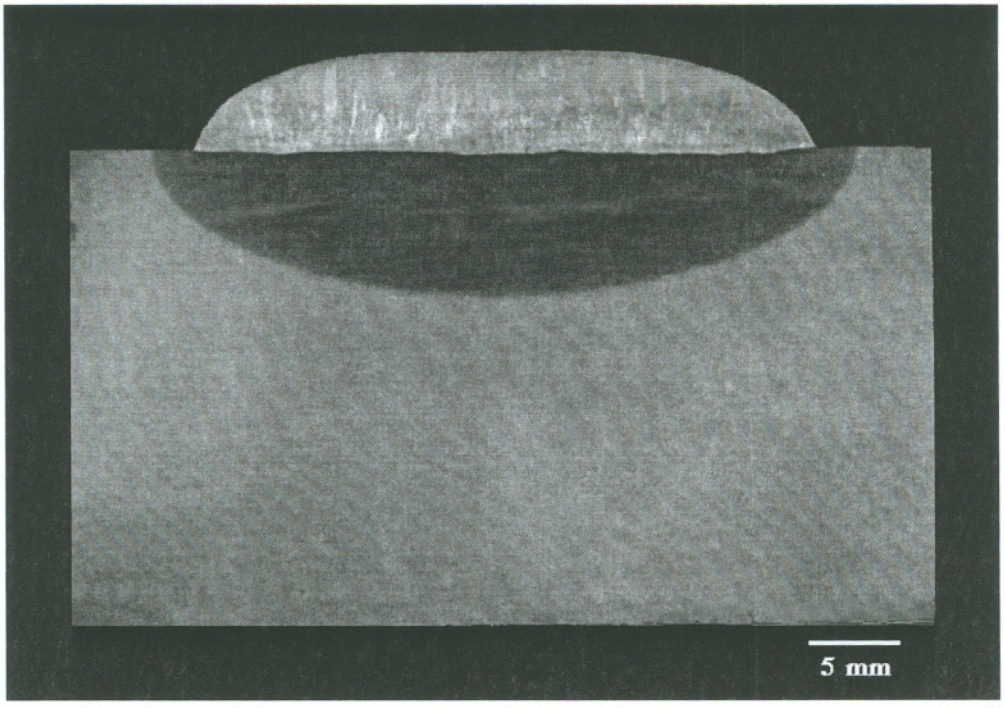

Figure 4.1 The Typical Cross Section of Nickel Alloy 625 Cladding Deposited on MIL-S-23284 Class 1 Steel by ESS.

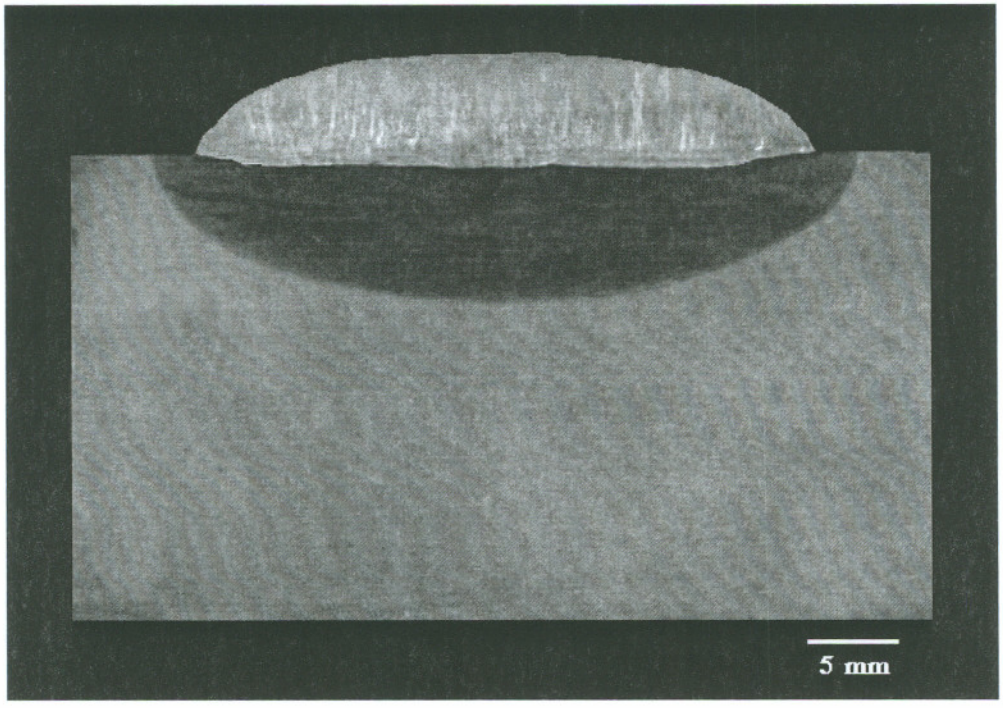

Figure 4.2 The Typical Cross Section of Nickel Alloy 625 Cladding Deposited on MIL-S-23284 Class 1 Steel by SAS.

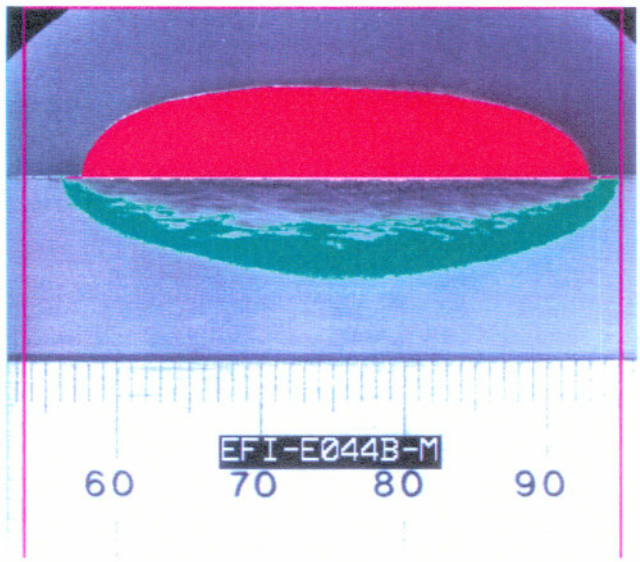

(a)

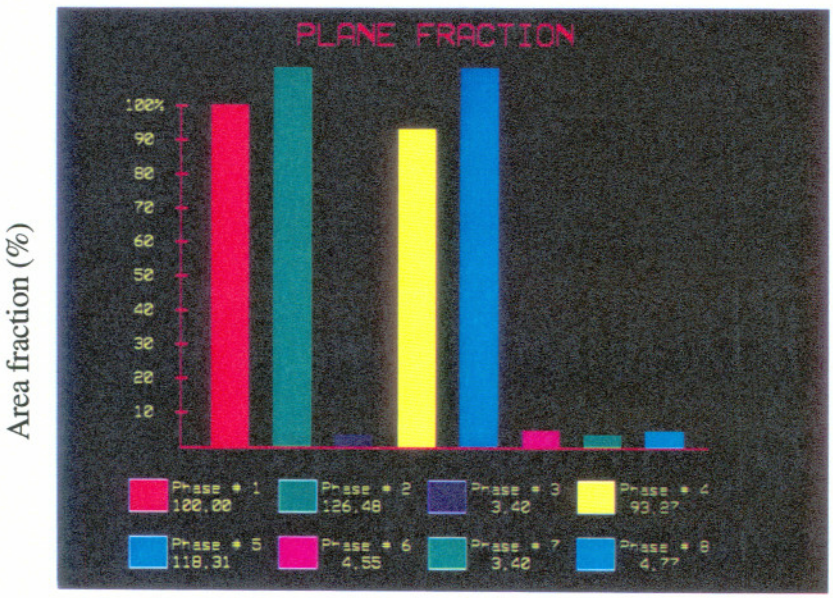

(b)

Figure 4.3 Image Analysis of the Nickel Alloy 625 Cladding Deposited on MIL-S-23284 Class 1 Steel by ESS, (a) Feature Identification of Cladding Cross Section and (b) Result of the Image Analysis (Area Fraction).

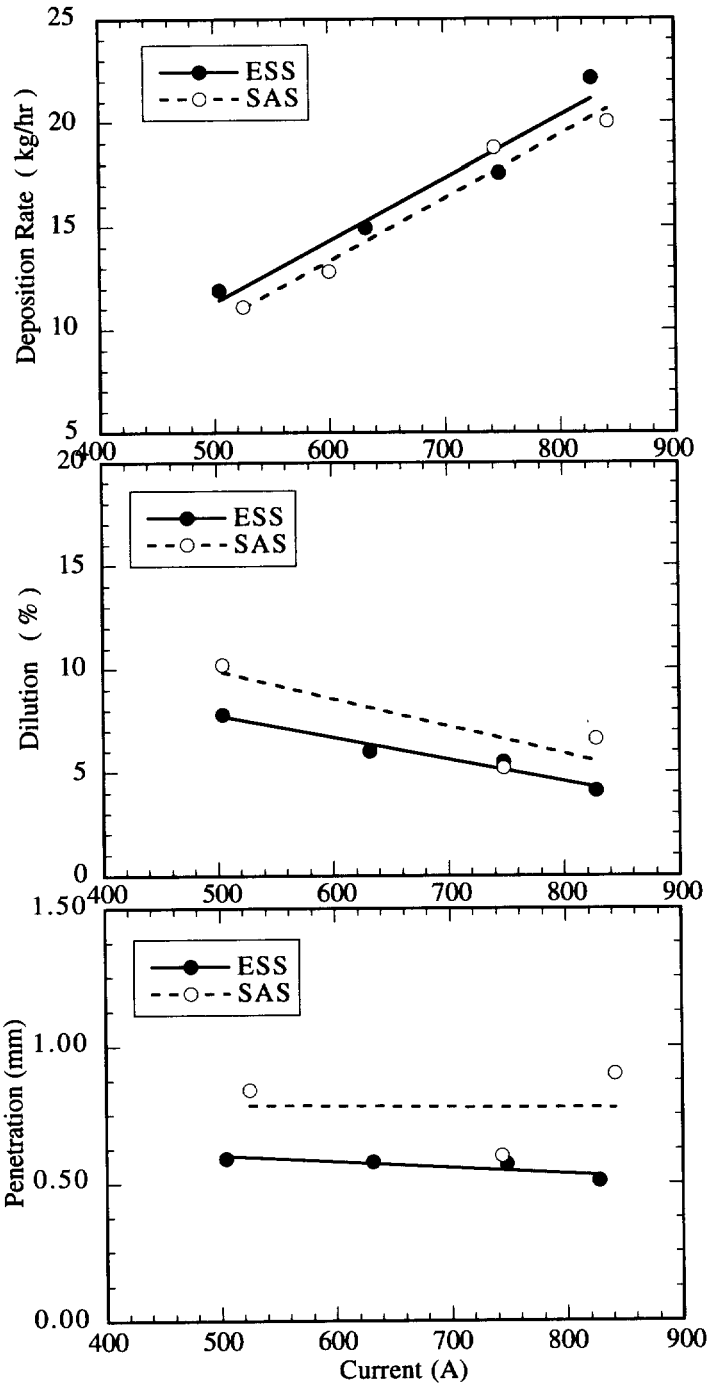

Figure 4.4 The Effect of Current on the Deposition Rate, Dilution, and Penetration of Nickel Alloy 625 Surfacing Deposited on MIL-S-23284 Class 1 Steel (voltage and travel speed are maintained at 25v and 152 mm/min., respectively).

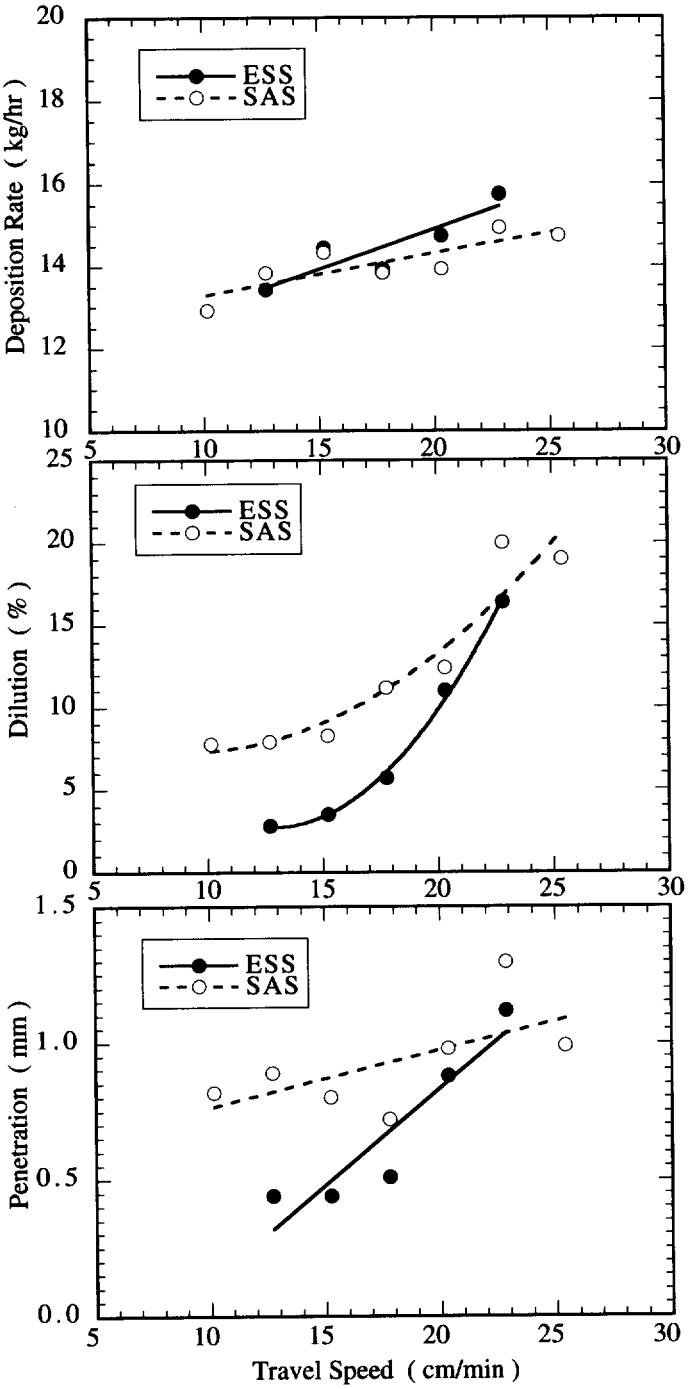

Figure 4.5 The Effect of Travel Speed on the Deposition Rate, Dilution, and Penetration of Nickel Alloy 625 Surfacing Deposited on MIL-S-23284 Class 1 Steel (current and voltage are maintained at 600A and 25v, respectively).

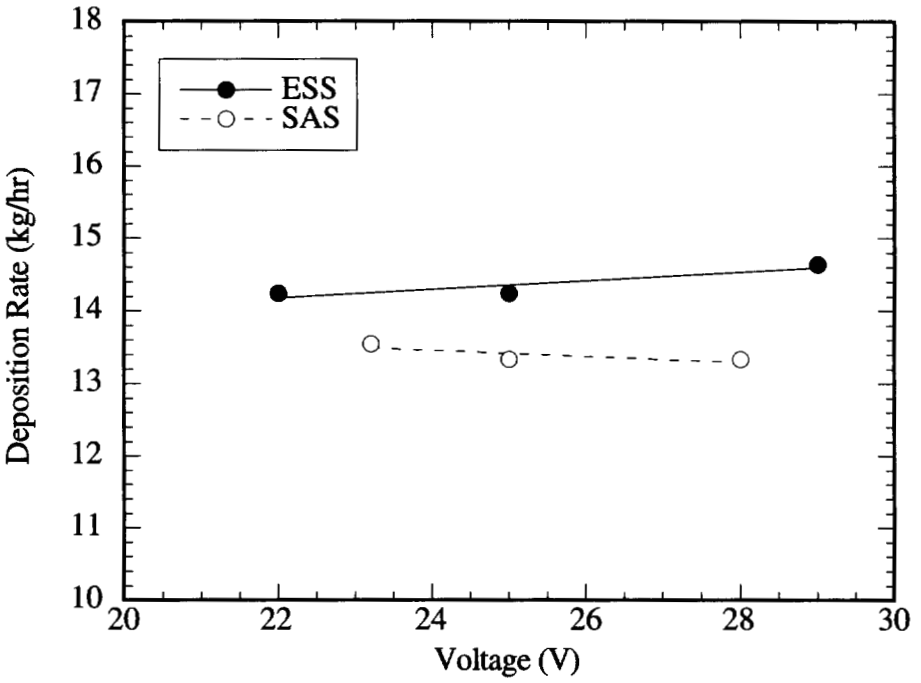

Figure 4.6 The Effect of Voltage on the Deposition Rate of Nickel Alloy 625 Surfacing Deposited on MIL-S-23284 Class 1 Steel (current and travel speed are maintained at 600A and 152 mm/min., respectively).

The optimal ESS conditions produced (1) acceptable dilution level of approximately 7%, (2) a sound bead shape, and (3) maximal possible deposition rate. The dilution level for the surfacing, as specified in MIL-STD-2191, required the iron content in the cladding ≤ 9 wt% and the molybdenum content in the cladding ≥ 8 wt%, both of which were considered at safe levels without deteriorating the corrosion resistance of nickel alloy 625 in sea water.[27,31,32,34] The bead shape was evaluated by wetting angle and bead height. Possible slag entrapment (slag inclusion) was avoided completely by controlling the wetting angle to less than 70°. The final optimal electroslag surfacing variables are listed in Table 4.1 for the 30 x 0.5 mm nickel alloy 625 strip deposited on MIL-S-23284, class 1 shafting steel. The typical characteristics of surfacing deposit under optimal surfacing conditions are listed in Table 4.2.

Table 4.1 Optimized ESS Variables for 30 x 0.5 mm Nickel Alloy 625 Strip Electrode Deposit on MIL-S-23284, Class 1 Shafting Steel

Current (A)	650
Voltage (V)	27
Travel Speed (mm/min.)	175
Lateral Overlap (mm)	3.5

Table 4.2 Typical Characteristics of ESS and SAS Deposits using 30 x 0.5 mm Nickel Alloy 625 Strip Electrode on MIL-S-23284, Class 1 Shafting Steel under the Condition Listed in Table 4.1

	ESS	SAS
Dilution (%)	6.5	11.7
Deposition rate (kg/hr)	15.7	13.6
Average penetration (mm)	0.33	0.66
Maximum penetration (mm)	0.61	1.09
Bead height (mm)	5.7	5.2
Bead width (mm)	37.0	37.4
Wetting angle	57°	50°

A wider, lower, and smoother bead profile was found in the second layer cladding in comparison with the first layer. Deeper penetration which caused higher dilution was also observed in the second through fourth layers of cladding. The deeper penetration and wider bead profile in the second layer are due to the low thermal conductivity of the first layer (compared to the steel base metal) and better wetting conditions. The more rapid thermal flow in the first layer is caused by the high thermal conductivity of the base steel. When depositing a second layer, the heat is conducted through the first layer in which a build-up of heat is observed as the result of the lower thermal conductivity. The second layer beads tend to be wider because of a better lateral flow-out. The dilution levels of the second layer measured by an image analyzer were 16% and 33% for ESS and SAS, respectively. Increasing cladding current increased the bead height to the same level as the first layer without producing a steep edge. However, for consistency, the same cladding variables for the first layer were still used for the following layer.

Composition Profiles

The surfacing deposit chemical compositions of different layers of nickel alloy 625 deposited on MIL-S-23284 class 1 steel measured by spark emission spectroscopy are listed in Table 4.3 for the ESS process and Table 4.4 for the SAS process. The dilution level could also be calculated from the chemical composition of the surfacing deposit using Eq. [4.1]. According to this equation, based on iron composition, the first layer dilution of nickel alloy 625 deposited on class 1 steel were 6.0% and 8.8% for ESS and SAS, respectively. Comparing to the dilution measured by the image analyzer (6.5% and 11.7% for ESS and SAS), the calculated dilution based on iron composition is lower

than that measured by the image analyzer especially when the iron content in the strip electrode is high. The difference between physically measured dilution and chemically calculated dilution is because the strip electrode contains iron and the base metal is not pure iron. The dilution obtained physically from the image analyzer should be considered as the most accurate measurement, because it represents the actual geometry of surfacing deposit.

$$Dilution\ \% = \frac{Deposit\ Fe\% - Strip\ Fe\%}{Steel\ Fe\% - Strip\ Fe\%} x100\% \qquad [4.1]$$

The alloying vectors of ESS and SAS for each element in this alloy were calculated based on the fourth layer compositions as listed in Table 4.5. Metal-slag reactions and reaction condition (arc & non-arc) for the two flux system were completely different. The cladding deposited by the SAS process exhibited a significant silicon pickup and chromium reduction due to high content of silicon in the SAS flux and high reaction temperature due to the welding arc. In contrast, ESS flux contains less silicon and the metal-slag reacts at lower temperature (slag temperature approx. 2300°C[20]) and no arc is involved in ESS except at the start.

Table 4.3 Chemical Compositions of Four Layer Cladding of Nickel Alloy 625 Deposited on MIL-S-23284 Class 1 Steel by ESS

Element wt%	First layer	Second layer	Third layer	Fourth layer
C	0.012	0.008	0.007	0.006
Mn	0.04	0.00	0.00	0.01
Fe	6.54	0.24	0.00	0.00
S	0.004	0.003	0.003	0.004
Si	0.16	0.08	0.07	0.08
Ni	60.80	66.30	66.49	66.25
Cr	20.82	21.66	21.64	21.64
Al	0.04	0.03	0.04	0.04
Ti	0.001	0.001	0.001	0.001
Mo	8.71	8.64	8.66	8.75
Nb	2.84	3.01	3.06	3.17
P	0.001	0.00	0.00	0.00

Table 4.4 Chemical Compositions of Four Layer Claddings of Nickel Alloy 625 by SAS

Element wt%	First layer	Second layer	Third layer	Fourth layer
C	0.05	0.02	0.02	0.02
Mn	0.12	0.04	0.04	0.03
Fe	9.20	3.54	1.70	1.37
S	0.006	0.004	0.005	0.004
Si	0.69	0.67	0.69	0.67
Ni	56.41	61.75	63.19	63.62
Cr	20.60	21.03	21.26	21.29
Al	0.11	0.10	0.11	0.10
Ti	0.061	0.048	0.055	0.062
Mo	9.30	9.15	9.26	9.09
Nb	2.82	2.98	3.01	3.06
P	0.001	0.00	0.00	0.00

Table 4.5 Alloying Vectors for ESS and SAS Process

	C	Mn	Fe	S	Si	Cr	Al	Ti	Mo	Nb	P
ESS	-0.02	-0.02	-0.95	+0.03	+0.04	-0.86	-0.22	-0.19	-0.57	-0.30	-0.005
SAS	-0.01	0.001	0.42	.003	+0.63	-1.21	-0.16	-0.13	-0.33	-0.41	-0.005

WELD METAL SOLIDIFICATION

Weld Pool & Weld Metal Solid/Liquid Interface

The size of the weld pool in ESS using 30 mm wide strip electrodes was very large compared with conventional wire welding. For typical cladding, the molten slag pool was measured from 76 mm to 100 mm (3 to 4") long and the molten metal pool 54 mm (2.1") long. The shape of the weld pool for electroslag surfacing was revealed from the quenched interface samples as shown in Figure 4.7. The solid/liquid interface of the weld pool is illustrated in Figure 4.8. Of the 54 mm (2.1") long weld pool, at least one third of it was a flat region in the front portion near the electrode of the interface as shown in Figure 4.8. Therefore, the direction of maximum thermal gradients at the early stage of the solidification is perpendicular to the base metal or vertical. Unlike the double ellipsoid heat source in conventional welding, the vertical thermal gradient will produce grain and dendritic structure that are virtually unidirectional and vertical as illustrated in Figure 4.9, 4.10, 4.13 - 4.17, and 4.20.

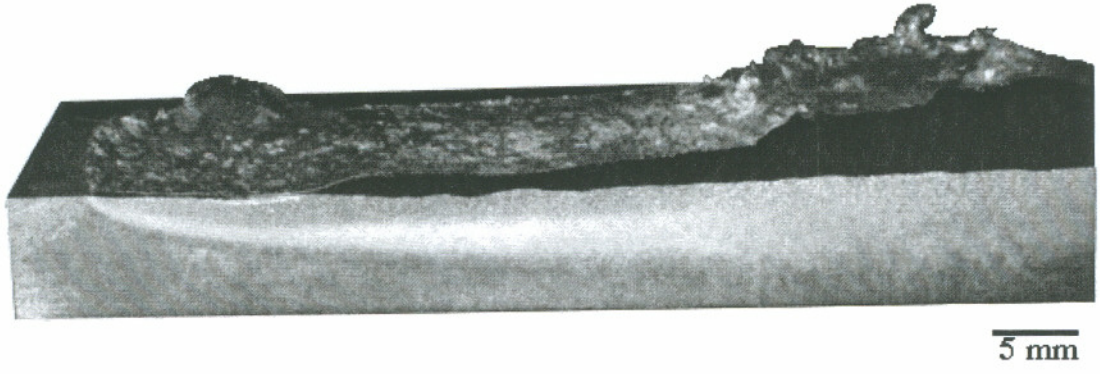

Figure 4.7 Water Quenched Weld Metal Solid/Liquid Interface of Nickel Alloy 625 Electroslag Surfacing.

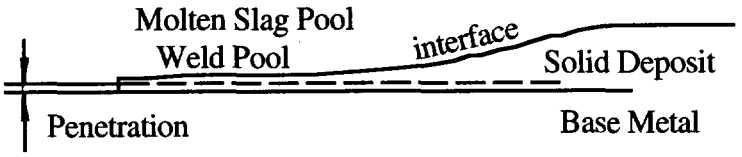

Figure 4.8 Illustration of the Weld Metal Solid/Liquid Interface of Nickel Alloy 625 Electroslag Surfacing.

Solidification Parameters

Because most grains in the clad metal were straight and grew perpendicularly to the substrate, the average solidification time at the center of the cladding could be roughly estimated by Eq. [4.2]. For typical cladding, the center pool length was about 53 mm (2.1") and the travel speed was 152 mm/min. (6 ipm), resulting in an average freezing time about 21 seconds for the cladding.

$$Solidification\ Time\ (sec) = \frac{60\ \text{x}\ Pool\ Length\ (mm)}{Travel\ Speed\ (mm/min.)} \qquad [4.2]$$

Freezing range of nickel alloy 625 cladding

The solidus and liquidus of the first layer cladding of nickel alloy 625 deposited on MIL-S-23284, class 1 steel were measured by DTA as shown in Table 4.6 The surface deposit of ESS exhibited a narrower melting range and higher melting temperature than that of the SAS surface deposit. The wider melting range and lower melting temperature of the SAS surface deposit were attributed mainly by its high silicon content which nearly quadrupled the amount of silicon content in the ESS deposit. Silicon was identified as Laves phase promoter in nickel alloy 625[91] which widened the

melting range of the alloy system by depressing the melting point of interdendritic constituents.

Table 4.6 Solidus and Liquidus of Nickel Alloy 625 Cladding Deposit			
Weld deposit	Solidus °C	Liquidus °C	ΔT °C
ESS	1284.4	1359.5	75.1
SAS	1270.2	1350.9	80.7

Solidification cooling rate

The local solidification time of gas tungsten arc (GTA) remelting of nickel alloy 625 cladding deposited by ESS (measured by plunging a thermocouple into the molten weld pool) was 2.4 seconds. The melting range of nickel alloy 625 was from 1359.5°C to 1284.4°C (75.1°C), so the average cooling rate was 31 °C/sec. The average primary dendrite arm spacings (λ) of GTA remelted nickel alloy 625 ESS deposited near the plunged thermocouple was 36.6μm as shown in Figure 4.9. The dendrite arm spacings versus the cooling rate of the GTA remelted metal is plotted in Figure 4.11. It is in agreement with Heubner's correlation[98] (Eq. 2.1). So that Heubner's correlation established in directionally solidified castings of nickel alloy 625 is confirmed to be true in welding situations, $\lambda = 758.3 \bullet (\text{Cooling rate})^{-0.4}$. For ESS, the measured primary dendrite arm spacing at the center of the cladding deposited by ESS was 88.5 μm (on average) as shown in Figure 4.10. By using such a correlation, the estimated cooling rate for ESS was about 3.6°C/s, that corresponded to 21 seconds cooling time. This result coincidentally agreed with the estimation predicted by Eq. 4.2 which was based on weld pool geometry and surfacing travel speed. For high heat input cladding by ESS, the

primary dendrite arm spacing was 120μm (on average) which corresponded to a 1.7 °C/s cooling rate.

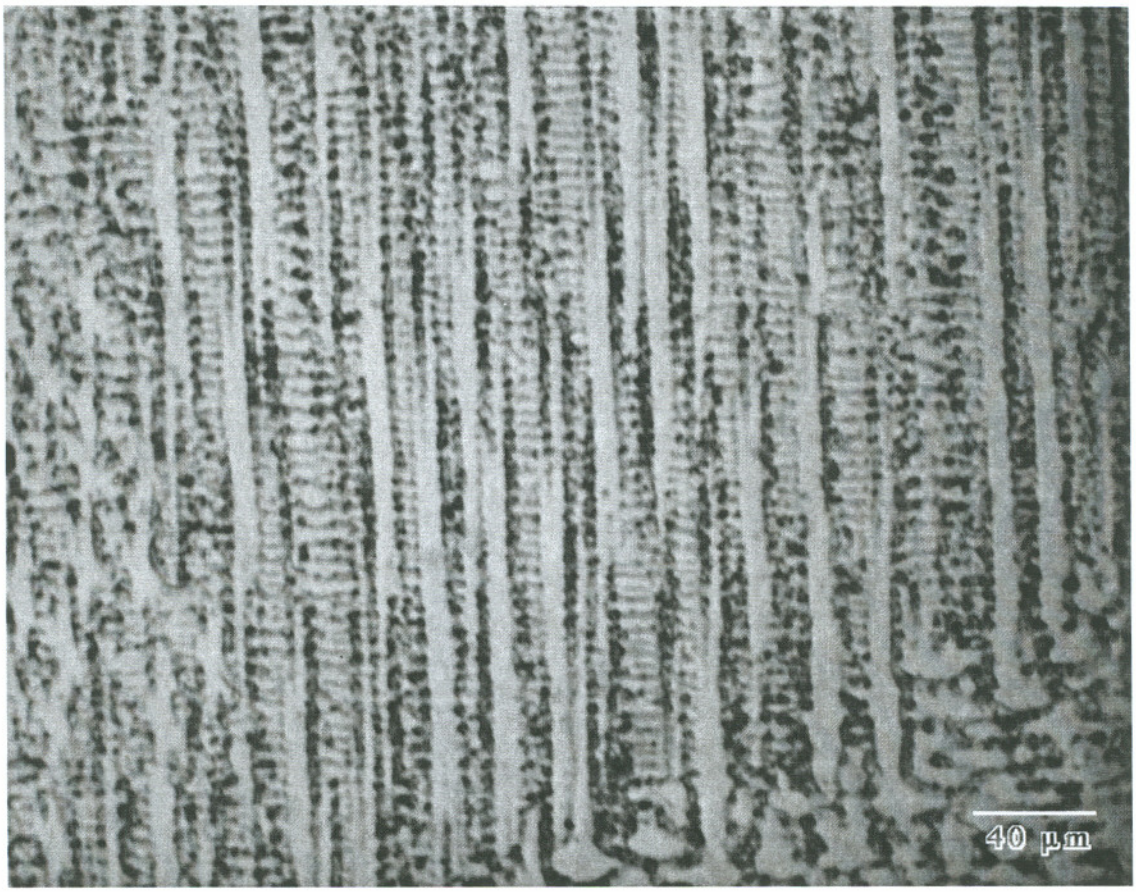

Figure 4.9 Dendritic Structure of GTA Remelted Nickel Alloy 625 ESS Deposit.

Figure 4.10 Dendritic Structure of Nickel Alloy 625 Cladding Deposited on MIL-S-23284 Class 1 Steel by ESS.

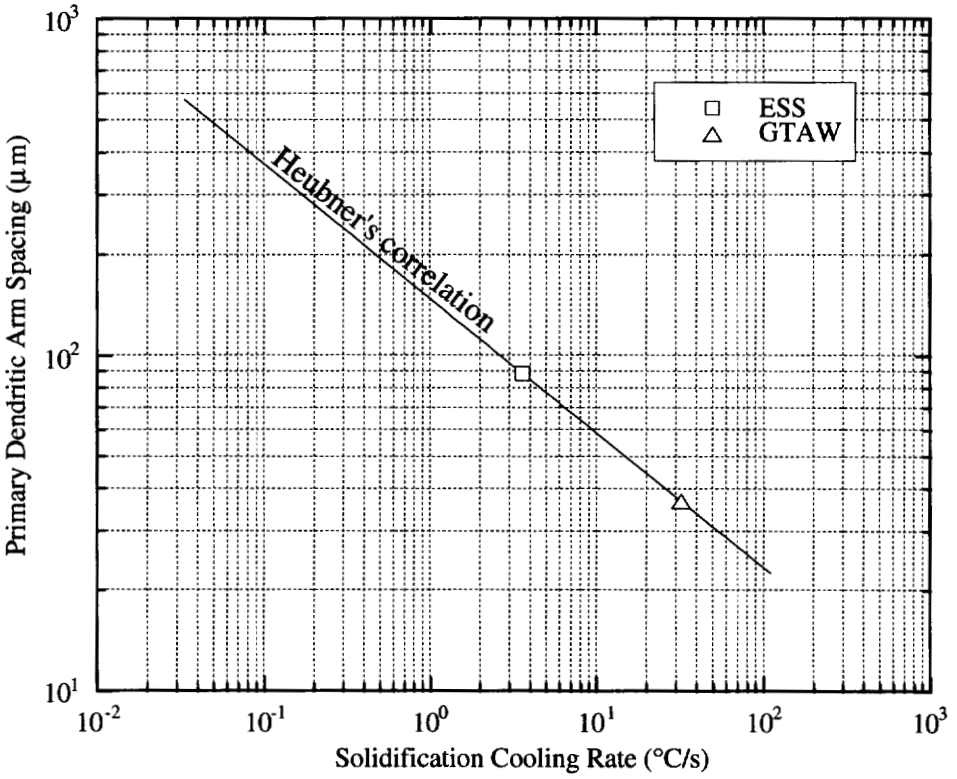

Figure 4.11 Cooling Rate in Nickel Alloy 625 Composite Zone of ESS and GTAW Calculated from Heubner's Correlation, Reference (98).

The solidification parameter of the stainless steel unmixed zone was also determined by a similar manner using the widely accepted Grant's relationship, $\lambda_2=7.6\bullet(Cooling\ rate)^{-0.19}$. The secondary dendritic arm spacing averaged about 2 μm which implied a cooling rate at this region about $1.3x10^3$ °C/sec according to the Grant relationship as shown in Figure 4.12.[44,129,186]

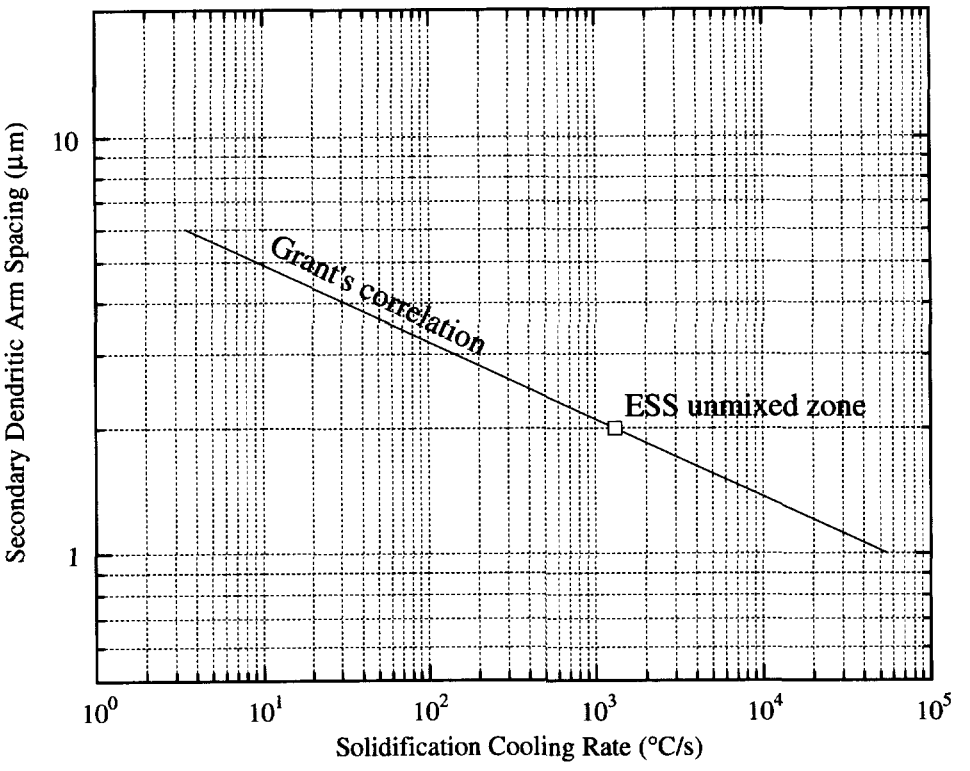

Figure 4.12 Cooling Rate Determination of the Unmixed Zone in Nickel Alloy 625 Deposited on 316 Stainless Steel Based on Grant's Correlation, Reference (186).

Solidification & Segregation

Solid/liquid interface in cladding

The microstructure of the solid/liquid interface of nickel alloy 625 cladding was revealed by water quenching during ESS as shown in Figure 4.13. This figure showed that most of the liquid metal was removed by the water jet, and only a thin layer of liquid weld metal remained and rapidly froze on top of the normal welding solidification structure (dendrites). Both bulk composition of the frozen liquid (quenched liquid weld metal) and bulk composition of the completely solidified solid (naturally solidified dendrites) were measured by SEM/EDS and are listed in Table 4.7. The composition of the liquid and solid were basically identical. As weld metal solidification proceeded, strongly convected liquid weld metal was continuously supplied to the top of the dendrites while the dendrites grew. No solute was built up and no segregation took place in the dendrite growth direction, i.e. there was no evidence of normal segregation or macrosegregation. The dendrite always grew into a liquid which had the same bulk composition vertically as the solid; as a result, no solute bands were formed in cladding. The segregation only took place laterally as dendrites coarsened.

Table 4.7 SEM/EDS Analysis of Water-Quenched Cladding of Nickel Alloy 625 Deposited on MIL-S-23284 Class 1 Steel by ESS

Element wt%	Quenched Liquid Weld Metal (bulk)	Naturally Solidified Dendrites (bulk)
Mn	0.12	0.15
Fe	7.61	7.77
Si	0.23	0.20
Ni	57.89	56.98
Cr	20.21	20.0
Mo	8.46	8.45
Nb	2.80	2.82

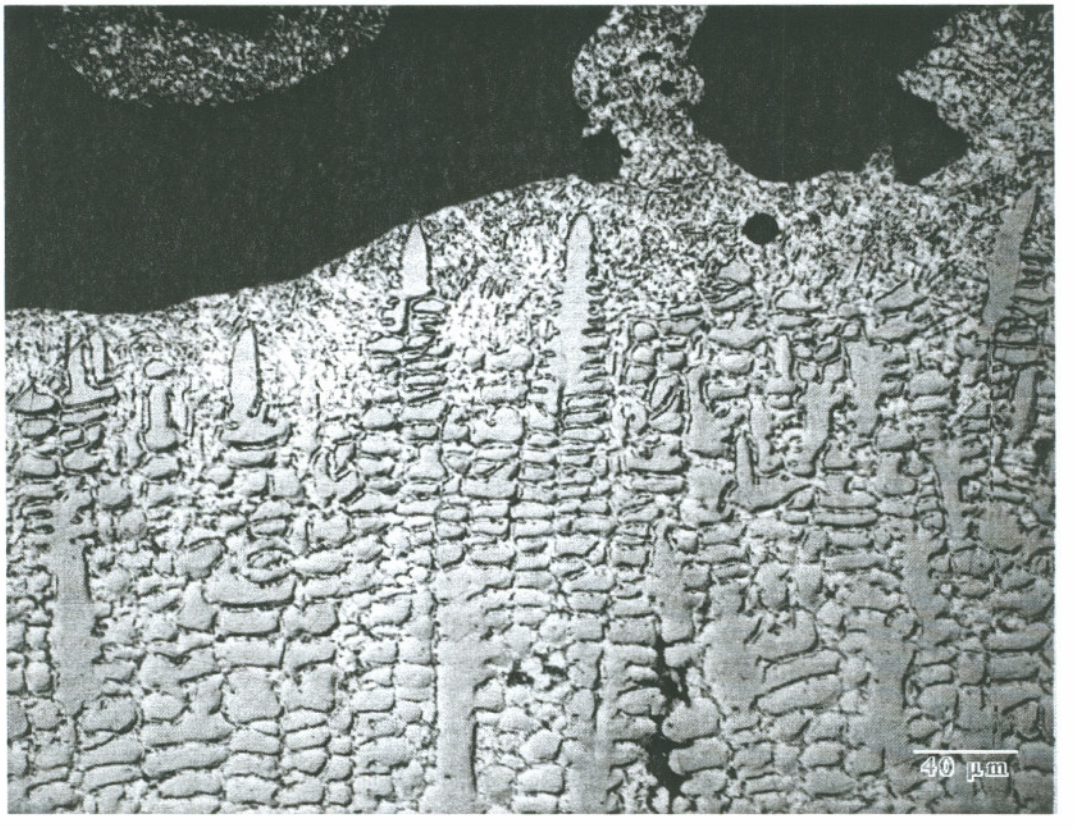

Figure 4.13 Optical Micrograph of the Water-Quenched Cladding Sample of Nickel Alloy 625 Deposited on MIL-S-2384 Class 1 Steel, electrolytic etched with 10% oxalic acid.

Under the optical microscope, the interdendritic region containing high niobium appeared to be darker than the dendrites (Figure 4.14). In the SEM image, the interdendritic region was brighter because of the greater number of secondary electrons emitted from regions which had high-atomic-number elements. The backscattered image from an unetched specimen showed the niobium and molybdenum-rich interdendritic regions were brighter as shown in Figure 4.15.

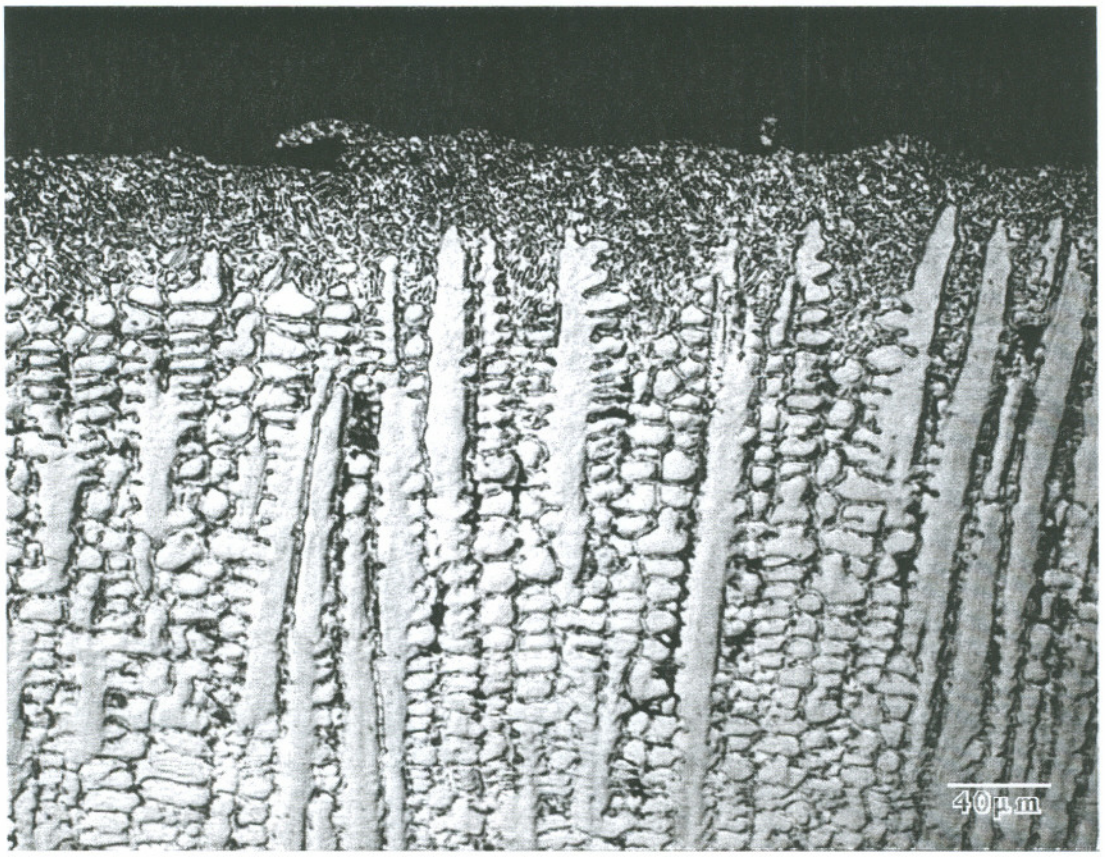

Figure 4.14 Optical Micrograph of Nickel Alloy 625 Cladding Deposited on Class 1 Steel. Water Quenched Sample, Dendrites Core Appear Brighter than Interdendritic Area, at the Top is the Water Quenched Liquid Weld Metal.

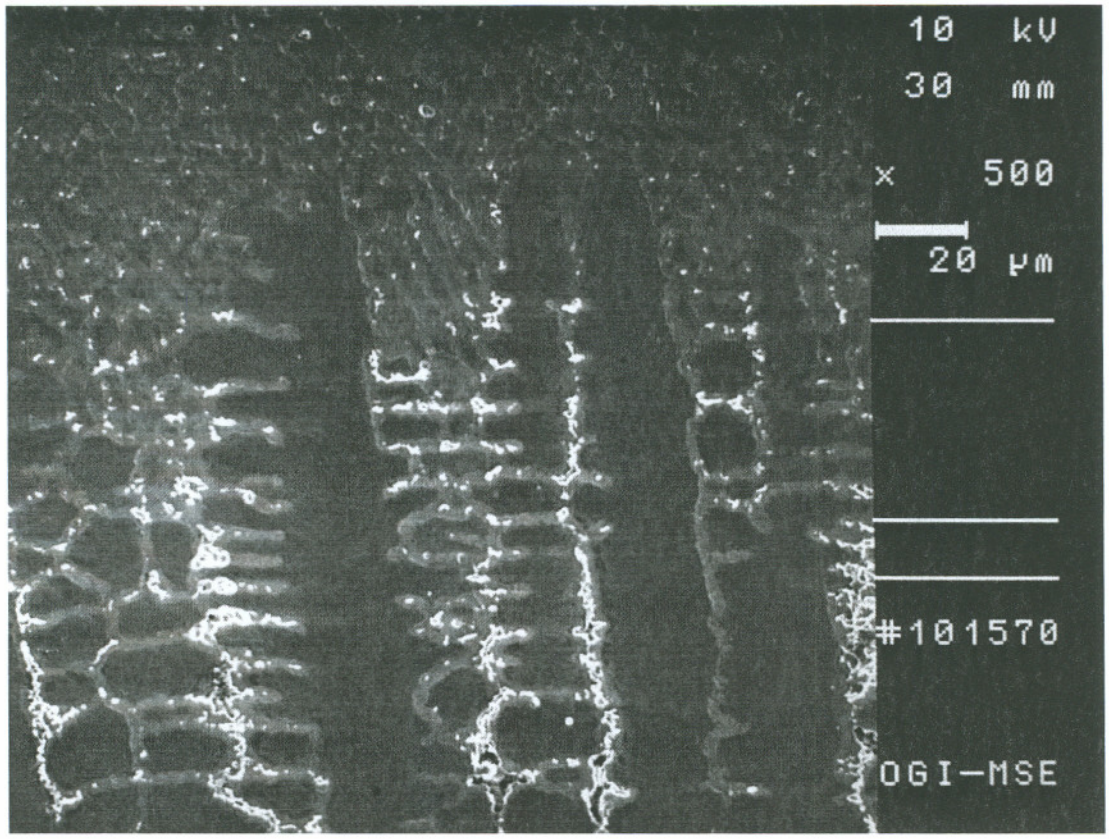

Figure 4.15 Scanning Electron Backscattered Image of Nickel Alloy 625 Cladding Deposited on Class 1 Steel. Water Quenched Sample, in Contrast to the Optical Micrograph, Interdendritic Area Appear Brighter than Dendrites Core.

Figure 4.16 is a SEM micrograph of the water-quenched samples where the majority of the weld metal is solidified. The interdendritic liquid appears in Figure 4.16 as a white network. It clearly indicates that dendrites were completely surrounded by the niobium-rich interdendritic liquid and the liquid film was in a continuous network-form. The continuous liquid film existed even when the dendrites were nearly completely formed. At this stage, no interdendritic precipitates were formed.

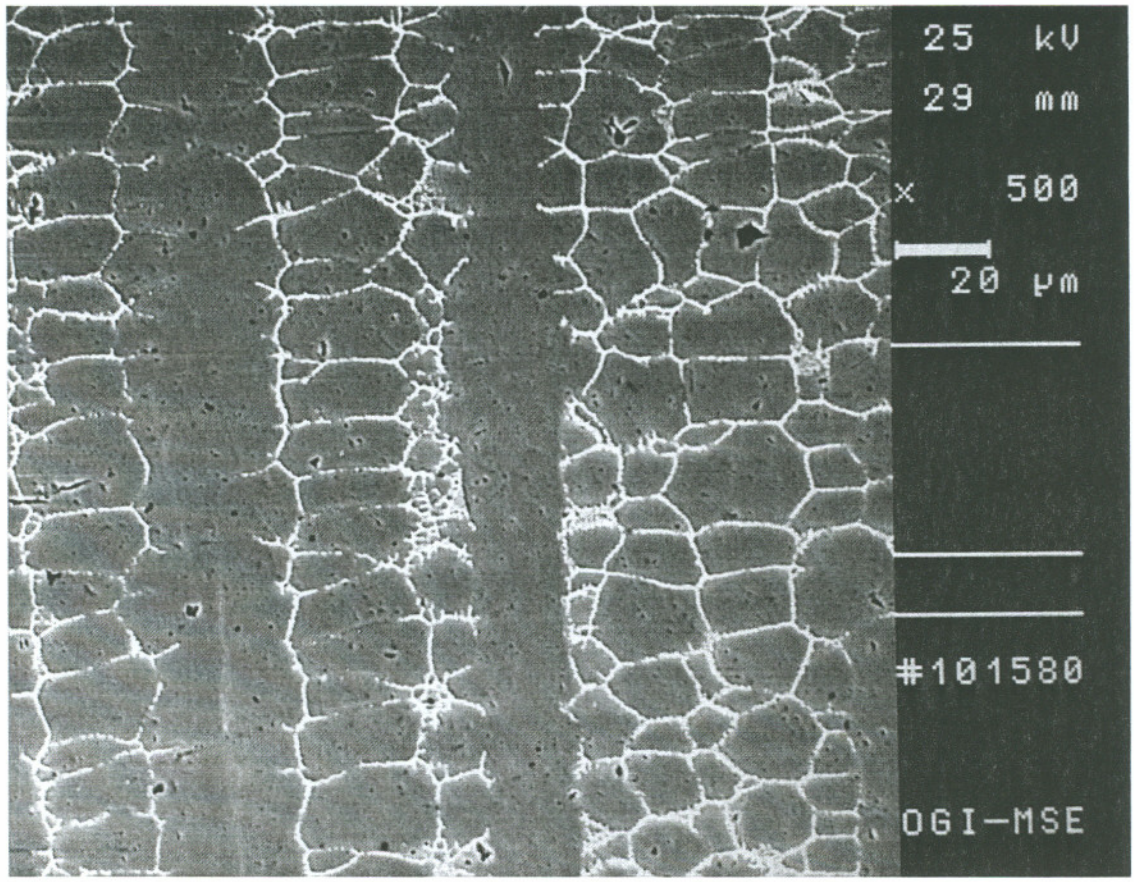

Figure 4.16 SEM Micrograph of Niobium-rich Liquid Network in the Water-Quenched Nickel Alloy 625 Cladding Deposited on MIL-S-23284 Class 1 Steel by ESS.

Interdendritic precipitates

The as-welded nickel alloy 625 microstructure consisted of γ matrix and Laves phase and carbides in the interdendritic regions as a result of the non-equilibrium solidification. These interdendritic precipitates were discontinuous within the interdendritic regions as shown in Figure 4.17. Detailed SEM images of the Laves phase and MC carbides at higher magnification are shown in Figure 4.18 and Figure 4.19. The interdendritic precipitates (Laves phase and carbides) can be distinguished by their morphology. Laves phase showed a lamellar script shape as shown in Figure 4.18, and carbides exhibited a blocky shape as shown in Figure 4.19. The compositions of Laves phase and MC carbides are listed in Table 4.8.

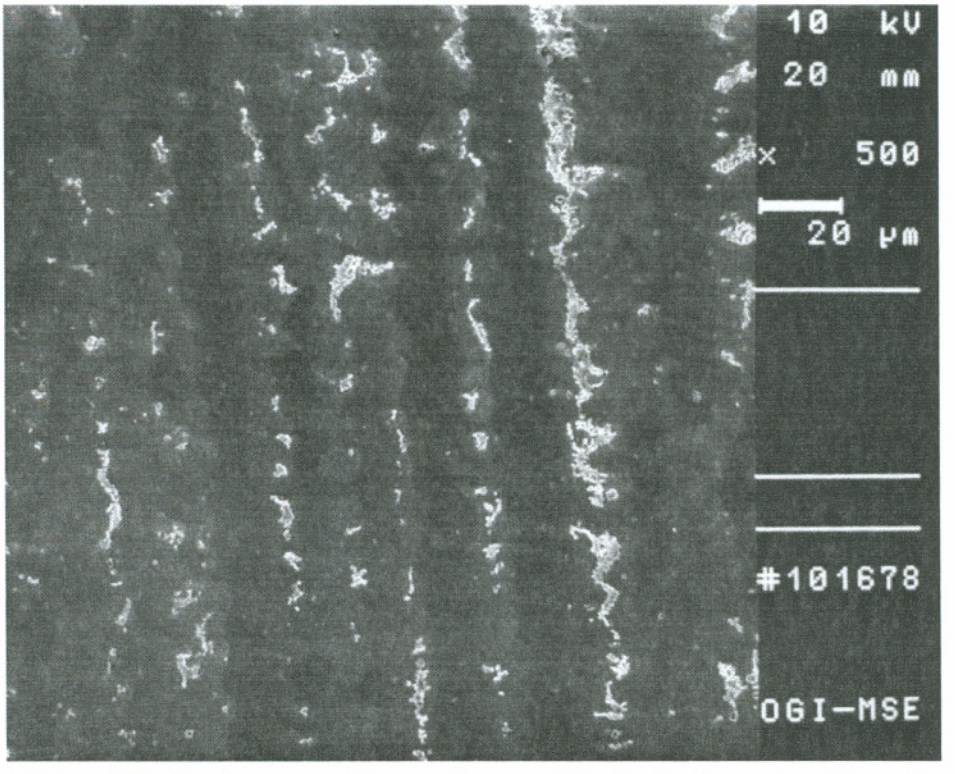

Figure 4.17 SEM Backscattered Image Shows γ Matrix (dark area) and Interdendritic Precipitates (bright area) for Nickel Alloy 625 Cladding Deposited on Class 1 Steel by ESS.

Figure 4.18 Scanning Electron Microscopy Showing Laves Phase in Nickel Alloy 625 Cladding Deposited on Class 1 Steel by ESS.

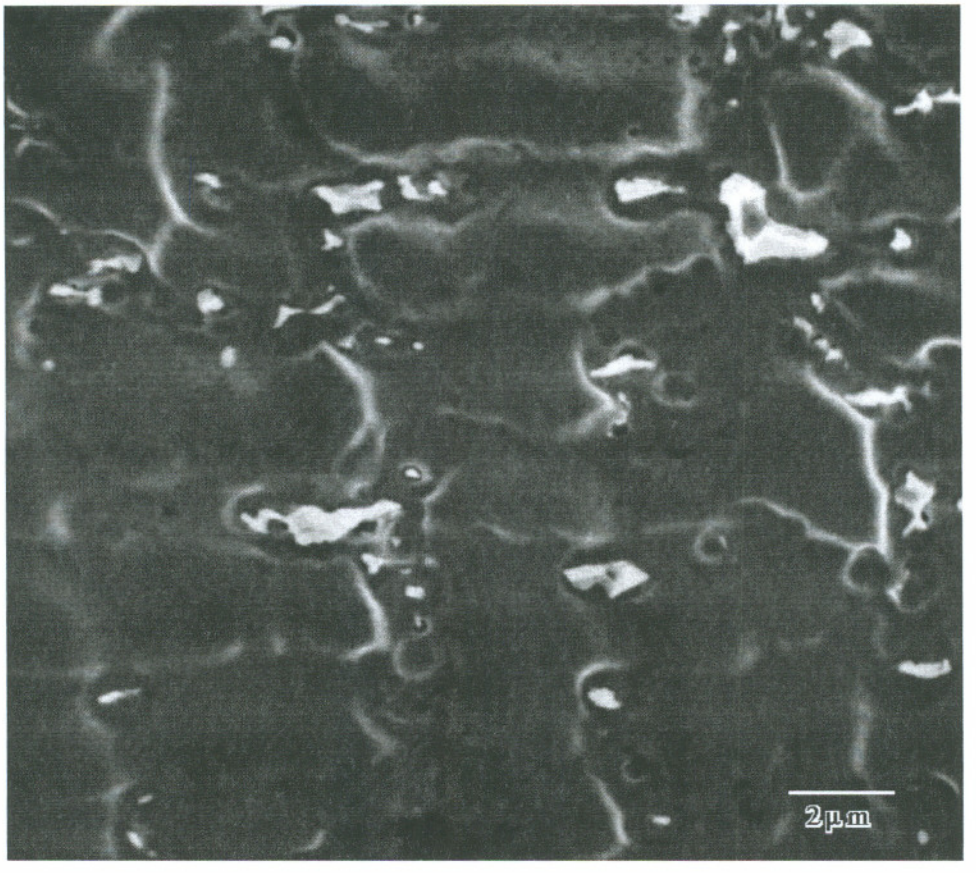

Figure 4.19 Scanning Electron Microscopy Showing Carbides in Nickel Alloy 625 Cladding Deposited by ESS.

Table 4.8 EDS Analysis of Laves Phase and Carbide in Nickel Alloy 625 Cladding by ESS

	Ni	Fe	Cr	Si	Mo	Nb	Ti
Laves	43.8	7.1	14.5	1.0	18.1	15.4	0.1
Laves	39.8	6.3	17.6	1.3	19.8	15.2	0.0
Laves	41.2	5.9	15.9	1.6	17.4	17.9	0.1
Laves	37.4	6.1	20.6	1.6	19.8	14.4	0.1
Laves	40.9	7.8	14.5	2.1	18.2	16.5	0.0
Laves	36.1	7.6	14.6	2.1	23.1	16.4	0.1
MC	4.7	1.0	2.3	0.3	34.3	55.2	2.2

The average niobium content of the Laves phase was 16 wt%. This result is in agreement with other research work found in references (91,97,187) and it also fits in the general formula form $(Ni,Fe,Cr,Mn,Si)_2(Mo,Ti,Nb)$ for the Laves phase in nickel alloy 625.

Variable partition coefficient

The niobium concentrations in the solid and the liquid at the interface measured by SEM/EDS on the water-quenched samples are listed in Table 4.9. The positions (a, b, c, d) were from dendrite top (tip) to the bottom, corresponding locations (a, b, c, d) of measurement in the dendritic structure are shown in Figure 4.20. The local temperature decreased from dendrite tip (a) to valley (d). However, in the current experiment the exact temperature of the measured point could not be determined. The partition coefficients (k) was determined based on niobium interfacial concentration, the result is also listed in Table 4.9.

Table 4.9 Niobium Redistribution in Nickel Alloy 625 Deposited on Class 1 Shafting Steel by ESS. Data is from the Water-Quenched Samples

Location	Interdendritic liquid, C_L^*	Solid dendrite core, C_S^*	Partition coefficient, $k=C_S^*/C_L^*$
Dendrite tip (a)	2.63	0.93	0.35
⇓ (b)	3.03	1.03	0.34
⇓ (c)	4.97	1.49	0.30
Dendrite root (d)	7.29	1.97	0.27

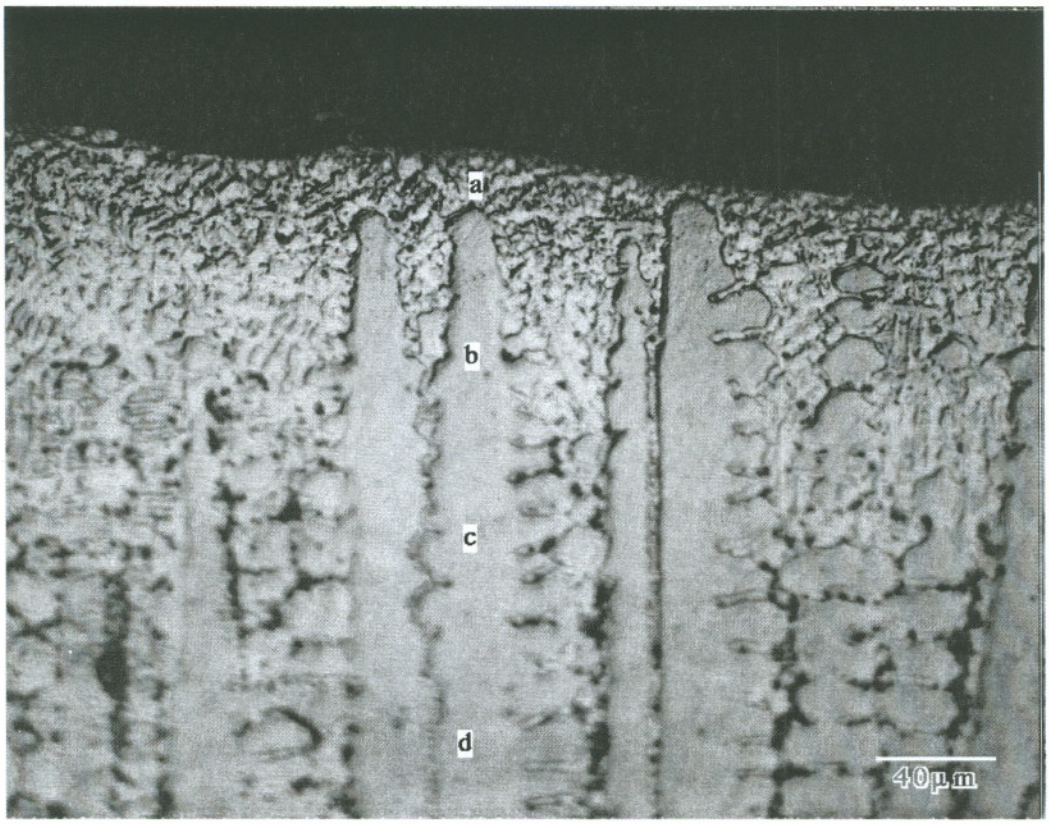

Figure 4.20 The Locations (a, b, c, d) of the Composition Measurement in the Dendritic Structure of the Water Quenched Nickel Alloy 625 Cladding Deposited on Class 1 Steel.

Weld Metal Microstructure

The cladding deposit consisted of an unmixed zone and a composite zone. The unmixed zone in the cladding was a band of melted base metal in between the composite zone and base metal. It had been melted and solidified during the cladding process and had not been mechanically mixed with filler metal. The composite zone contained a mixture of filler metal and base metal. A small region of the steel surface was melted and

mixed with filler metal; and the elements from the melted steel were incorporated and homogenized into the liquid phase.

The unmixed zone

Regardless of the strip/base metal composition, the cladding contains an unmixed zone, although it was not always visible. Figure 4.21 shows an interface region of nickel alloy 625 deposited on class 1 steel. The unmixed zone in this cladding could not be identified because steel undergoes a solid state phase transformation. The solidification structures of the unmixed zone could not be preserved to room temperature. Since it had the same composition and structure (after the phase transformation) as the base metal, it was often considered as part of HAZ. Table 4.10 summarizes the unmixed zone in different cladding conditions.

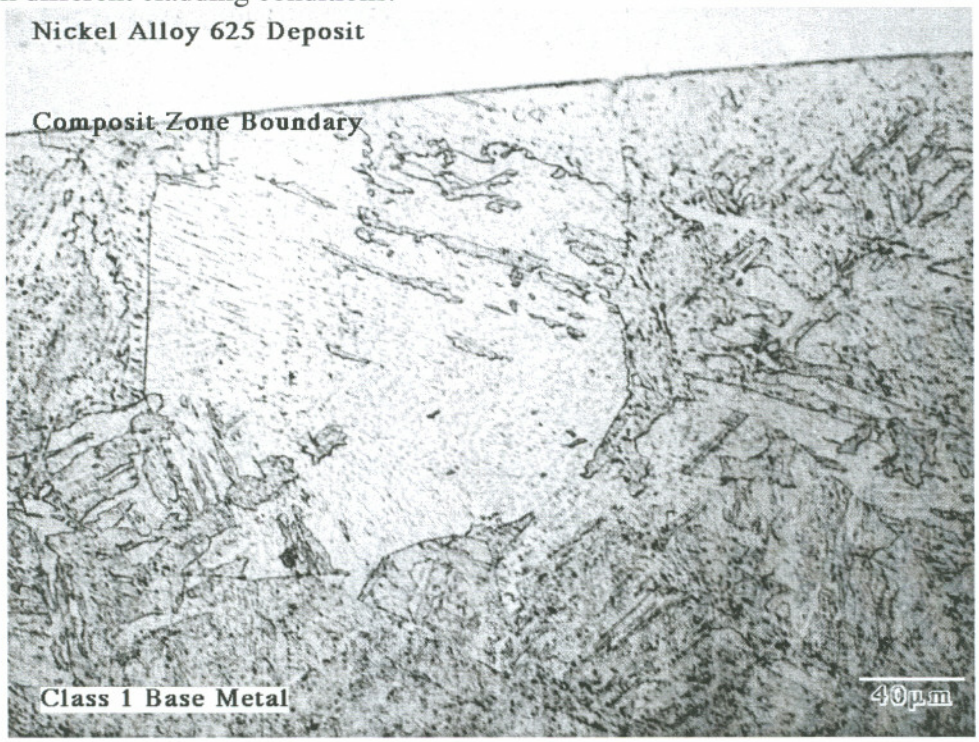

Figure 4.21 Interface of Nickel Alloy 625 Deposit on Class 1 Shafting Steel by ESS process, No Visible Unmixed Zone.

Table 4.10 Effect of Filler Metal and Base Metal Compositions on the Formation of the Unmixed Zone

Filler Metal	Base Metal	$\Delta T=T_{mF}-T_{mB}$°C	Unmixed Zone	Welding Process
Ni Alloy 625	Class 1 Steel	–220	invisible[1]	ESS
Ni Alloy 625	304 SS	–115	yes	ESS
Ni Alloy 625	316 SS	–93	yes	ESS
–	625 ESS Deposit	–0	invisible[2]	GTA Remelting
–	70/30 Cu-Ni ESS Deposit.	–0	invisible[2]	GTA Remelting
70/30 Cu-Ni	304 SS	–230	yes	ESS
70/30 Cu-Ni	316 SS	–208	yes	ESS
304 SS	304 SS	–0	invisible[2]	ESS
Mild Steel	304 SS	+105	yes	ESS

ΔT the melting temperature difference between filler metal (T_{mF}) and base metal (T_{mB}).
[1] Due to solid state phase transformation.
[2] No structural or compositional difference between the unmixed and composite zone.

It was observed that the unmixed zone existed in both 70/30 Cu-Ni alloy and nickel alloy 625 surfacing deposited on 316 stainless steel. Even the melting temperatures of the two strips were lower than that of the 316 stainless steel base metal (208 and 93°C lower than 316 stainless steel for 70/30 Cu-Ni alloy and nickel alloy 625, respectively). In contrast to the low melting temperature of filler metal, a mild steel strip was deposited on 304 stainless steel which had a positive temperature difference about 105°C, yet, similar unmixed zone was still observed. The existence of the unmixed zone was not affected by the melting temperature difference in the ESS. The depth of the unmixed zone could be as deep as 75 μm.

When nickel alloy 625 was deposited on 316 stainless steel base metal, the unmixed zone consisting of melted 316 stainless steel solidified as primary austenite cells

or cellular dendrites with ferrite in the interdendritic regions, as shown in Figure 4.22. The EDS compositional analyses showed that the unmixed zone had a chemical composition identical to that of the base metal, as shown in Table 4.11 and 4.12 for 316 and 304 stainless steel base metals, respectively.

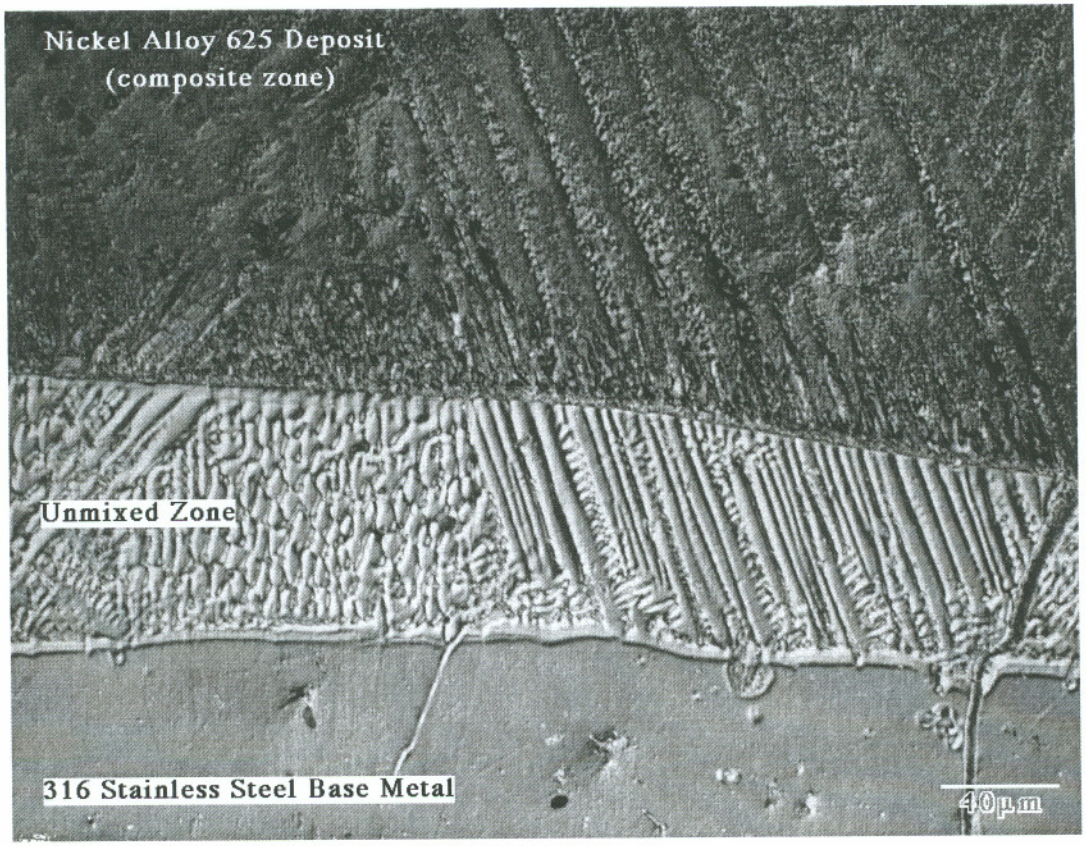

Figure 4.22 Microstructure of the Unmixed Zone in Electroslag Surfacing on 316 Stainless Steel Base Metal using Nickel Alloy 625 Strip Electrodes.

Table 4.11 EDS Analysis of the Unmixed Zone and Composite Zone in Nickel Alloy 625 Deposited on 304 Stainless Steel by ESS (Compared with the Base Metal and Filler Metal Composition)

	304 Stainless Steel Base Metal	Unmixed Zone	Composite Zone	Filler Metal Nickel Alloy 625
Mn	2.01	2.02	0.23	0.03
Fe	68.7	68.0	9.36	0.95
Si	0.86	0.84	0.11	0.04
Ni	8.81	9.12	56.9	63.5
Cr	19.3	19.3	22.5	22.5
Mo	0.19	0.12	7.73	9.32
Nb			2.71	3.47

Table 4.12 EDS Analysis of the Unmixed Zone and Composite Zone in Nickel Alloy 625 Deposited on 316 Stainless Steel by ESS (Compared with the Base Metal and Filler Metal Composition)

	316 Stainless Steel Base Metal	Unmixed Zone	Composite Zone	Filler Metal Nickel Alloy 625
Mn	1.75	1.69	0.20	0.03
Fe	64.3	63.7	9.42	0.95
Si	0.33	0.28	0.09	0.04
Ni	12.2	12.9	57.0	63.5
Cr	18.5	19.3	22.2	22.5
Mo	2.85	2.99	8.24	9.32
Nb			2.62	3.47

The liquid weld metal (melted base metal) in the unmixed zone solidified on solid base metal. Like autogenous welding or matched filler metal welding, most grains epitaxially initiated at the weld interface and grew into the unmixed zone as shown in Figure 4.23. The microstructure in the unmixed zone was cellular dendritic. The early stage of competitive growth also took place in this zone. The favorably oriented grains also outgrew the poorly oriented grains in this zone.

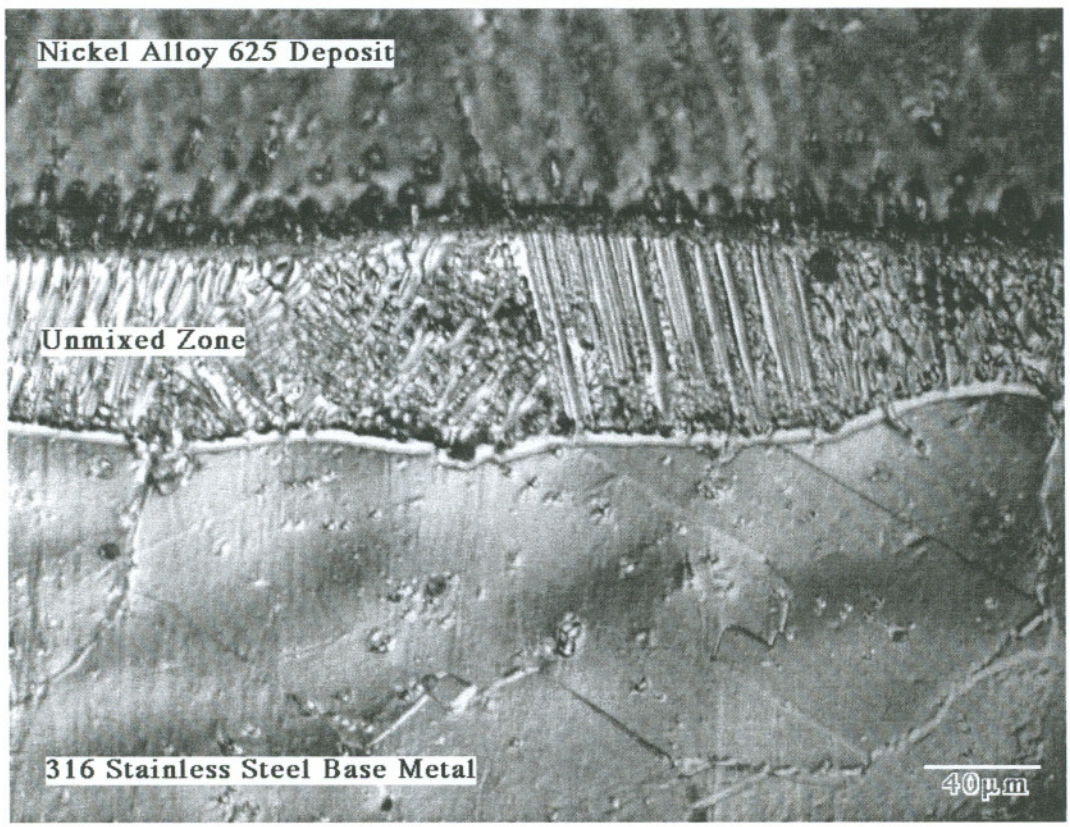

Figure 4.23 Epitaxial Growth in the Unmixed Zone of Nickel Alloy 625 Deposited on 316 Stainless Steel by ESS.

The composite zone

The chemical compositions of the composite zones of nickel alloy 625 deposited on stainless steels are listed in Table 4.11 and 4.12 for 304 and 316 stainless steels, respectively. The cladding contained a diluted composition of nickel alloy 625. Similar to nickel alloy 625 deposited on steel, the microstructural morphology of as-welded nickel alloy 625 was completely different from that of wrought alloy. The wrought alloy microstructure was fine-grained (usually ASTM 8) and homogenous containing no Laves phase. The as-welded nickel alloy 625 was large-grained (ASTM 0) and heavily segregated composite-like structure. The microstructure of the as-welded nickel alloy 625 composite zone consisted of a dendritic f.c.c. γ solid solution of nickel, chromium, and iron; as well as carbides and Laves phase in the interdendritic regions. The production of those interdendritic constituents was a result of non-equilibrium solidification.

Primary dendrite arm spacing increased from the root of the cladding bead to the top surface due to the changes in thermal conditions, however, it was interesting to note that the increase in the primary dendrite arm spacing did not eliminate the number of cellular dendrites as it often did in the casting.[188] The grains laterally expanded themselves to compete with/eliminate neighboring grains, as a result, fewer grains survived at the end of solidification as shown in Figure 4.24.

Figure 4.24 The Grain Structure of Five Layer Nickel Alloy 625 Deposited on Class 1 Shafting Steel by ESS

WELD METAL SOLUTE REDISTRIBUTION MODEL

To more accurately quantify the solute redistribution during dendritic solidification and eliminate the large discrepancies found in many existing models, a model is derived based on Kobayashi's approximate solution for dendritic solidification[133] which has sufficiently good accuracy in comparison to his exact theoretical solution to the Brody-Flemings model.[130] In addition to the approximate solution, the new model takes multi-component alloy systems into account with a variable partition coefficient throughout solidification (which was often assumed as a constant in the existing models).

Model and Its Assumptions

A cylindrical coordinate system is used in this model. The assumed dendrite geometry is illustrated as in Figure 4.25. The solidification proceeds towards y-direction and ends when the position on the solid/liquid interface Y arrives at the position $y=L$. The length L corresponds to one half of the dendrite spacing, $\lambda/2$. The position $y=0$ corresponds to dendrite core. Assumptions for this model include:

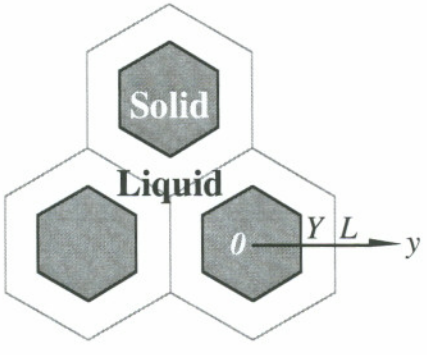

Figure 4.25 The Cylindrical Coordinate Used in this Model.

(a) Back diffusion of solute in the solid during solidification is incorporated in this model. The solute transport in the solid is controlled by diffusion with a diffusion coefficient independent of concentration. For a cylindrical coordinate system, it can be described as:

$$\frac{\partial Cs}{\partial t} = D\frac{\partial}{y\partial y}(y\frac{\partial Cs}{\partial y}) \qquad [4.3]$$

where C_S is the solute concentration in solid (wt%); and

D is the solute diffusion coefficient in solid (m^2/s).

(b) Diffusion and mechanical mixing (convection) in the liquid is complete. The solute concentration in the liquid is often assumed to be controlled completely either by solute diffusion or by liquid convection or both. The interdendritic liquid is assumed to have a uniform composition, $C_L = C_L^*$, where C_L is the nominal solute concentration in the liquid and C_L^* is the solute concentration at the solid/liquid interface.

(c) The density of the material is a constant from room temperature to melting temperature, and equal for both solid and liquid phases. Shrinkage is neglected during solidification. The area fraction of solid f_S and fraction of liquid f_L are described as:

$$f_S = \left(\frac{Y}{L}\right)^2 \quad and \quad f_S = 1 - f_L \qquad [4.4]$$

(d) The solidification is a linear continuous function,

$$f_S = \frac{t}{tf} \qquad [4.5]$$

where tf is the local solidification time in seconds.

(e) The partition coefficient k applied at the solid/liquid interface is a temperature dependent function, it can be described as:

$$k = aT + b \qquad [4.6]$$

where T is the temperature in K, a and b dimensionless are constants for a given element in a certain alloy system.

If k is assumed to be linearly dependent on temperature. k then:

$$k = a\frac{\Delta T}{\lambda} f_s + b \qquad [4.7]$$

where ΔT is the freezing range, λ is the dendrite arm spacing.

(f) The solute is conserved within the volume element of consideration, therefore no mass flow into or out of the volume element occurs,

$$\frac{2f_s}{Y^2}\int_0^z C_s Y \partial y + \frac{C_s^*}{k} f_L = C_0 \qquad [4.8]$$

where C_0 is the initial alloy concentration.

By using Z, an intermediate dimensionless parameter which represents the position in the volume element:

$$Z = \frac{(y/Y)^2}{2\gamma} \quad \text{and} \quad Z_0 = \frac{1}{2\gamma} \qquad [4.9]$$

where the γ is the back diffusion parameter for dendrites

$$\gamma = \frac{8Dtf}{\lambda^2} \qquad [4.10]$$

Substituting t with f_S in the diffusion equation [4.3] and replacing y with z and k with equation [4.7] in the mass balance equation [4.8], the following equations [4.11, 4.12] are obtained

$$f_S \frac{\partial C_S}{\partial f_S} = (1+Z) \frac{\partial C_S}{\partial z} + Z \frac{\partial^2 C_S}{\partial z^2} \qquad [4.11]$$

and

$$\frac{f_S}{z_0} \int_0^{z_0} C_S \partial z + \frac{\lambda C_S^*}{a \Delta T f_S + b} (1-f_S) = C_0 \qquad [4.12]$$

An approximate solution of the model can be derived (if the second order component is being neglected) from applying the integral to equation [4.11] and differentiating equation [4.12]. So C_S can be described as function of f_S, $C_S=f(f_S)$, using the boundary condition that $C_S = kC_0$ for $f_S=0$.

$$E = a\frac{\Delta T}{\lambda}; \quad Ef_S + b = \theta; \; E + b = G \qquad [4.13]$$

$$(\frac{G}{\theta}-1)E\frac{\partial C_S}{\partial \theta} - (\frac{G}{\theta^2}-1)C_S + \frac{\partial C_S}{\partial z} = 0 \qquad [4.14]$$

$$\frac{\partial C_S}{\partial z} = 0 \quad \text{for } z=0.$$

A computer program was created and used to calculate the solute elements redistribution during the weld metal solidification.

Model Predictions and Validation

Niobium is a very important alloying element in the nickel alloy 625 and it is distinguished by its extreme segregation behavior compared to other alloying elements in this alloy system. The niobium segregation directly affects the solidification cracking susceptibility of the weld metal. Therefore, niobium has been used, as an example, throughout this model. However, the model does not necessarily have to be restricted to niobium only. The initial values for niobium used in this model are listed in Table 4.13.

Table 4.13 The Initial Values for the Model for the Solute Redistribution of Niobium during Solidification of Nickel Alloy 625 Cladding

	ESS (6 kJ/mm)	ESS (9 kJ/mm)	SAS (6 kJ/mm)
C_{0Nb} (wt%)	2.84	2.97	2.82
λ (μm)	88.5	120	89.0
tf (sec.)	21.0	44.9	22.6
a†	-1.29	-1.29	-1.29
b†	1.2×10^{-3}	1.2×10^{-3}	1.2×10^{-3}
ΔT	75.1	75.1	80.7
D_S	$5.6\times10^{-6}\exp(-2.8\times10^{5}/RT)$	$5.6\times10^{-6}\exp(-2.8\times10^{5}/RT)$	$5.6\times10^{-6}\exp(-2.8\times10^{5}/RT)$

† values for niobium is from reference (98)
Where R is the universal constant (8.31 J/K·mol)
T is the mean temperature value of the solidus and liquidus of the cladding in K.

The calculated solute redistribution profiles of niobium from this model are shown in Figure 4.26. It predicted a 12.5% interdendritic liquid fraction when niobium concentration in the interdendritic liquid reached 12.6 wt%. Figure 4.27 is the SEM image of the interface quenched cladding of nickel alloy 625 which measured a 12.7% interdendritic liquid fraction at the same niobium concentration level (12 wt%). Niobium was the most segregated element in this alloy system according to the partition

coefficient. The development of microsegregation was accelerated as the temperature dropped during solidification due to the changes in the partition coefficient. Figure 4.28 is the result of model prediction of niobium concentration in the interdendritic liquid at different solidification stages. Figure 4.29 to Figure 4.31 are the SEM micrographs corresponding to the different solidification stages. The model prediction and the experimental results are summarized in Table 4.14.

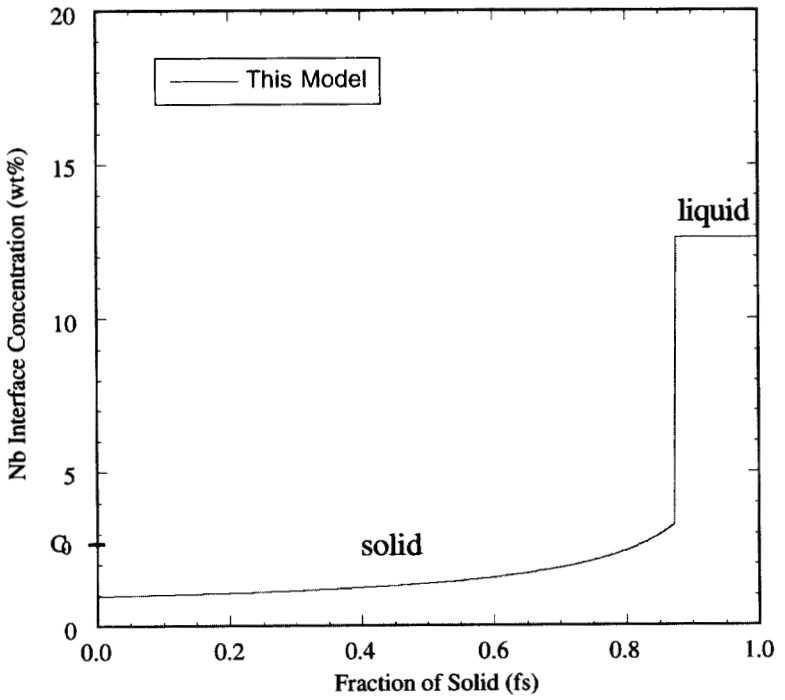

Figure 4.26 The Model Predicted an Interdendritic Liquid Fraction of 12.5% when the Nb Concentration in the Liquid is Equal to 12.6 (wt%).

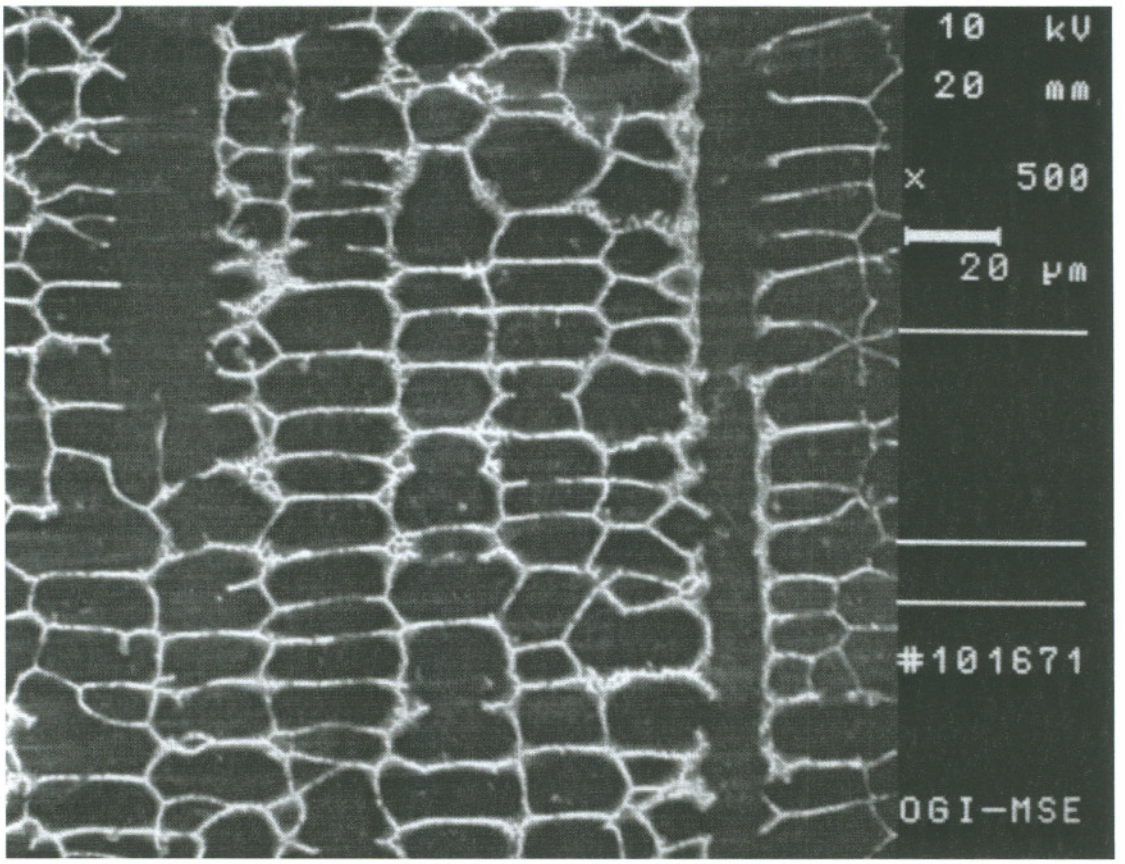

Figure 4.27 SEM Backscatter Image of the Interdendritic Liquid from the Quenched Interface Cladding, at the Stage where $C_{L_{Nb}}$ is Reached to 12.6 wt% in the Liquid (Liquid Fraction = 12.5%). The Bright Area is the Water-Quenched Interdendritic Liquid Network, Dark Area is the Dendrite.

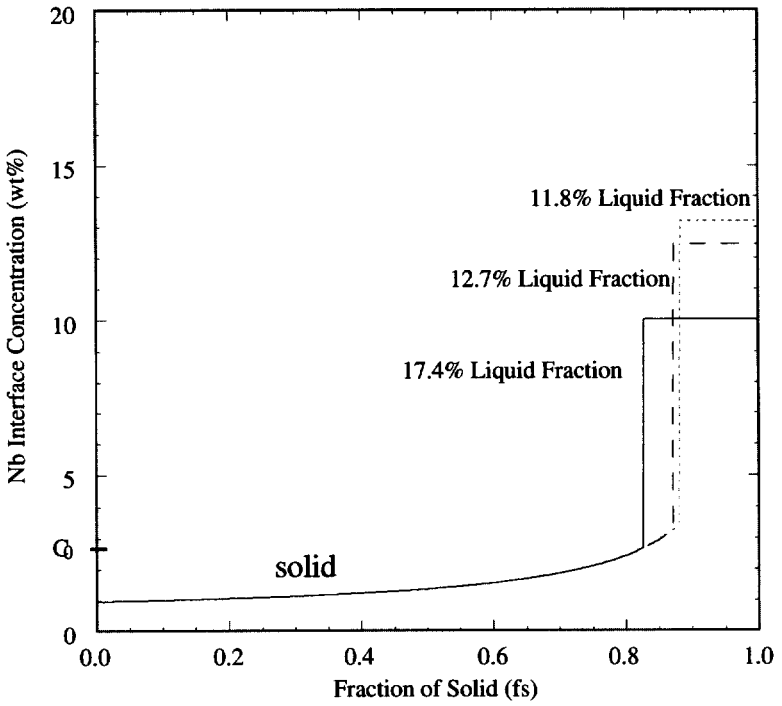

Figure 4.28 Comparison between Predicted and Experimental Data for Interdendritic Liquid Fraction at Different Nb Concentration Level.

Table 4.14 Comparison of Experimental Data with the Model, Nb Concentration in the Interdendritic Liquid of Nickel Alloy 625 Cladding

% of Liquid Fraction	Experimental $C_{L_{Nb}}$ (wt%)	Model $C_{L_{Nb}}$ (wt%)
17.4	9.99	10.04
12.7	12.5	12.46
11.8	13.2	13.20

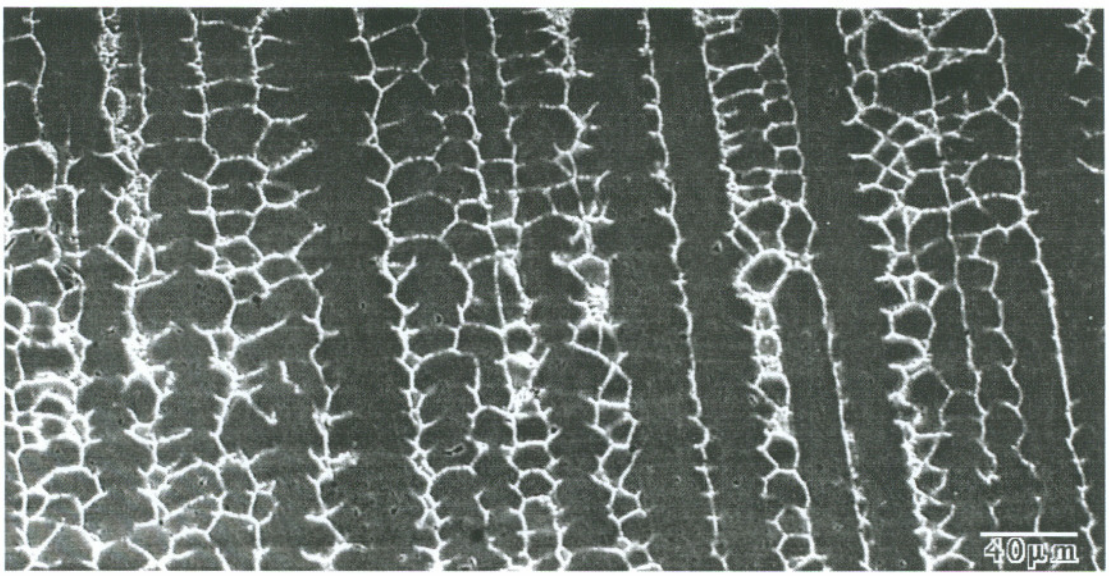

Figure 4.29 SEM Backscatter Image of the Interdendritic Liquid from the Quenched Interface Cladding, at the Stage where $C_{L_{Nb}}$ is Reached to 9.99 wt% in the Liquid (Liquid Fraction = 17.4%). The Bright Area is the Water-Quenched Interdendritic Liquid Network, Dark Area is the Dendrite.

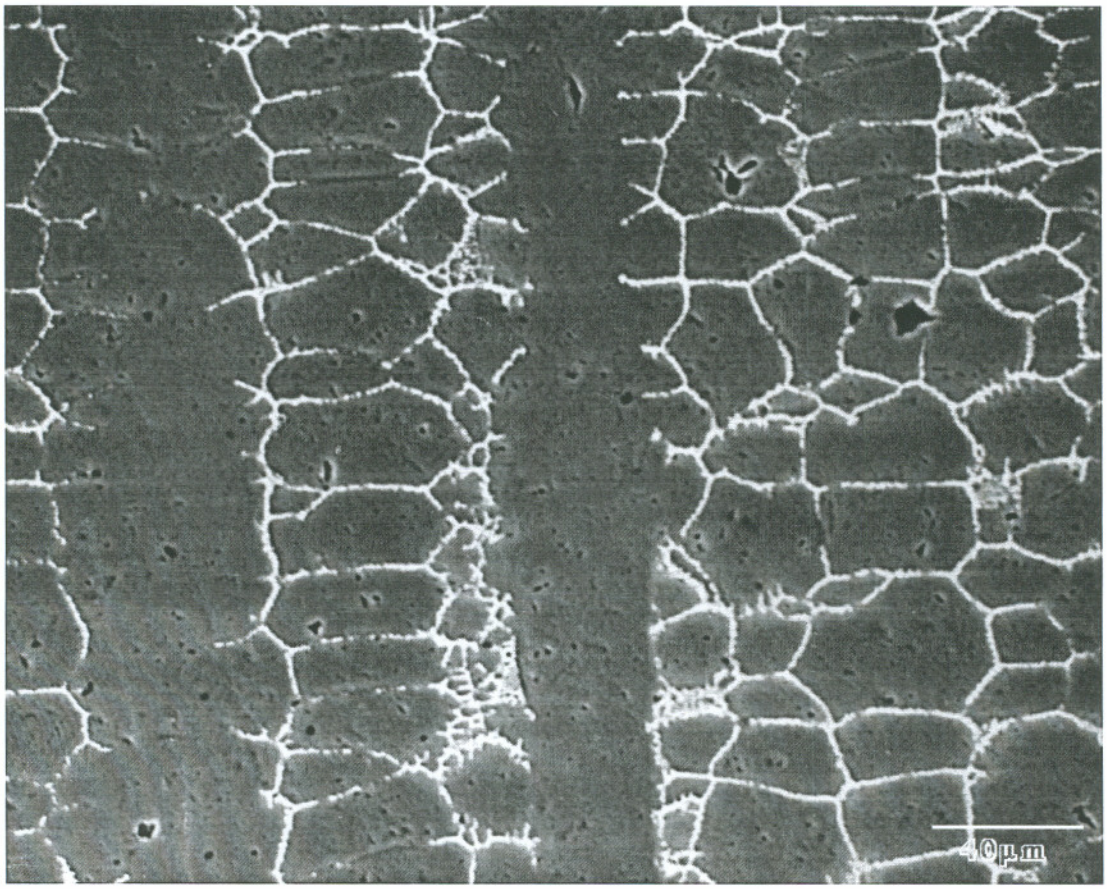

Figure 4.30 SEM Backscatter Image of the Interdendritic Liquid from the Quenched Interface Cladding, at the Stage where $C_{L_{Nb}}$ is Reached to 12.5 wt% in the Liquid (Liquid Fraction = 12.7%). The Bright Area is the Water-Quenched Interdendritic Liquid Network, Dark Area is the Dendrite.

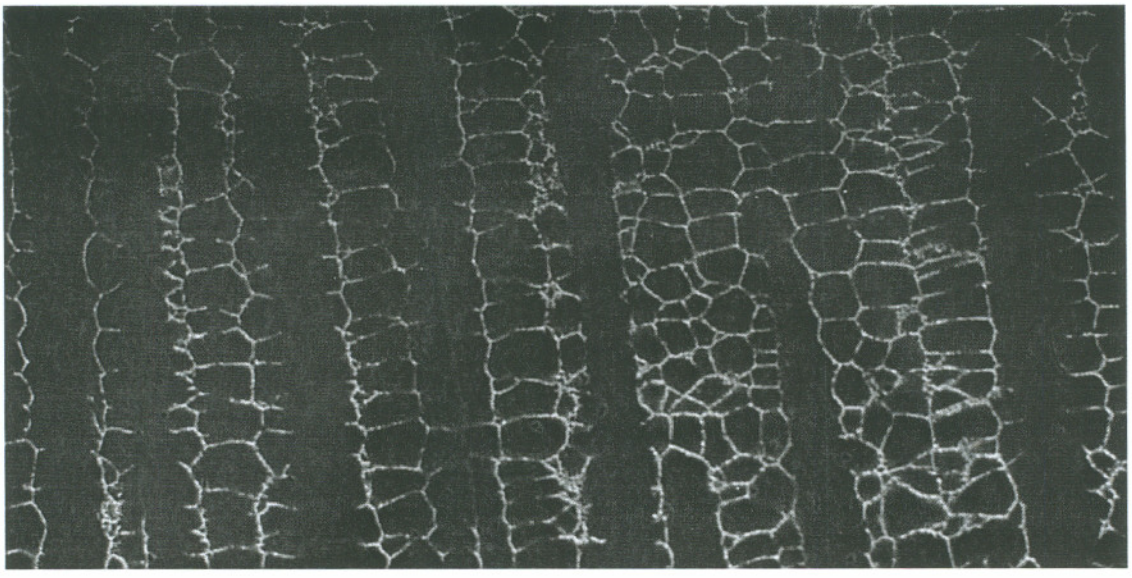

Figure 4.31 SEM Backscatter Image of the Interdendritic Liquid from the Quenched Interface Cladding, at the Stage where $C_{L_{Nb}}$ is Reached to 13.2 wt% in the Liquid (Liquid Fraction = 11.8%). The Bright Area is the Water-Quenched Interdendritic Liquid Network, Dark Area is the Dendrite.

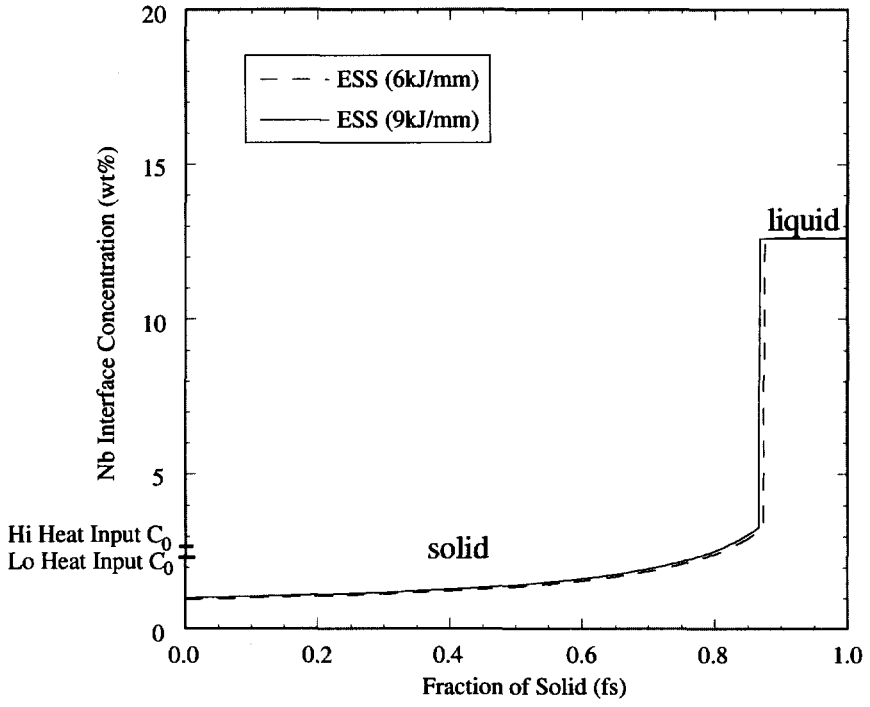

Figure 4.32 Predicted Interdendritic Liquid Fraction for Different Heat Input Cladding by ESS at $C_{L_{Nb}}$ = 12.6 (wt%).

Figure 4.32 shows the model's result for the different heat input claddings. The model predicted a 13.3% interdendritic liquid fraction for high heat input cladding and 12.5% for the normal heat input cladding when niobium concentration in the liquid reached 12.6 wt%. The difference in the predicted result by the model was attributed to a higher initial niobium content in the high heat input cladding due to the smaller dilution. Although longer solidification time (doubled in the high heat input cladding) normally reduced the degree of segregation, the influence on segregation by diffusion was very limited for niobium.

SOLIDIFICATION CRACKING SUSCEPTIBILITY

Both ESS and SAS processes were tested with nickel alloy 625 strip. Under a identical cladding conditions, the cracking indices (CI) were 1/3 and 2/3 for ESS and SAS, respectively. The increased solidification cracking tendency in SAS was attributed to the wider melting range and more interdendritic precipitates. The results of solidification cracking test for different cladding materials are listed in Table 4.15. These tests were performed under the same cladding conditions using both the ESS process and the SAS process. Among those tested cladding materials, 308L stainless steel exhibited the best cracking resistance with a cracking index (CI) of 0. 70/30 Cu-Ni showed the worst cracking resistance (CI=1), cracking through the entire width of the cladding bead. Nickel alloy 625 demonstrated a moderate cracking resistant in this group. Table 4.16 shows the effect of cladding variables on solidification cracking susceptibility for nickel alloy 625 electroslag surfacing. For the same heat input, the nickel alloy 625 exhibited a similar cracking tendency when cladding travel speed varied from 102 to 178 mm/min. However, for the same cladding travel speed, solidification cracking tendency increased as heat input increased. The cracking index increased from 1/3 to 2/3 for 6 to 9 kJ/mm heat input, respectively.

Table 4.15 Cracking Index (CI) of 30 mm Strip Deposit on 25 mm Thick MIL-S-23284, Class 1 Steel

	Nickel Alloy 625	Nickel 625L Fe	Nickel Alloy 59	Nickel 200	70/30 Ni-Cu	70/30 Cu-Ni	308L Stainless
ESS	1/3	1/4	1/8	1/2	1/3	1	0
SAS	2/3	-	1/4	-	2/3	1	0

Table 4.16 Effect of Cladding Variables on Solidification Cracking Susceptibility (CI) Nickel Alloy 625 Cladding Deposited by ESS		
	Travel Speed =102 mm/min.	Travel Speed=178 mm/min.
Heat Input = 6 kJ/mm	1/3	1/3
	Heat Input = 6 kJ/mm	Heat Input = 9 kJ/mm
Travel Speed =178 mm/min.	2/3	1/3

Figure 4.33 illustrates a typical fracture of the OGI solidification cracking test. The fractured cladding bead could be categorized into three distinct zones as indicated in the Figure 4.33. In Figure 4.33, zone 1 exhibited an interdendritic fracture or solidification cracking. The secondary dendrite arms were clearly observed as shown in Figure 4.34. The secondary arms gradually became obscure from zone 1 to zone 2. Zone 2 showed a groove-like morphology and those grooves were parallel to the growing direction of the columnar dendrite as shown in Figure 4.35 and among these grooves non-metallic inclusions were observed on the fractured surface. Zone 3 was the ductile overload fractured region. This portion of the cladding bead survived from the solidification cracking test and was pulled apart at the room temperature. It showed a ductile fracture feature as shown in Figure 4.36.

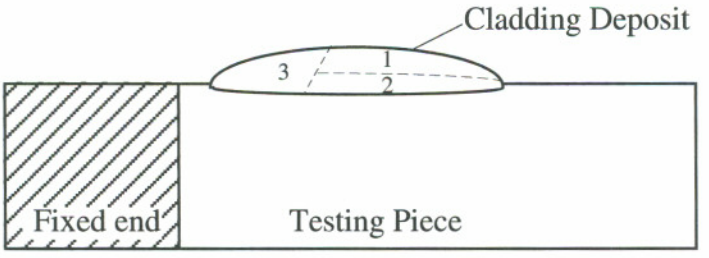

Figure 4.33 Illustration of Solidification Fracture Surface of the Solidification Cracking Test. Numbers 1, 2, and 3 indicate different fracture feature zones: zone 1 & 2 are solidification fracture regions, 3 is ductile overload fractured.

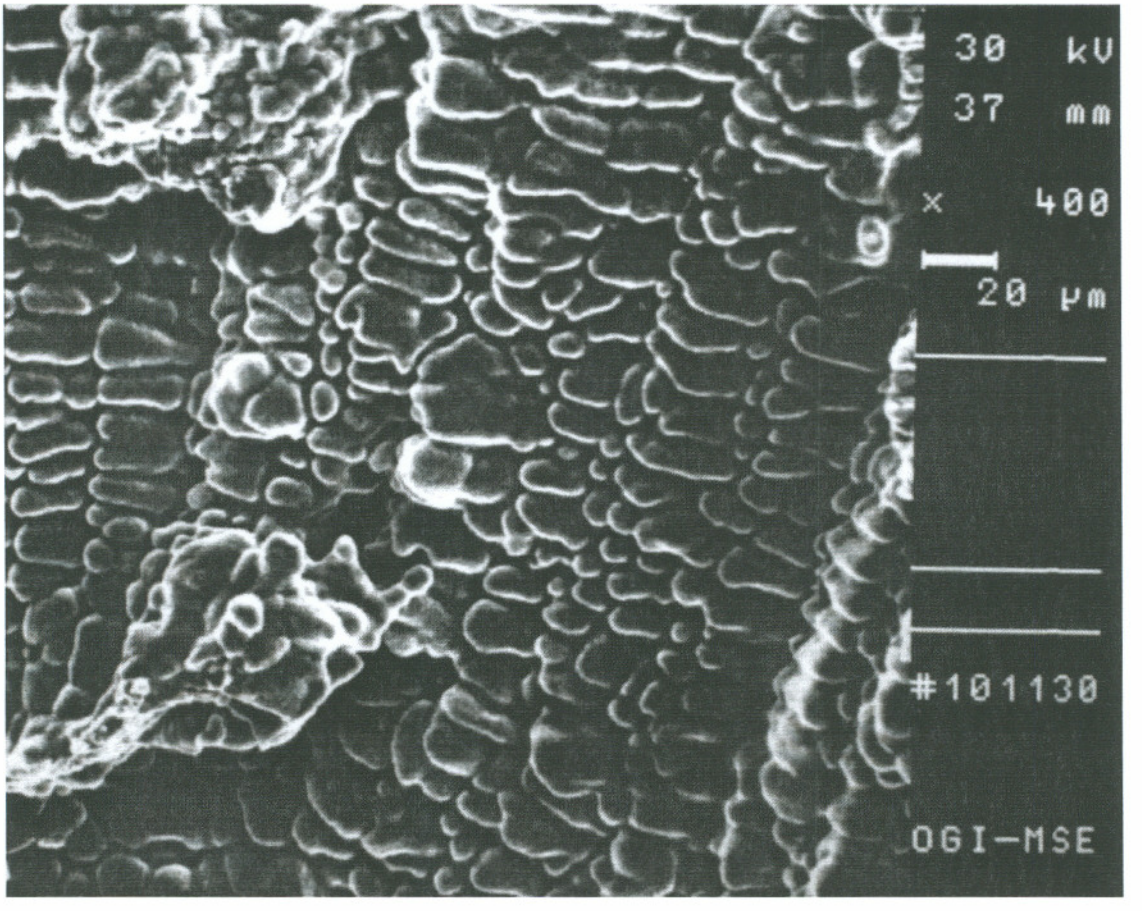

Figure 4.34 Solidification Cracking Morphology of Dendritic Fracture in Nickel Alloy 625 Cladding, Corresponding to Zone 1 in Figure 4.33.

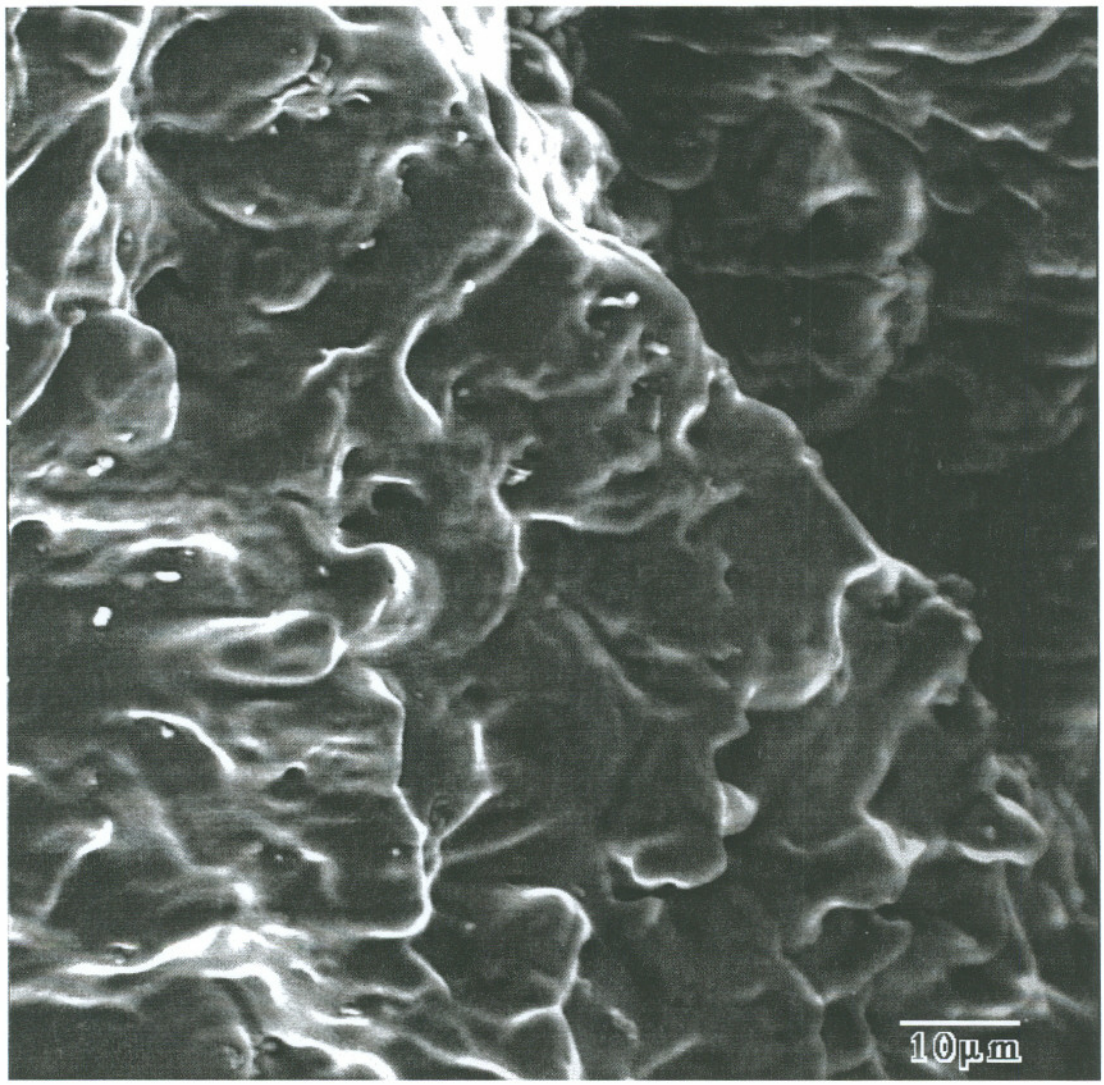

Figure 4.35 Solidification Cracking Surface of Nickel Alloy 625 Cladding Showed a Groove Morphology, Corresponding to Zone 2 in Figure 4.33.

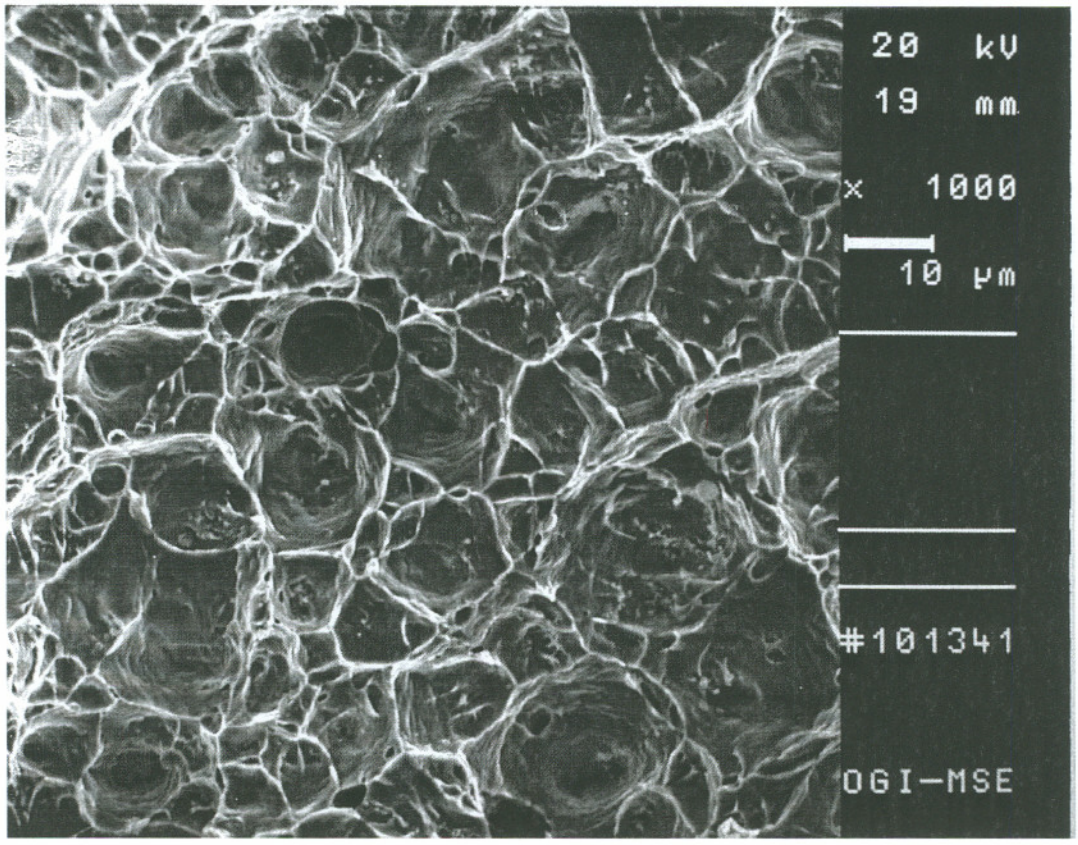

Figure 4.36 Ductile Fracture of the Non-cracking Cladding Bead Portion in Nickel Alloy 625 Cladding by ESS, Corresponding to Area 3 in Figure 4.33.

CHAPTER V

DISCUSSION

WELD METAL MICROSTRUCTURE EVOLUTION

Formation of the Unmixed Zone

The unmixed zone is a part of the base metal which is melted during welding but is not mechanically mixed with other liquid phase, and it still keeps its chemical composition identical to that of the base metal. It was speculated by Matthews[99], Savage[100], Lundin[103], and Lukkari[101] that the size and formation of the unmixed zone were related to the melting temperature difference between filler metal and base metal and the heat input of welding. They concluded that the greater the positive temperature difference (filler metal melting temperature > base metal melting temperature), the larger the unmixed zone and the higher heat input, the larger the unmixed zone. However, in the dissimilar metal cladding by the ESS process, it is observed that the unmixed zone exists regardless of the melting temperature and composition differences between the filler metal and the base metal. It seems that the unmixed zone is not affected by the melting temperature of the filler metal. In the ESS process, when the alloys, such as 70/30 CuNi (T_m=1170°C), 70/30 NiCu (T_m=1308°C), nickel alloy 625 (T_m=1285°C), and mild steel (T_m=1505°C), are deposited on stainless

steel 316 (T_m=1378°C), all cladding contain an unmixed zone even when the filler metal melting temperature is substantially lower than that of the base metal. Table 4.10 has summarized the existence of the unmixed zone in electroslag surfacing.

For those welds, of which the base metals undergo solid state phase transformation in the HAZ area, the unmixed zone usually can not be identified. As seen in Figures 4.21 and 5.1, the line which separates two different microstructures is the interface between the unmixed zone and the composite zone. However, the unmixed zone in those cases is often regarded as part of the HAZ.

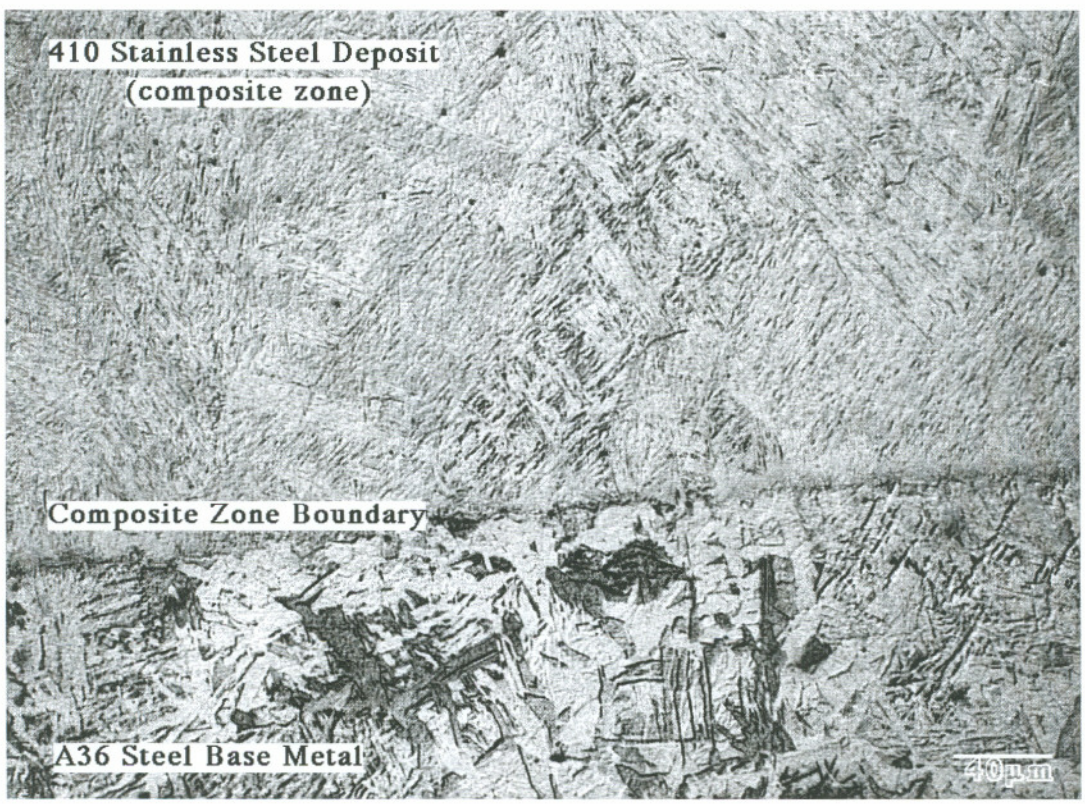

Figure 5.1 Interface Regions of 410 Stainless Steel Deposited on A36 Steel by ESS. The top portion is the cladding composite zone and the bottom portion is the A36 steel. The unmixed zone can not be seen here. The interface in this figure is the boundary of composite zone and unmixed zone.

On the other hand, for autogenous welding or matched filler metal welding, the unmixed zone exists in the weldment theoretically. However, it has no difference in chemical composition with the rest of the weldment. And it has the same structure as the composite zone. The unmixed zone in these cases is invisible from the metallurgical point of view. Figure 5.2 shows the interface region of 304 stainless steel deposited on 304 stainless steel by ESS process. The fusion boundary (welding interface) can be seen. However, no unmixed zone is seen in this cladding. The unmixed zone could not be differentiated from the composite zone since it has an identical structure and composition to those of the composite zone. Figure 5.3 exhibits grain substructures of an autogenous welding of nickel alloy 625. The upper portion shows that fine dendrites are GTA remelted no a nickel alloy 625 ESS deposit (lower portion). Again no unmixed zone can be seen in this GTA weld deposit.

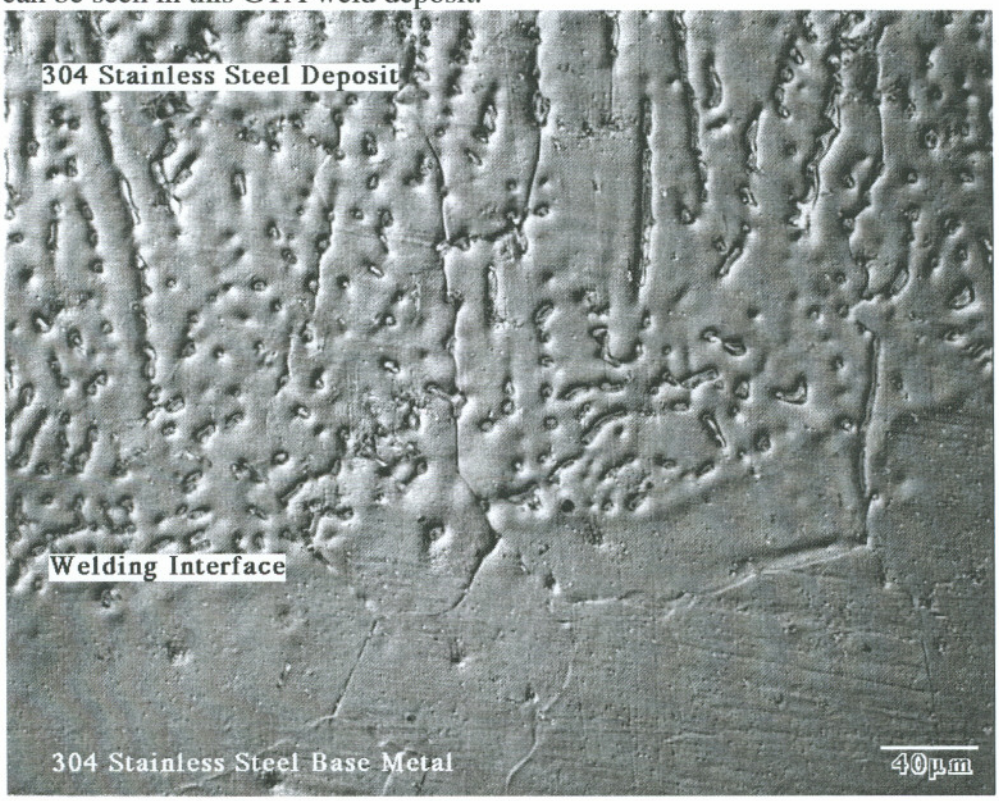

Figure 5.2 Optical Micrograph of the Interface Region of 304 Stainless Steel Deposited on 304 Stainless Steel (Matched Filler Metal) by ESS.

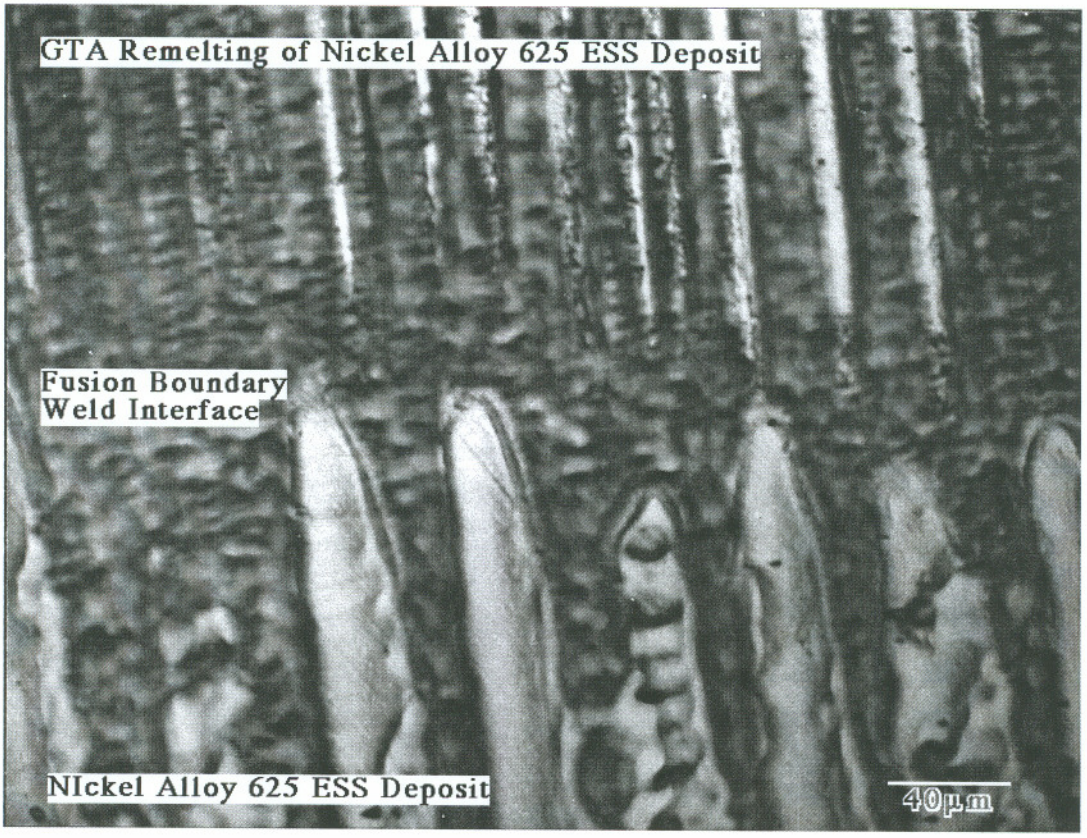

Figure 5.3 Optical Micrograph of the Interface Region of Nickel Alloy 625 ESS Deposit Remelted by GTA Autogenous Welding.

The Composite Zone

The composition of the composite zone is diluted by the base metal to form an admixture. A small region of the base metal is surface-melted by the welding pool and mixed with the cladding material. The elements from the melted steel are incorporated and homogenized in the liquid phase. Figure 5.4 shows the microstructure of the composite zone of nickel alloy 625 deposited on class 1 steel. The grains are basically aligned in the direction perpendicular to the base substrate. Competitive growth is still the governing mechanism of growths.

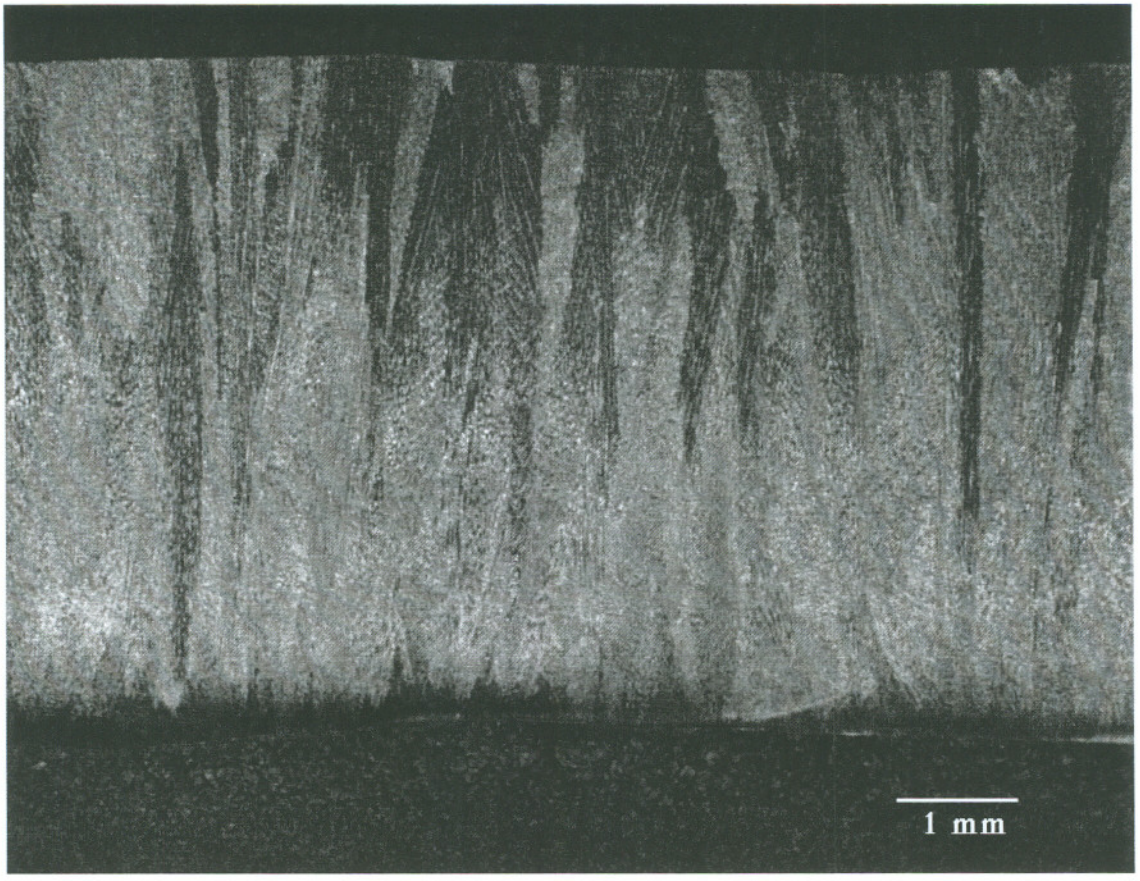

Figure 5.4 Grain structures of the Composite Zone in Nickel Alloy 625 Deposited on Class 1 Steel.

Weld Metal Microstructure Evolution

The microstructure evolution in the dissimilar metal cladding by ESS can be described as following:

Melted base metal (the unmixed weld metal) is in intimate contact with the solid base metal with composition identical to each other. Due to the existence of unmixed zone in the dissimilar metal weld, the early stages of weld metal solidification in the dissimilar metal weld is essentially the same as autogenous or matched filler metal welding. The solidification of the weld metal is initiated by arranging atoms from the

liquid phase on the existing crystalline substrate, thereby the grains in the base metal extend themselves without altering the crystallographic orientation. The conventional theory of epitaxial growth is still applicable in the dissimilar metal welding. The epitaxial growth is the dominate event in the grain initiation of the weld metal solidification. The growth direction of grains would have been the direction perpendicular to the solid/liquid interface because of the maximum temperature gradient and the maximum driving force for solidification, if grains did not have their own preferred growth direction. For cubic metals, the preferred growth direction is <100> and there are three of them perpendicular to each other. Therefore, during solidification, grains grow rapidly in the direction where their easy growth direction is closest to the direction of the maximum thermal gradient. In ESS, the solid/liquid interface at the front portion of the weld pool is flat. The direction of the maximum thermal gradient is perpendicular to the base substrate (vertical) and irrespective to the cladding direction. For the randomly oriented base metal grains, they grow on the side of which the easy growth direction is more parallel to the direction of the maximum temperature gradient. The closer the easy growth direction is to the direction of the maximum temperature gradient, the easier the grains grow. In the grain growth process, the grains compete with each other based on their orientation preference, i.e. competitive growth. Those grains with their easy growth direction normal to the base substrate will grow more easily and crowd out those grains whose easy growth direction deviates significantly from that direction.

The unmixed zone plays a significant role in the microstructure development in dissimilar metal welding. With the unmixed zone, the weld metal solidifies on the solid base metal epitaxially as it does in the autogenous welding. However, the presence of the unmixed zone has also created a second interface in the weld metal and that has moved the solidification front toward a place where the thermal gradient is less than that of the

first interface because of lower thermal conductivity in the unmixed zone. This smaller thermal gradient promotes the type "B" grain boundary formation near the secondary interface.

Only those favorably oriented grains extend toward the composite zone. The unfavorably oriented grains either are eliminated or lose growth momentum which causes the new grain formation near the second interface in the composite zone. As grains grow across the boundary between the unmixed zone and the composite zone, the thermal gradient reduces significantly. Figure 5.5 shows the unmixed zone and the composite zone of nickel alloy 625 deposited on 304 stainless steel. It is clearly seen that a new grain is formed in the composite zone and type B grain boundary is created.

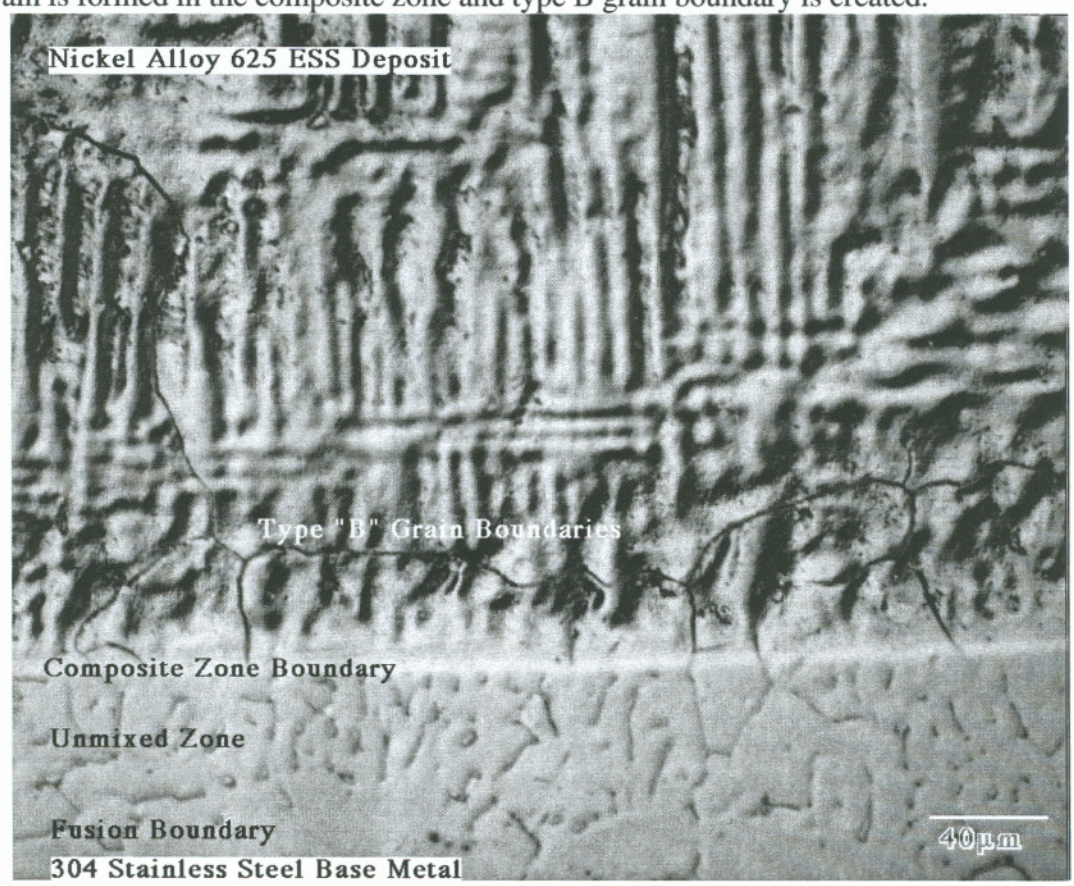

Figure 5.5 Microstructure of the Interface Region of Nickel Alloy 625 Deposited on 304 Stainless Steel Base Metal by ESS.

As the grains grow into a region where the solid/liquid interface is no longer a flat region, the direction of maximum thermal gradient is tilted towards the cladding direction. However, those grains at this stage, have survived from the competition and have been aligned very well in the direction which is normal to the base metal. Although the maximum thermal gradient has changed its direction, this change is not enough to stop grain growth or bend its growth direction. Grain growth is continued towards the top of the bead without altering its growth direction as shown in Figure 5.4. There is no grain bending in the electroslag surfacing process.

SOLIDIFICATION MODELING

The model based on Kobayashi's approximate solution for dendritic solidification with a variable partition coefficient has effectively predicted niobium redistribution during the solidification of nickel alloy 625 cladding. The changes in distribution coefficient over the solidification range are significant. With the variable partition coefficient (k from 0.34 to 0.25 for niobium), this model has predicted an increased segregation behavior toward the end of solidification. Different cladding conditions have produced a different dilution and a slightly different solidification geometry (dendrite arm spacing). In the normalized modeling unit (=1), the model demonstrated a similar segregation behavior of niobium at the same dilution level (same initial niobium concentration, different dendrite arm spacing). Kobayashi also concluded that the solidification geometry is unimportant for quantifying the microsegregation effects.[51] However, for the same predicted (solid/liquid) area fraction, large dendrite arm spacing means large size of the interdendritic constituents. Higher niobium initial concentration resulted from lower dilution leads to the production of more interdendritic constituents. Heat input is the greatest factor affecting the interdendritic constituents

because of its influence on the dilution level and dendrite arm spacing. High heat input normally means lower dilution and larger dendrite arm spacing.

The assumption of complete diffusion of solute in the liquid is adopted especially in the case of ESS due to the following reasons:

- relatively high diffusivity ($D_L = 1x10^{-9}$ m^2/s);
- short diffusion distances ($\lambda/2 = 50\mu m$);
- long diffusion time; and
- strong welding convection.

Further proof is obtained by calculating dendrite tip undercooling (ΔT_{tip}) which can be derived by consideration of a simplified solute diffusion description within the interdendritic liquid.[131] This yields the dendrite tip temperature T_t as follows:

$$T_t = T_m + mC_0(1-a) \qquad [5.1]$$

where

$$a = \frac{D_L G}{mVC_0} \qquad [5.2]$$

$$\therefore \qquad \Delta T_{tip} = -\frac{D_L G}{V} = -\frac{D_L(GV)}{V^2} \qquad [5.3]$$

D_L is the solute diffusion coefficient in the liquid alloy (1 x 10^{-9} m^2/s), m is the liquidus slope, G is the temperature gradient, V is the growth rate (2.6 x 10^{-4} m/s) or GV is the cooling rate (GV=3.57 °C/s), and C_0 is the alloy average composition. In the ESS process, the estimated undercooling ΔT_{tip} is about -0.05 °C without considering the convection in liquid. This indicates that the dendrite tip undercooling due to solute buildup at the solidification front is negligible.

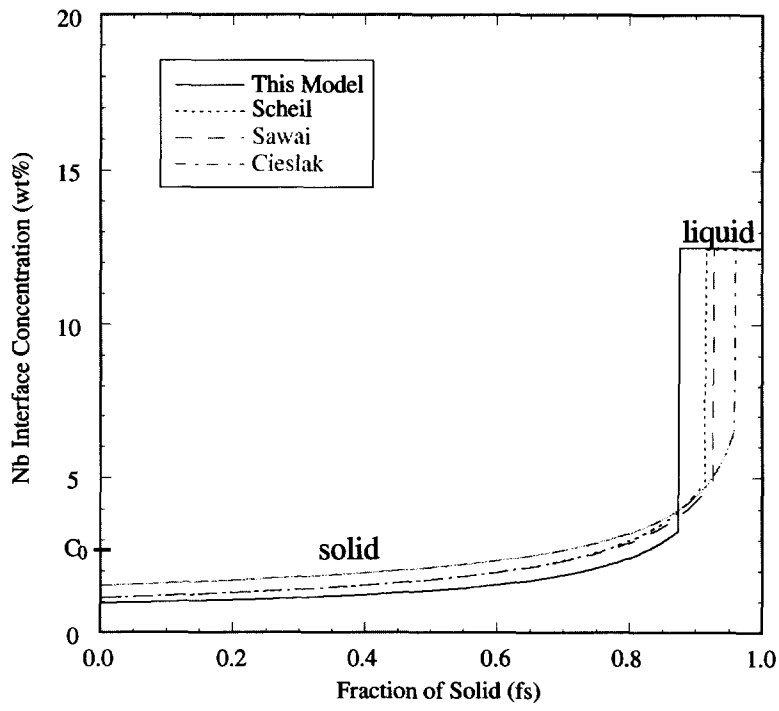

Figure 5.6 Comparison of the Current Model with Scheil, Sawai, and Cieslak Model for Interdendritic Liquid Fraction at Nb =12.5 wt% for solidification of nickel alloy 625.

In the above figure, the new model employs a variable partition coefficient. k is equal to 0.34 at the start of solidification and reduced to 0.25 at the end for nickel alloy 625. With the back diffusion in the solid incorporated in this model, it predicts the largest liquid fraction (12.5% @ C_{LNb}=12.5 wt%) among those models. The value of partition coefficient k = 0.4 was used in Sawai's model[127], in which back diffusion was also incorporated. It predicted slightly less liquid fraction (7.25%) than the comparable Scheil's model (8.5% liquid fraction at k = 0.4, with no diffusion in the solid). It is seen that solid diffusion of niobium becomes substantial when the solid C_0 is exceeded. Cieslak used the Scheil equation with k = 0.54 taken from binary phase diagram and

predicted the smallest liquid fraction (4%) when niobium concentration in the liquid was reached 12.5 wt%. From the experimental data, we know that the correct liquid fraction is 12.6%. The current model predicts the strongest segregation behavior of niobium as compared to other models. All the other models have underestimated the liquid fraction except the proposed new model. The difference in the niobium redistribution in the solid is mainly due to the differences in partition coefficient among those models.

The extent of niobium diffusion in the solid is limited due to the large size of the niobium atom. It is believed that back diffusion plays an important role in the microsegregation during solidification, particularly for the interstitial elements. However, such an effect on niobium is very limited due to small diffusion coefficient and lack of diffusion time in the ESS process.

The model has effectively predicted the volume fraction of niobium-rich interdendritic liquid distributed in the interdendritic region of nickel alloy 625 cladding. The volume fraction of the interdendritic liquid directly affects the final solidification products such as Laves phase and carbides. It is known that they form at different temperatures. However, the quantitative relationship regarding to formation of Laves phase and carbides is still not properly understood. As a result, this model can not calculate the amount of Laves phase directly, since the Laves phase is not the only product that the interdendritic liquid produces as it solidifies. It is also believed that any attempt to quantitatively predict Laves phase from solidification model would have to precisely solve quantitative relationship between Laves phase and carbides. Rapid liquid diffusion is expected at the terminal stage of the solidification. The continuous network of interdendritic liquid breaks off and forms the interdendritic eutectic constituents, mainly discontinuous Laves phase and MC carbides.

Solidification Parameters Estimation

Because most grains in the clad metal are straight and grow perpendicularly to the substrate, the average solidification time at the center of the cladding could be roughly estimated by Eq. [4.2].

$$Solidification\ Time\ (sec) = \frac{60\ \text{x}\ Pool\ Length\ (mm)}{Travel\ Speed\ (mm/min.)} \qquad [4.2]$$

For a typical cladding conditions, the center pool length is about 53 mm (2.1") and the travel speed is 152 mm/min. (6 ipm) and they give the average freezing time about 21 seconds for the cladding.

The average solidification time of ESS surfacing can be obtained by measuring the dendrite arm spacing of the dendritic structure and using Heubner's correlation. It can also be roughly estimated through the cladding pool size (Eq. 4.2) and that gives an easy access to estimate the dendrite arm spacing in different cladding conditions.

WELD METAL SOLIDIFICATION CRACKING

The tear-drop-like feature in the upper areas of the solidification cracking (Zone 1 described in Figure 4.33) has clearly indicated the presence of liquid metal when cracking takes place. Dendrites completely surrounded by the liquid film network can also be seen in the interface-quenched samples as shown in Figure 4.16. However, at this stage, when the solid is completely surrounded by a thin liquid film, there is no stress built up in this area and therefore cracking can not initiate in this region. On the other hand, it also offers little resistance to cracking if the cracking initiates elsewhere.

The fracture in the cracking test is caused by the thermal expansion of the test piece and the contraction of the cladding. When the cracking driving force exceeds the resistance to the cracking, the cracking initiates from the bottom of the cladding and propagates to the top of the cladding. The amount of low-melting interdendritic liquid directly accounts for the solidification cracking resistance in the nickel alloy 625 cladding. The grooves in zone 2 are solidified primary dendrites with the low melting eutectic constituents distributed in the interdendritic region.

CHAPTER VI

CONCLUSIONS

The goals of this work have been (1) to contribute to the understanding of the fundamental aspects of electroslag surfacing (ESS) process using strip electrodes regarding weld pool formation and weld metal solidification mechanism, (2) to develop a model to predict solute redistribution during weld metal solidification, and (3) to assess the weld metal solidification cracking susceptibility of strip cladding of engineering alloys such as nickel alloy 625. Different combinations of strip electrodes including: (a) nickel alloys 625, 59, 200, and 70/30 NiCu; (b) stainless steels 304, 308L, and 410; and (c) 70/30 CuNi and base metals including: MIL-S-23284, Class 1 steel as well as 304 and 316 stainless steels have been investigated. Based on the results of this study, the following conclusions can be drawn.

A unique microstructural morphology of cladding deposited by ESS is characterized by vertically oriented grains and dendrites. Unlike traditional weld metal deposited by GMAW, SAW, and other arc welding processes, grain orientation is vertically unidirectional because the temperature gradient during solidification is essentially vertical at the early stage. Weld metal solidification initiates epitaxially from the base metal to the unmixed zone and grains and dendrites grow competitively into the composite zone. The width of the unmixed zone during high heat input ESS is not affected by the melting temperature differences between filler metal and base metal. The

unmixed zone disappears when the filler metal and base metal have the same composition. Renucleation may occur near the interface between the unmixed zone and the composite zone when the grains in the unmixed zone have an unfavorable growth direction particularly in dissimilar metal cladding. The formation of type B grain boundaries can only occur in dissimilar metal cladding when renucleation occurs. Thus, because the weld pool size is large and the solid/liquid interface moves vertical-up, the resulting microstructure is uniquely characterized by grains and dendrites which are virtually all parallel to the vertical axis.

A new solidification model successfully predicts the redistribution of alloying elements such as niobium in the ESS of class 1 steel with nickel alloy 625 strip. A high level of agreement between the model prediction and experimental data on the liquid area fractions is achieved. The significant improvement in the accuracy of the model is primarily attributed to the successful application of a variable partition coefficient which allows accelerated segregation behavior of niobium between dendrites. Back diffusion has only a limited effect on niobium redistribution during the early stages of dendrite formation but is accelerated during the late stages of solidification.

Interface-quenching experiments provides a means to "freeze" different steps in the solidification of cladding deposited by ESS and thereby verifying the solidification model. The sequence of Laves phase and MC carbides formation in nickel alloy 625 involves the formation of a continuous interdendritic liquid film network from which a discontinuous precipitates of Laves phase and MC carbides form.

The solidification cracking resistance of nickel alloy 625 cladding deposited on steel is related to the presence of the low-melting interdendritic liquid which weakens the

weld metal resistance to the cracking. A new solidification cracking test has been developed and successfully applied in the strip surfacing process without producing an altered microstructure to the actual cladding.

REFERENCES

1. Seidel, G. and H. Hess, "Investigation of the Electroslag Strip Cladding with Strip Electrodes," *Schweissen und Schneiden*, 23 (10), 410-411 (1971).

2. Nakano, S., T. Hiro, N. Nishiyama and J. Tsuboi, "The New Strip Electroslag Overlay Technique with Electro-magnetic Control - the MAGLAY -," *Kawasaki Steel Technical Report*, 2 (3), 31-42 (1981).

3. Nakano, S., N. Nishiyama, A. Kamada and J. Tsuboi, "MAGLAY - an Electroslag Technique for Overlay Welding," *Metal Construction*, 14 (11), 610-614 (1982).

4. Barger, J.J., "Weld Overlays," : *Welding Technology in Japan*, pp.16-22, Welding Research Council, New York, NY, (1982).

5. Bemst, A.V. and Ph. Dargent, "Electroslag Cladding Using Nickel Base Alloys," *Metal Construction*, (12), 730-733 (1983).

6. Masumoto, I., Electroslag Overlay Welding with Strip Electrode and Present Status of the Application to Japanese Industries, IIW, (1985).

7. Hoffmann, T. and G. Rudolph, "Overlay Welding of Nickel and its Alloy," *Welding and Metal Fabrication*, (8/9), 281-282 (1986).

8. Killing, R. and D. Bohme, "Performance Characteristics of Electroslag Welding Cladding With Strip Electrodes," *Schweissen und Schneiden*, 40 (6), 283(E91)-288(E94) (1988).

9. Killing, R., "Influences of Welding Powder and Welding Parameters on the Welding Process in Electroslag Strip Cladding with Strip Electrodes," *Schweissen und Schneiden*, 10, E159-E162 (1988).

10. Demuzere, R. and W. Pors, "Strip Cladding of Corrosion-Resistant Layers. II," *Roestvast Staal*, April (2), 23-31 (1989).

11. Yu, D.W. and J.H. Devletian, "Electroslag Surfacing: A Potential Process for the Rebuilding and Restoration of Ship Components," *Journal of Ship Production*, 5 (2), 67-78 (1989).

12. Murray, C. and A. Burley, "Electro-slag Strip Cladding of Tubeplates," *Welding and Metal Fabrication*, (11), 468-469 (1989).

13. Oh, Y.K., J.H. Devletian and S.J. Chen, "Low Dilution Electroslag Cladding for Shipbuilding," *Welding Journal*, 68(8), 37-44 (1990).

14. Oh, Y.K. and J.H. Devletian, "Electroslag Surfacing for Shipbuilding and Repair," *Sea Technology*, (6), 46-47 (1990).

15. Blaskovic, P. and S. Lesnak, "Electroslag Surfacing with a Double Strip Electrode in the Horizontal Position," *Welding International*, 4 (3), 238-240 (1990).

16. Irving, B., "Pressure Vessel Fabrication Makes a Comeback in the U.S," *Welding Journal*, 70 (12), 51-54 (1991).

17. Devletian, J.H., Y.P. Gao, Q.H. Zhao and W.E. Wood, "Strip Cladding of Main Propeller Shafting with Ni Alloy 625 by Electroslag Surfacing," : *1992 Ship Production Symposium*, pp.7C2-1-7C2-11, The Society of Naval Architects and Marine Engineers, New Orleans, LA, (1992).

18. Gao, Y.P., J.H. Devletian and W.E. Wood, "Electroslag and Submerged Arc Cladding with Nickel Alloy Strip," : *3rd TWR Conference Proceedings*, David, S.A., ed.,ASM International, Materials Park, OH, (1993).

19. Devletian, J.H., Y.P. Gao, Q.H. Zhao and W.E. Wood, "Strip Cladding of Propeller Shafts with Ni Alloy 625 by Electroslag Surfacing," *Journal of Ship Production*, 9 (3), 173-180 (1993).

20. Heuser, H., "Electroslag Strip Cladding," *Thyssen Welding Technical Information*, (1993).

21. Lucas, W., "Arc Surfacing and Cladding Processes," *Welding and Metal Fabrication*, (2), 55-62 (1994).

22. Demuzere, R., *Submerged Arc and Electroslag Strip Cladding - A Review -*, Soudometal, Brussels (1994).

23. Inco Alloys International, *Electroslag Welding Flux*, Inco Alloys International, Huntington, WV (1994).

24. Gilliand, R.G. and G.M. Slaughter, "The Welding of New Solution-Strengthened Nickel-Base Alloys," *Welding Journal*, 45 (7), 314s-320s (1966).

25. Eiselstein, H.L. and D.J. Tillack, "The Invention and Definition of Alloy 625," : *Superalloys 718, 625 and Various Derivatives*, pp.1-14, Loria, E.A., ed.,The Mineral, Metals and Materials Society, (1991).

26. Inco Alloys International, *INCONEL alloy 625*, Inco Alloys International, Huntington, WV (1985).

27. Hasson, D.F., C. Zanis, L. Aprigliano and C. Fraser, "Corrosion and Corrosion-Fatigue Behavior of IN625 Weld Surfaced 3.25 Nickel Steel," : *Proceedings of Corrosion of Nickel-Base Alloys*, pp.135-146, Scarberry, R.C., ed.,ASM, Metals Park, OH, (1985).

28. Krupp VDM, *High-Performance Materials*, Krupp VDM Publication No. N524 92-11, Werdohl, FRG (1992).

29. Wilson, I.L.W., R.G. Gourley, R.M. Walkosak and G.J. Bruck, "The Effect of Heat Input on Microstructure and Cracking in Alloy 625 Weld Overlays," : *Superalloys 718, 625 and Various Derivatives*, pp.735-746, Loria, E.A., ed.,The Mineral, Metals and Materials Society, Pittsburgh, PA, (1991).

30. Patterson, R.A. and J.O. Milewski, "GTA Welding Cracking - Alloy 625 to 304L," *Welding Journal*, 64 (8), 227s-231s (1985).

31. White, T.H. and R.V.V. Davis, "Weld Overlaying for Marine Corrosion Resistance," *Welding and Metal Fabrication*, 46 (6), 353-356 (1978).

32. Hasson, D.F., C. Zanis, L. Aprigliano and C. Fraser, "Surfacing of 3.25% Nickel Steel with Inconel 625 by the Gas Metal Arc Welding-Pulsed arc Process," *Welding Journal*, 57 (1), 1s-8s (1978).

33. Dimbylow, C.S., "Bead Geometry and Properties of Inconel 625 Overlays on Steel," *Metal Construction*, 17 (1), 35-39 (1985).

34. "Effect of Iron on the Performance of IN625 Weld Deposits," *Government Report Announcement*, 85 (11), 129-155 (1985).

35. Superalloy 718, 625 and Various Derivatives, The Minerals, Metals & Materials Society, Pittsburgh, Pennsylvania (1989).

36. Zhao, Q.H., Y.P. Gao, J.H. Devletian, J. McCarthy and W.E. Wood, "Microstructural Analysis of Ni Alloy 625 Cladding over Carbon Steel," : *3rd TWR Conference Proceedings*, David, S.A., ed.,ASM International, Materials Park, OH, (1993).

37. Savage, W.F., C.D. Lundin and A.H. Aronson, "Weld Metal Solidification Mechanics," *Welding Journal*, 44 (4), 175s-181s (1965).

38. Savage, W.F. and A.H. Aronson, "Preferred Orientation in the Welding Fusion Zone," *Welding Journal*, 45 (2), 85s-89s (1966).

39. Savage, W.F., C.D. Lundin and T.F. Chase, "Solidification Mechanics of Fusion Welds in Face-Centered Cubic Metals," *Welding Journal*, 47(11), 522s-526s (1968).

40. Savage, W.F., C.D. Lundin and T.F. Chase, "Technical Note: Direct Observation of Microstructural Changes Associated with Fusion Welding," *Welding Journal*, 47 (11), 527s-528s (1968).

41. Loper JR., C.R., L.A. Shideler and J.H. Devletian, "The Effect of Heat-Affected Zone structure on the Structure of the Weld Fusion Zone," *Welding Journal*, 48 (4), 171s-178s (1969).

42. Devletian, J.H. and W.E. Wood, "Principles of Joining Metallurgy," : *Metals Handbook*, Ed. 9, pp.21-49, ASM, (1982).

43. Devletian, J.H. and W.E. Wood, Paper presented at the 66th Annual AWS Convention, Las Vegas, NV, (1985).

44. Venkataraman, S. and J.H. Devletian, "Rapid Solidification of Stainless Steel by Capacitor Discharge Welding," *Welding Journal*, 67 (6), 111s-118s (1988).

45. Owczarski, W.A., D.S. Duvall and C.P. Sullivan, "A Model for Heat Affected Zone Cracking in Nickel Base Superalloys," *Welding Journal*, 45 (4), 145s-155s (1966).

46. Matsuda, F., H. Nakagawa and J.B. Lee, "Weld Cracking in Duplex Stainless Steel (Report II) - Modeling of Cellular Dendritic Growth during Weld Solidification -," *Transactions of Japan Welding Research Institute*, 18 (1), 107-117 (1989).

47. Brooks, J.A. and M.I. Baskes, "Weld Microsegregation Characterization and Modeling," : *Advances in Welding Science and Technology*, pp.93-99, David, S.A., ed.,ASM International, Metals Park, OH, (1986).

48. Wang, C.Y. and C. Beckermann, "A Multiphase Solute Diffusion Model for Dendritic Alloy Solidification," *Metallurgical Transactions A*, 24A (12), 2787-2802 (1993).

49. Nastac, L. and D.M. Stefanscu, "An Analytical Model for Solute Redistribution during Solidification of Planar, Columnar, or Equiaxed Morphology," *Metallurgical Transactions A*, 24A (9), 2107-2118 (1993).

50. Sharp, R.M. and M.C. Flemings, "Solute Redistribution in Cellular Solidification," *Metallurgical Transactions*, 5 (4), 823-830 (1974).

51. Kobayashi, S., "Mathematical Analysis of Solute Redistribution during Solidification Based on a Columnar Dendrite Model," *Transactions of The Iron and Steel Institute of Japan*, 28 (9), 728-735 (1988).

52. Swaminathan, C.R. and V.R. Voller, "A General Enthalpy Method for Modeling Solidification Processes," *Metallurgical Transactions B*, 23B (10), 651-664 (1992).

53. Ohnaka, I., "Mathematical Analysis of Solute Redistribution during Solidification with Diffusion in Solid Phase," *Transactions of The Iron and Steel Institute of Japan*, 26, 1045-1051 (1986).

54. David, S.A. and J.M. Vitek, "Correlation between Solidification Parameters and Weld Microstructures," *International Materials Reviews*, 34 (5), 213-245 (1989).

55. Battle, T.P., "Mathematical Modeling of Solute Segregation in Solidification Materials," *International Materials Reviews*, 37 (6), 249-270 (1992).

56. Wilken, K. and H. Kleistner, "The Classification and Evaluation of Hot Cracking Tests for Weldments," *Welding in the World*, 28 (7/8), 37-48 (1990).

57. Goodwin, G.M., "Test Methods for Evaluating Hot Cracking," : *First United States - Japan Symposium on Advances in Welding Metallurgy*, pp.59-78, AWS, San Francisco, USA. and Yokohama, Japan., (1990).

58. Brill, U., T. Hoffmann and K. Wilken, "Solidification Cracking: Super Stainless Steel and Nickel-Base Alloys," : *Weldability of Materials*, pp.99-105, Patterson, R.A. and K.W. Mahin, ed., ASM International, Materials Park, OH, (1990).

59. Rawlings, G.N. and K. Wilken, "Comparing the Effectiveness of New Hot Cracking Test Methods," *Schweissen und Schneiden*, 4, E75-E78 (1992).

60. Almqvist, G. and N. Egeman, "Stainless Steel Cladding with Strip Electrodes," *Welding and Metal Fabrication*, 31, 294-302 (1963).

61. Almqvist, G. and N. Egeman, "Nickel Cladding with Strip Electrodes," *Welding Journal*, 45 (4), 275-283 (1966).

62. Thomas Jr., R.D., "Corrosion-resistant Weld Overlays by the Dual-strip Process," *British Welding Journal*, (5), 307-314 (1966).

63. Campbell, H.C. and W.C. Johnson, "Cladding and Overlay Welding with Strip Electrodes," *Welding Journal*, 45 (5), 399-409 (1966).

64. Engindeniz, E., H. Barth and E. Scholz, "Submerged-arc Surface Welding with Flux-cored Strip Electrodes," *Schweissen und Schneiden*, 8, E122-E123 (1987).

65. Kalvala, P. and R.P. Krishnan, "Submerged-arc Strip Cladding - A Study on the Effects of Fluxes and Welding Parameters," *Schweissen und Schneiden*, 7, E106-E109 (1988).

66. Hobart Brothers Co., *Technical Guide for Electroslag Welding*, (1980).

67. Forsberg, S.G., "Resistance Electroslag (RES) Surfacing," *Welding Journal*, 64 (8), 41-48 (1985).

68. Hoffmann, T., "Welding of Nickel Alloys and High Alloy Special Stainless Steels," : *Nickel Alloys and High Alloy Special Stainless Steels*, pp.95-105, Expert Verlag, Sindelfingen, (1987).

69. Devletian, J.H., A. Koch and E.N. Buckley, "Unique Application Initiates the Introduction of Electroslag Cladding to U.S. Industry," *Welding Journal*, 71(1), 57-60 (1992).

70. Oh, Y.K. and J.H. Devletian, "Electroslag Strip Cladding of Stainless Steel with Metal Powder Additions," *Welding Journal*, 71(1), 37-44 (1992).

71. Gao, Y.P., J.H. Devletian and W.E. Wood, "Electroslag and Submerged Arc Cladding Ni Alloy 625," *73th Annual AWS Convention, Chicago, Il.'92*, (1992).

72. Steffens, H.D., E.R. Sievers and J. Blum, "Preliminary Experiments on Electroslag Weld Hardfacing of Small Diameter Shafts Using Strip Electrodes," *Schweissen und Schneiden*, 2, E26-E27 (1989).

73. Kompan, Y.Y., "Unique Electrode Designed for Electroslag Surfacing," *Welding International*, 8 (12), 986-988 (1994).

74. Superalloys Source Book, ASM, Metals Park, OH (1984).

75. Superalloys 718, 625 and Various Derivatives, The Minerals, Metals & Materials Society, Warrendale, PA (1991).

76. Lukens Steel, *Lukens Roll-Bonded Clad Steels*, Lukens Steel, Coatesville, PA 19320 (1994).

77. Wilhelm, S.M., R.D. Kane, S. Matsui, T. Yoshida and T. Iwase, "Evaluation of Alloy 625 Steel Bimetallic Pipe for Petroleum Service," : *Superalloys 718, 625 and Various Derivatives*, pp.771-791, Loria, E.A., ed.,The Minerals, Metals & Materials Society, Warrendale, PA, (1991).

78. Fukuda, T., Y. Ohashi, M. Nakanishi, M. Nishiguchi, M. Ueda, S. Azuma and J. Kikuchi, "Development of a Production Technique for P/M Alloy 625 Clad Low Alloy Steel Pipe," : *Superalloys 718, 625 and Various Derivatives*, pp.793-802, Loria, E.A., ed.,The Minerals, Metals & Materials Society, Warrendale, PA, (1991).

79. Rodgers, K.J. and E.R. Macleod, "Applications of Electroslag Cladding," : *First International Conference on Surface Engineering*, pp.23-37, Bucklow, I.A., ed.,The Welding Institute, Abington, UK, (1986).

80. Nugent, R.M., "Alloy 625 Surfacing of Tool and Die Steels," *Welding Journal*, 65 (6), 33s-39s (1986).

81. Kohler, M., "Effect of the Elevated-Temperature-Precipitation in Alloy 625 0n Properties and Microstructure," : *Superalloys 718, 625 and Various Derivatives*, pp.363-374, Loria, E.A., ed.,The Minerals, Metals & Materials Society, Warrendale, PA, (1991).

82. Ferrer, L., B. Pieraggi and J.F. Uginet, "Microstructural Evolution during Thermomechnical Processing of Alloy 625," : *Superalloy 718, 625 and Various Derivatives*, pp.217-228, Loria, E.A., ed.,TMS, Warrendale, PA, (1991).

83. Rizzo, F.J. and J.F. Radavich, "Microstructural Characterization of PM 625-Type Materials," : *Superalloy 718, 625 and Various Derivatives*, pp.297-308, Loria, E.A., ed.,TMS, Warrendale, PA, (1991).

84. Davidson, J.H., "The Influence of Processing Variables on the Microstructure and Properties of PM 625 Alloy," : *Superalloy 718, 625 and Various Derivatives*, pp.229-239, Loria, E.A., ed.,TMS, Warrendale, PA, (1991).

85. Conaway, H.R. and J.H. Mesick, "A Report on New Matrix-stiffened Ni-Cr Welding Products," *Welding Journal*, 49 (2), 27s-32s (1970).

86. Arata, Y., K. Terai, H. Nagai, S. Shimizu and T. Aota, "Fundamental Studies on Electron Beam Welding of Heat-resistant Superalloys for Nuclear Plants (Report II) - Correlation between Susceptibility to Weld Cracking and Characteristics in Hot Ductility and Trans-Varestraint Test," *Transactions of Japan Welding Research Institute*, 6 (1), 69-79 (1977).

87. Cieslak, M.J., "The Welding and Solidification Metallurgy of Alloy 625," *Welding Journal*, 70 (2), 49s-56s (1991).

88. Slaughter, G.M., E.A. Franco-Ferreira, E.L. Long Jr. and G. Hallerman, "Technical Note: Unusual Weld Cracking Problem in Inconel," *Welding Journal*, 47 (10), 479s-480s (1968).

89. Lingenfelter, A.C., "Varestraint Testing of Nickel Alloys," *Welding Journal*, 51 (9), 430s-436s (1972).

90. Cieslak, M.J., G.A. Knorovsky, T.J. Headley and A.D. Romig Jr, "The Use of New PHACOMP in Understanding the Solidification Microstructure of Nickel Base Alloy Weld Metal," *Metallurgical Transactions A*, 17(A) (12), 2107-2116 (1986).

91. Cieslak, M.J., T.J. Headley, T. Kollie and A.D. Romig Jr, "A Melting and Solidification Study of Alloy 625," *Metallurgical Transactions A*, 19(A) (9), 2319-2331 (1988).

92. Cieslak, M.J., T.J. Headley and R.B. Frank, "The Welding Metallurgy of Custom Age 625 PLUS Alloy," *Welding Journal*, 68 (12), 473s-482s (1989).

93. Cieslak, M.J., G.A. Knorovsky, T.J. Headley and A.D. Romig Jr, "The Solidification Metallurgy of Alloy 718 and Other Niobium-Containing Superalloys," : *Superalloy 718: Metallurgy and Applications*, (1989).

94. Cieslak, M.J., "The Solidification Behavior of an Alloy 625/718 Variant," : *Superalloys 718, 625 and Various Derivatives*, pp.71-80, Loria, E.A., ed.,The Mineral, Metals and Materials Society, (1991).

95. Steffens, H.D. and J. Blum, "Hot Cracking Susceptibility of Electroslag Strip Electrode Cladding with NiMo16Cr16Ti," *Schweissen und Schneiden*, 12, E212-E213 (1992).

96. Wielage, B., F. Hartung and R. Boecking, "Influence of Stabilizers on the Hot Cracking Sensitivity and Corrosion Resistance of Multilayer Austenitic Submerged Arc Strip Cladding," *Schweissen und Schneiden*, 45 (1), E11-E14 (1993).

97. Cortial, F., J.M. Corrieu and C. Vernot-Loier, "Influence of Heat Treatments on Microstructure, Mechanical Properties, and Corrosion Resistance of Weld Alloy 625," *Metallurgical Transactions A*, 26A (5), 1273-1286 (1995).

98. Heubner, U., M. Kohler and B. Prinz, "Determination of the Solidification Behavior of Some Selected Superalloys," : *Superalloys 1988*, pp.437-448, Duhl, D.N., G. Maurer, S. Antolovich, C. Lund and S. Reichman, ed., The Metallurgical Society, (1988).

99. Matthews, S.J. and W.F. Savage, "Heat-Affected Zone Infiltration by Dissimilar Liquid Weld Metal," *Welding Journal*, 50 (4), 174s-182s (1971).

100. Savage, W.F., E.F. Nippes and E.S. Szekeres, "A Study of Weld Interface Phenomena in a Low Alloy Steel," *Welding Journal*, 55 (9), 260s-268s (1976).

101. Lukkari, J. and T. Moisio, "The Effect of the Welding Method on the Unmixed Zone of the Weld," : *Microstructural Science Volume 7*, pp.333-344, May, I.L., P.A. Fallon and J.L. McCall, ed., Elsevier North Holland, Inc., New York, NY, (1979).

102. Savage, W.F., "Solidification, Segregation and Weld Imperfections," *Welding in the World*, 18 (5/6), 89-114 (1980).

103. Lundin, C.D., W. Liu, C.Y.P. Qiao and K.K. Khan, "Unmixed Zone in Arc Welds - Significance in Corrosion Resistance and Mechanical Properties," *Welding Research Council - Progress Reports*, L (3/4), 64-87 (1995).

104. Chalmers, B., Principles of Solidification, John Wiley & Sons, Inc., New York (1967).

105. Loper JR., C.R. and J.T. Gregory, "Microstructural Aspects of Weld Metal Solidification in Large Grain Aluminum," *Welding Journal*, 53 (3), 126s-133s (1974).

106. Easterling, K., Introduction to the Physical Metallurgy of Welding, Butterworths, London (1983).

107. Kou, S. and Y. Le, "Nucleation Mechanisms and Grain Refining of Weld Metal," *Welding Journal*, 65 (12), 305s-313s (1986).

108. Le, Y. and S. Kou, "Formation of Three Types of New Grains in the Weld Metal," : *Recent Trends in Welding Science and Technology*, pp.139-144, David, S.A., ed.,ASM International, Metals Park, OH, (1986).

109. Kou, S., Welding Metallurgy, John Wiley & Sons, Inc., (1987).

110. Kou, S., "Grain Structure Development in the Fusion Zone," : *Recent Trends in Welding Science and Technology*, pp.137-146, David, S.A. and J.M. Vitek, ed., ASM International, Materials Park, OH, (1989).

111. Kou, S. and Y. Le, "Welding Parameters and the Grain Structure of Weld Metal - A Thermodynamic Consideration," *Metallurgical Transactions A*, 19A (4), 1075-1082 (1988).

112. Loper JR., C.R. and J.T. Gregory, "Non-epitaxial Growth in Weld Metal," : *Solidification and Casting of Metals*, pp.433-437, The Metals Society, London, (1979).

113. Matsuda, F. and H. Nakagawa, "Simulation Test of Disbonding between $2^1/_4$Cr-1Mo Steel and Overlaid Austenitic Stainless Steel by Electrolytic Hydrogen Charging Technique," *Transactions of Japan Welding Research Institute*, 13 (1), 159-161 (1984).

114. Baikie, B.L. and D. Yapp, "Oriented Structures and Properties in type 316 Stainless-Steel Weld Metal," : *Solidification and Casting of Metals*, pp.438-443, The Metals Society, London, (1979).

115. Laridjani, M., P. Ramachandrarao and R.W. Cahn, "Metastable Phase Formation in a Laser-irradiated Silver-germanium Alloy," *Journal of Materials Science*, 7(6), 627-630 (1972).

116. Yatsuya, S. and T.B. Massalski, "Laser Beam Interaction with the Pd-Si-Cu Eutectic," *Materials Science and Engineering*, 65, 101-111 (1982).

117. Brooks, J.A. and K.W. Mahin, "Solidification and Structure of Welds," : *Welding Theory and Practice*, pp.35-78, Olson, D.L., R. Dixon and A.L. Liby, ed., Elsevier Science Publishing Company, Inc., Amsterdam, Netherlands, (1990).

118. Marcellin, W.J. and P.R. Landon, "Technical Note: Cause of Cracking in Thorium During Fusion Welding," *Welding Journal*, 47 (12), 575s-576s (1968).

119. Davies, G.J. and J.G. Garland, "Solidification Structures and Properties of Fusion Welds," *International Metals Reviews*, 20, 83-106 (1975).

120. Savage, W.F. and R.J. Hrubec, "Synthesis of Weld Solidification using Crystalline Organic Materials," *Welding Journal*, 51 (5), 260s-271s (1972).

121. Venkataraman, S., W.E. Wood, D.G. Atteridge and J.H. Devletian, "Grain Refinement in Electroslag Welds," pp.381-397, (1982).

122. Matsuda, F., K. Nakata, Y. Shimokusu, K. Tsukamoto and K. Arai, "Effect of Additional Element on Weld Solidification Crack Susceptibility of Al-Zn-Mg Alloy (Report I) - Results of Ring Casting Cracking Test -," *Transactions of Japan Welding Research Institute*, 12 (1), 81-87 (1983).

123. Stout, R.D., T.E. Tozok and P.P. Podgurski, "Tensile Properties of High Purity Iron Base Weld Metals," *Welding Journal*, 42 (9), 385s-391s (1963).

124. Baird, B.L., "Biaxial Stress Strain Properties of Welds in High Strength Alloys," *Welding Journal*, 42 (12), 571s-576s (1963).

125. Savage, W.F., E.F. Nippes and J.S. Erickson, "Solidification Mechanisms in Fusion Welds," *Welding Journal*, 65 (8), 213s-221s (1976).

126. Savage, W.F., C.D. Lundin and R.J. Hrubec, "Segregation and Hot Cracking in Low-Alloy Quench and Tempered Steels," *Welding Journal*, 47 (9), 420s-425s (1968).

127. Sawai, T., Y. Ueshima and S. Mizoguchi, "Microsegregation and Precipitation Behavior during Solidification in a Nickel-base Superalloy," *ISIJ International*, 30 (7), 520-528 (1990).

128. Cieslak, M.J., T.J. Headley and A.D. Romig, "Transformations and New PHACOMP Analysis in Weld Metal of Hastelloy C-Type Alloys," : *Advances in Welding Science and Technology*, pp.119-125, David, S.A., ed.,ASM International, (1986).

129. Flemings, M.C., Solidification Processing, McGRAW-HALL, (1974).

130. Brody, H.D. and M.C. Flemings, "Solute Redistribution in Dendritic Solidification," *Transactions of AIME*, 236 (5), 615-624 (1966).

131. Bower, T.F., H.D. Brody and M.C. Flemings, "Measurements of Solute Redistribution in Dendritic Solidification," *Transactions of AIME*, 236 (5), 624-634 (1966).

132. Clyne, T.W. and W. Kurz, "Solute Redistribution During Solidification with Rapid Solid State Diffusion," *Metallurgical Transactions A*, 12A, (6), 965-971 (1981).

133. Kobayashi, S., "A Mathematical Model for Solute Redistribution during Dendritic Solidification," *Transactions of The Iron and Steel Institute of Japan*, 28 (7), 535-542 (1988).

134. Matsumiya, T., H. Kajioka, S. Mizoguchi, Y. Ueshima and H. Esaka, "Mathematical Analysis of Segregation in Continuously Cast Slabs," *Transactions of The Iron and Steel Institute of Japan*, 24 (11), 873-882 (1984).

135. Sarreal, J.A. and G.J. Abbaschian, "The Effect of Solidification Rate on Microsegregation," *Metallurgical Transactions A*, 17A (11), 2063-2073 (1986).

136. Giovanola, B. and W. Kurz, "Modeling of Microsegregation under Rapid Solidification Conditions," *Metallurgical Transactions A*, 21A (1), 260-263 (1990).

137. Giovanola, B. and W. Kurz, "Microsegregation under Rapid Solidification Conditions with Solid State Diffusion," *Zeitschrift fur Metallkunde*, 82 (2), 83-88 (1991).

138. Borland, J.C., "Generalized Theory of Super-Solidus Cracking in Welds (and Castings)," *British Welding Journal*, (8), 508-512 (1960).

139. Babiak, Z., "Stress and Deformations during Surfacing," *The Surfacing Journal*, 16 (4), 114-119 (1985).

140. Pellini, W.S., "Strain Theory of Hot Tearing," *Foundry*, (11), 125-199 (1952).

141. Apblett, W.R. and W.S. Pellini, "Factors which Influence Weld Hot Cracking," *Welding Journal*, 33 (2), 83s-90s (1954).

142. Borland, J.C. and R.N. Younger, "Some Aspects of Cracking in Welded Cr-Ni Austenitic Steels," *British Welding Journal*, (1), 22-59 (1960).

143. Borland, J.C., "Suggested Explanation of Hot Cracking in Mild and Low Alloy Steel Welds," *British Welding Journal*, (11), 526-540 (1961).

144. Masubuchi, K. and D.C. Martin, "Mechanisms of Cracking in HY-80 Steel Weldments," *Welding Journal*, 41 (8), 375s-384s (1962).

145. Williams, J.A. and A.R.E. Singer, "A Review of the Mechanisms of Hot Short Cracking," *Journal of the Australian Institute of Metals*, 11 (2), 2-9 (1966).

146. Savage, W.F., "Solidification, Segregation and Weld Defects," : *Weldments: Physical Metallurgy and Failure Phenomena*, pp.1-18, Christoffel, R.J., E.F. Nippes and H.D. Solomon, ed., General Electric Company, Schenectady, NY, (1978).

147. Zacharia, T. and D.K. Aidun, "Hot-Cracking Mechanisms in Binary Alloys," *Welding Research Council*, XLII (9/10), 29-41 (1987).

148. Matsuda, F., "Hot Cracking Susceptibility of Weld Metal," : *First United States-Japan Symposium on Advances in Welding Metallurgy*, pp.26-58, ASM International, (1990).

149. Thompson, E.G., "Hot Cracking Studies of Alloy 718 Weld Heat Affected Zones," *Welding Journal*, 48 (2), 70s-79s (1969).

150. Savage, W.F., E.F. Nippes and G.M. Goodwin, "Effect of Minor Elements on Hot Cracking Tendencies of INCONEL 600," *Welding Journal*, 56 (8), 245s-252s (1977).

151. Nakagawa, H., F. Matsuda, A. Nagai and N. Sakabata, "Weldability of Fe-36%Ni Alloy (Report I) - Hot Cracking with Cross-Bead Test -," *Transactions of Japan Welding Research Institute*, 9 (2), 55-62 (1980).

152. Matsuda, F., K. Nakata and K. Sorada, "Dynamic Observation of Solidification and Solidification Cracking during Welding with Optical Microscope (I) - Solidification Front and Behavior of Cracking -," *Transactions of Japan Welding Research Institute*, 11 (2), 67-77 (1982).

153. Bohme, D. and H. Heuser, "The Influence of Welding Parameters on the Susceptibility to Solidification Cracking of Non-Alloy Submerged Arc Weld metal," *Schweissen und Schneiden*, 3, E36-E37 (1984).

154. Cieslak, M.J. and W.F. Savage, "Hot-Cracking Studies of Alloy CN-7M," *Welding Journal*, 64 (5), 119s-126s (1985).

155. Lundin, C.D., R. Menon, C.H. Lee and V. Osorio, "New Concepts in VARESTRAINT Testing for Hot Cracking," : *Welding Research: the State of the Art*, pp.33-42, Nippes, E.F. and D.J. Ball, ed., American Society for Metals, (1985).

156. Zhang, Y.C., H. Nakagawa and F. Matsuda, "Weldability of Fe-36%Ni Alloy (Report IV) -Dynamic Observation of Reheat Hot Cracking in Weld Metal by means of Hot Stage Microscope-," *Transactions of Japan Welding Research Institute*, 14 (2), 113-117 (1985).

157. Katayama, S., T. Fujimoto and A. Matsunawa, "Correlation among Solidification Process, Microstructure, Microsegregation and Solidification Cracking Susceptibility in Stainless Steel Weld Metals," *Transactions of Japan Welding Research Institute*, 14 (1), 123-138 (1985).

158. Kou, S. and Y. Le, "Grain Structure and Solidification Cracking in Oscillated Arc Welds of 5052 Aluminum Alloy," *Metallurgical Transactions A*, 16A (7), 1345-1352 (1985).

159. Kou, S. and Y. Le, "Alternating Grain Orientation and Weld Solidification Cracking," *Metallurgical Transactions A*, 16A (10), 1887-1896 (1985).

160. Karjalainen, L.P., V.P. Kujanpaa and N. Suutala, "Hot Cracking in Iron Base Alloys - Effect of Solidification Mode," : *Advances in Welding Science and Technology*, pp.145-149, David, S.A., ed.,ASM International, Metals Park, OH, (1986).

161. Cieslak, M.J., "Hot-Cracking Mechanism in CO_2 Laser Beam Welds of Dissimilar Metal Involving PH Martensitic Stainless Steels," *Welding Journal*, 66 (2), 57s-60s (1987).

162. Lundin, C.D., C.H. Lee and R. Menon, "Hot Ductility and Weldability of Free Machining Austenitic Stainless Steel," *Welding Journal*, 67 (6), 119s-130s (1988).

163. Thompson, R.G., B. Radhakrishnan and D.E. Mayo, "Grain Boundary Chemistry Contributions to Intergranular Hot Cracking," *J.Phys (France)*, 49 (10), C5.471-C5.479 (1988).

164. Dixon, B.F., "Weld Metal Solidification Cracking in Steel," : *IIW Asian Pacific Regional Welding Congress*, pp.731-751, (1988).

165. Dixon, B.F., "Weld Metal Solidification Cracking in Austenitic Stainless Steels," *Australian Welding Research*, 16, 75-83 (1988).

166. Matsuda, F., "Solidification Crack Susceptibility of Weld Metal," : *Recent Trends in Welding Science and Technology*, pp.127-136, David, S.A. and J.M. Vitek, ed., ASM International, Materials Park, OH, (1989).

167. Lundin, C.D., C.Y.P. Qiao, C.H. Lee and G.M. Goodwin, "Evaluation of Hot Cracking Susceptibility of Nuclear Grade Austenitic Stainless Steels by Four Hot Cracking test Methods," : *Recent Trends in Welding Science and Technology*, pp.699-705, David, S.A. and J.M. Vitek, ed., ASM International, Materials Park, OH, (1989).

168. Nakao, Y. and K. Shinozaki, "Hot Cracking Susceptibilities of Nickel-Base Superalloy Weld Zones," : *High Temperature Materials for Power Engineering 1990 II*, pp.1461-1470, (1990).

169. Abraham, M., M. Kutsuna and Y. Hosoi, "Effect of Alloying Elements on Hot Cracking Susceptibility of Fe-Cr-Mn Alloys," *Transactions of Japan Welding Society*, 22 (1),, 29-33 (1991).

170. Matthews, S.J. and P. Crook, "Weldability Characteristics of a New High Silicon, Nickel-based Corrosion Alloy," *74th Annual AWS Convention, Houston, TX April 25-30 '93*, (1993).(Abstract)

171. Gao, Y.P., J.H. Devletian and W.E. Wood, "Weld Metal Solidification Cracking Study on Strip Cladding," *74th Annual AWS Convention, Houston, TX April 25-30 '93*, (1993).

172. Pease, G.R., "The Practical Welding Metallurgy of Nickel and High-Ni Alloys," *Welding Journal*, 36 (7), 330s-334s (1957).

173. Duvall, D.S. and W.A. Owczarski, "Further Heat-Affected-Zone Studies in Heat-Resistant Nickel Alloys," *Welding Journal*, 46 (9), 423s-432S (1967).

174. Owczarski, W.A., "Some Minor Element Effects on Weldability of Heat Resistant Nickel Base Superalloys," : *Proceedings of the Symposium - Effects of Minor Elements on the Weldability of High-Nickel Alloys*, Ed. 6, pp.6-24, Welding Research Council, NY, (1967).

175. Matsuda, F., K. Nakata and S. Harada, "Moving Characteristics of Weld Edges during Solidification in Relation to Solidification Cracking in GTA Weld of Aluminum Alloy Thin Sheet," *Transactions of Japan Welding Research Institute*, 9 (2), 83-93 (1980).

176. Thomas Jr., R.D., "HAZ Cracking in Thick Sections of Austenitic Stainless Steels - Part II," *Welding Journal*, 63 (12), 355s-368s (1984).

177. Lippold, J.C., "Centerline Cracking in Deep Penetration Electron Beam Welds in Type 304L Stainless Steel," *Welding Journal*, 64 (5), 127s-136s (1985).

178. Brooks, J.A. and A.W. Thompson, "Microstructural Development and Solidification Cracking Susceptibility of Austenitic Stainless Steel Welds," *International Materials Reviews*, 36 (1), 16-44 (1991).

179. Thompson, R.G., J.J. Cassimus and J.R. Dobbs, "The Relationship Between Grain Size and Microfissuring in Alloy 718," *Welding Journal*, 64 (4), 91s-96s (1985).

180. Senda, T., F. Matsuda, G. Takano, K. Watanabe, T. Kobayashi and T. Matsuzaka, "Fundamental Investigations on Solidification Crack Susceptibility for Weld Metals with Trans-Varestraint Test," *Transactions of Japan Welding Society*, 2 (2), 45-66 (1971).

181. Matsuda, F. and H. Nakagawa, "Some Fractographic Features of Various Weld Cracking and Fracture Surfaces with Scanning Electron Microscope - Studies on Fractography of Welded Zone (I)," *Transactions of Japan Welding Research Institute*, 6 (1), 81-90 (1977).

182. Matsuda, F., H. Nakagawa, S. Ogata and S. Katayama, "Fractographic Investigation on Solidification Crack in the Varestraint Test of Fully Austenitic Stainless Steel - Studies on Fractography of Welded Zone (III) -," *Transactions of Japan Welding Research Institute*, 7 (1), 59-70 (1978).

183. Matsuda, F. and H. Nakagawa, "Fractographic Features and Classification of Weld Solidification Cracks," *Transactions of Japan Welding Research Institute*, 8 (1), 115-157 (1979).

184. Goodwin, G.M., "A Quantitative Test for Hot Cracking," *Metal Progress*, (2), 48-50 (1988).

185. Kurz, W. and D.J. Fisher, Fundamentals of Solidification, Trans Tech Publications, Aedermannsdorf, Switzerland (1986).

186. Grant, N.J., "Rapid Solidification of Metallic Particulates," *JOM*, 35 (1), 20-27 (1983).

187. Lienert, T.J., C.V. Robino, C.R. Hills and M.J. Cieslak, "A Welding Metallurgy Study of Hastelloy Alloys B-2 and W," : *Weldability of Materials*, pp.159-165, Patterson, R.A. and K.W. Mahin, ed., ASM International, Materials Park, OH, (1990).

188. Schlienger, M.E., *Understanding and Development of Advanced Techniques for the Processing of Single Crystal Turbine Components*, Ph.D. Thesis, Oregon Graduate Institute of Science and Technology, Portland, OR (1995).

APPENDIX

The following is the program used in image analysis for determination of dilution, penetration (max., min., and ave.), cladding bead features (total area, width, height, and wetting angles), and HAZ features in both electroslag and submerged arc strip surfacing.

ANALYSIS INSTRUCTIONS - ESS

```
 1> Live            :                        ;
 2> Load image      : a: filename.TIF        ;
 3> Hist. Mod.      : lo. dens.: hi. dens.   ;
 4> Sharpening      :                        ;
 5> Threshold       : pl 1, 0-44             ;
 6> Threshold       : pl 2, 135-155          ;
 7> Store image     : a: filename1.TIF       ;
 8> Grid            : plane 8, 14 X 0        ;
 9> Keep            : pl 8, wait             ;
10> Filling         : plane 1                ;
11> Keep            : pl 1, wait             ;
12> Cut             : pl 2, wait             ;
13> Keep            : pl 2, wait             ;
14> Threshold       : pl 7, 121-200          ;
```

```
15> Cut              : pl 7, wait          ;
16> Keep             : pl 7, wait          ;
17> Or               : planes 7, 2 -> 3    ;
18> Threshold        : pl 4, 115-174       ;
19> Cut              : pl 4, wait          ;
20> Keep             : pl 4, wait          ;
21> Or               : planes 4, 3 -> 3    ;
22> Copy             : plane  3, -> 2      ;
23> Copy             : plane  8, -> 6      ;
24> Cut              : pl 6, wait          ;
25> Keep             : pl 6, wait          ;
26> Draw             : pl 1, wait          ;
27> Cut              : pl 1, wait          ;
28> Xor              : planes 6, 1 -> 3    ;
29> Kill             : pl 3, wait          ;
30> Xor              : planes 6, 1 -> 4    ;
31> Keep             : pl 4, wait          ;
32> Or               : planes 8, 2 -> 5    ;
33> Draw             : pl 5, wait          ;
34> Filling          : plane 5             ;
35> Xor              : planes 8, 5 -> 5    ;
36> Copy             : plane  5 -> 2       ;
37> Xor              : planes 5, 3 -> 5    ;
38> Copy             : plane  3 -> 7       ;
39> Fraction meas.   : plane  1            ;
40> Field meas.      : plane  1            ;
41> Field meas.      : plane  2            ;
42> Field meas.      : plane  3            ;
43> Field meas.      : plane  4            ;
44> Field meas.      : plane  5            ;
45> Field meas.      : plane  6            ;
46> Field meas.      : plane  7            ;
47> Field meas.      : plane  8            ;
48> Image frame      : 0 0 511 476         ;
49> Direct meas.     : pl 1 tape, wait     ;
50> Direct meas.     : pl 2 tape, wait     ;
51> Direct meas.     : pl 4 tape, wait     ;
```

```
52> Direct meas.    : pl 5 tape, wait       ;
53> Feature meas.   : plane  1              ;
54> Feature meas.   : plane  2              ;
55> Feature meas.   : plane  4              ;
56> Feature meas.   : plane  5              ;
57> Stop
```

BIOGRAPHICAL NOTE

The author was born July 20, 1964 in Henan, People's Republic of China. He graduated from Beijing Polytechnic University with a Bachelor of Science degree in Welding Engineering in 1987. He worked as a Materials Engineer with Central Iron & Steel Research Institute in Beijing from 1987 to 1989. He then joined the Department of Materials Science and Engineering of the Oregon Graduate Institute of Science & Technology to pursue a Ph.D. degree. He successfully defended this Ph.D. thesis in 1995. A hypertext version of this thesis is also available at the author's home page currently at: http://www.cse.ogi.edu:80/~yougao/yougao.html